A MEASUREMENT OF THE RECOIL POLARIZATION OF ELECTROPRODUCED $\Lambda(1116)$

Name: Simeon B. McAleer
Department: Department of Physics
Major Professor: Larry Dennis
Degree: Doctor of Philosophy
Term Degree Awarded: Spring, 2002

The CEBAF Large Acceptance Spectrometer at the Thomas Jefferson National Laboratory was used to study the reaction $e + p \rightarrow e' + K^{+} + \Lambda(1116)$ for events where the $\Lambda(1116)$ subsequently decayed via the channel $\Lambda(1116) \rightarrow p + \pi^{-}$. Data were taken at incident electron beam energies of 2.5, 4.0, and 4.2 GeV during the 1999 E1C run period. The hyperon production spectra span the Q^2 range from 0.5 to 2.8 GeV^2 and nearly the entire range in the center of mass angles. The proton angular distribution in the $\Lambda(1116)$ rest frame is used to deduce the recoil polarization of the hyperon, and the W and $\cos\theta_{cm}^{K+}$ dependence of the recoil polarization will be presented. The data show sizeable negative polarizations for the $\Lambda(1116)$ as a function of both $\cos\theta_{cm}^{K+}$ and W.

THE FLORIDA STATE UNIVERSITY

COLLEGE OF ARTS AND SCIENCES

A MEASUREMENT OF THE RECOIL POLARIZATION OF ELECTROPRODUCED $\Lambda(1116)$

By

SIMEON B. MCALEER

A Thesis submitted to the
Department of Physics
in partial fulfillment of the
requirements for the degree of
Doctor of Philosophy

Degree Awarded:
Spring Semester, 2002

The members of the Committee approve the thesis of Simeon B. McAleer defended on DECEMBER 13, 2001.

Larry Dennis
Professor Directing Thesis

Jerry Magnan
Outside Committee Member

Mark Riley
Committee Member

Simon Capstick
Committee Member

David Van Winkle
Committee Member

Mom, Dad, I did it. Thank you.

The Space Between
The tears we cry
Is the laughter keeps us coming back for more
- Dave Matthews

ACKNOWLEDGEMENTS

The first people that I would like to thank are my parents, Janet and Simeon. They have pushed, prodded, and supported me through the education system which culminated in this thesis. I would not have been able to accomplish any of this without their help and support. Everyday I ask myself whether the things I am doing would make them proud. I hope so far I have been able to succeed in that goal.

The next person I would like to acknowledge is my advisor, Dr. Larry Dennis. I could not have lucked out with a better person to guide me through this thesis. He was always there to offer support be it a physics idea, computer equipment, or simply listening as a friend. It really meant a great deal to me and I owe him a lot. I would always look forward to anytime that he would come to visit. It would mean a few meals out and a screening of the newest movie release. I would like to thank Larry for letting me stay in Newport News where I could be closer to my family and friends.

I would next like to thank Dr. Steve Barrow for his tireless work helping me. At times I was probably close to impossible to work with but Steve put up with me like a champ. Steve also provided invaluable assistance in reading the many rough drafts of this document and helping me to mold it into the document it is today. Perhaps the most telling story about Steve's assistance would be one of the many in which I would ask Steve a question to which he did not have an immediate answer. The day would come to a close and I would go home and leave the problem at work.

Inevitably, though, the next day, the first words out of Steve's mouth would be "I was thinking about your problem last night and I think I have a solution."

I would like to thank the other people with whom I worked while I was at Jefferson Lab. The professors from other universities and the Jefferson Lab staff members who helped me in this research, in particular, Dr. William Brooks, Dr. Volker Burkert, Dr. Latifa Elouhadri, Dr. Arne Freyberger, Dr. Mark Ito, Dr. Bernhard Mecking, Dr. Bogdan Niczyporuk, Dr. L. Cole Smith, Dr. Stepan Stepanya, ad Dr. Dennis Weygand, provided invaluable assistance throughout the course of this thesis. I would really like to thank Dr. Joe Manak for his guidance both professional and personal during his time at Jefferson Lab. I would like to thank my fellow strange particle physicists, Dr. Dan Carman, Dr. Kyungseon Joo, Dr. Mac Mestayer, Dr. Gabriel Nicelescu, and Dr. Rheinard Schumaker. I would especially like to thank the other graduate students with whom I worked at Jefferson Lab: Dr. Simon Taylor, Dr. Costy Louckachine, Dr. Richard Thompson, Dr. Burin Asavabihop, Dr. Hovanes Egyian, (soon to be Dr.) Rob Feuerbac, and (soon to be Dr.) John McNabb. These guys got Hall B to a working product in its very early stages. They also performed a lot of the essential, time consuming studies which fail to get any recognition in any final work.

I would like to thank my fellow Florida State graduate students, Damon Jackson, Charlie Buhler, Scott Myers, Russ Gilmartin, Mike Eisenberg, Rob Laird, and Dave Soltysick for helping me stay sane while I was taking classes at FSU. I would also like to thank them for making supporting the FSU football team so much fun. I am glad that we got to see FSU win the National Championship while we were still at FSU, just like we hoped. I would especially like to thank my fellow student, Adam Dooley, and his wife Nicole, for all the times that they provided a roof over my head on visits back to Tallahassee. I would also like to thank Adam for giving me someone to compete against when it came to the comprehensive exam and a completion date for this thesis. But most of all I would just like to thank Adam and Nicole for being good friends throughout everything.

I would like to thank my sister Kathy and my brother Ed for just letting me know that they are there for me whenever I need them. Even though I never used their help or advice as much as I should I just want to let them know that I appreciate it and I am there for them if they ever need it. I am also trying really hard to live up to the expectations of being the "cool" uncle to Kyra.

I would like to thank my other friends, Mike Horne, Colin Crawford, Ryan Smith, Carolyn Amato, Aileen and John Farrelly, Mike Coyle, Jeff Short, Todd Callahan, and Bill and Nicole Benedict. Thanks to Horne and Colin especially for allowing me to sleep on their couches during the D.C. weekends too numerous to count. Also thank you Mike and Colin for coining the term the McAlyear to let me know that I needed to finally finish this degree. Thank you Carolyn Amato for just being there on the other side of the phone whenever I needed you. I am always here for you. I would also like to extend my thanks to Michelle Cullen who was there as a great friend through the last part of this ordeal to show me the light at the end of the tunnel.

I would like to thank Mr. Frank Catapano for helping foster an interest in math and science in Resurrection Ascension Grammar School. I would like to thank Regis High School and in particular the faculty members, Ms. Lynda Blankenship, Mrs. Patricia Hannan, Mr. Robert Sikso, and Fr. Garaventa for their support through my awkward teen years. I would like to thank the University of Scranton for a fine Jesuit education. I would like to thank my fellow physics student, Dr. David Longo for being an excellent study partner and friend. I would also like to thank Dr. Varonides whose help continued even after I graduated and got to FSU letting me know that I could handle the weird, new tensor mathematics that I was seeing for the first time.

I would like to thank my committee members Dr. Simon Capstick, Dr. David Van Winkle, Dr. Mark Riley, and Dr. Jerry Magnan for helping me through this process.

I would also like to acknowledge the outstanding efforts of the staff of the Accelerator and Physics Divisions at Jefferson Laboratory that made this measurement possible. This work is supported by the U.S. Department of Energy and the National Science Foundation. The Southeastern Universities Research Association operates the Thomas Jefferson National Accelerator Facility for the United States Department of Energy under contract DE-AC05-84ER40150.

TABLE OF CONTENTS

APPENDICES

LIST OF TABLES

LIST OF FIGURES

ABSTRACT

The CEBAF Large Acceptance Spectrometer at the Thomas Jefferson National Laboratory was used to study the reaction $e + p \rightarrow e' + K^{+} + \Lambda(1116)$ for events where the $\Lambda(1116)$ subsequently decayed via the channel $\Lambda(1116) \rightarrow p + \pi^{-}$. Data were taken at incident electron beam energies of 2.5, 4.0, and 4.2 GeV during the 1999 E1C run period. The hyperon production spectra span the Q^2 range from 0.5 to 2.8 GeV^2 and nearly the entire range in the center of mass angles. The proton angular distribution in the $\Lambda(1116)$ rest frame is used to deduce the recoil polarization of the hyperon, and the W and $\cos\theta_{cm}^{K+}$ dependence of the recoil polarization will be presented. The data show sizeable negative polarizations for the $\Lambda(1116)$ as a function of both $\cos\theta_{cm}^{K+}$ and W.

CHAPTER 1

INTRODUCTION

1.1 Overview

The goal of nuclear physics is to understand the fundamental nature of matter by studying the atomic nucleus. To date all matter is understood through the Standard Model to be comprised of leptons, one type of which is an electron, and quarks, of which there are six types: up, down, strange, charm, top, and bottom. These quarks can join in combinations of two or three quarks to form hadrons such as the commonly known particles, protons and neutrons, and the not so commonly known particles, such as kaons, pions, and lambdas. Four fundamental forces govern the way in which quarks combine and interact: the gravitational, electromagnetic, strong, and weak forces. Despite the presence of all four forces in nuclear matter, by far the most important are the strong and weak forces. By studying the behavior of hadrons, therefore, information can be gained about quarks and the forces holding them together.

In 1947, a cosmic-ray research group in Manchester [1] discovered the existence of particles which exhibited behavior much different than other known particles. These particles, coined strange due to this different behavior, were produced copiously in strong interactions but decayed extremely slowly compared with particles which underwent strong force decays. These V particles, so named for the shape which they left in bubble chamber pictures, were later identified as kaons and lambdas. In order to understand the behavior of these new particles, in 1952 M. Gell Mann [2] proposed a new additive quantum number, strangeness, S. He identified the positive kaon, K^+ as having S=+1 and the Λ with S=-1. Since that time, particles containing strange quarks have been extensively studied.

Measurements of strangeness production involving an incident photon, either real or virtual, on a proton target, have been carried out for more than 40 years, motivated by issues such as the importance of the strange quark-antiquark sea within nucleons and the predicted abundance of strange quarks within the quark-gluon plasma[3]. Despite all of this work, a comprehensive model to describe the underlying mechanism of strangeness production is unavailable. One of the difficulties could be due to the role the strange quark plays compared to that of the up and down quarks[4]. A strange quark-antiquark pair introduces a new degree of freedom which results in, even close to threshold, a number of nucleon and hyperon resonances that contribute to the production process, but are absent from nonstrange processes. In addition, phenomenological investigations of strangeness production are further hampered by a lack of knowledge of several relevant coupling constants and form factors[4]. More cross section measurements are needed, and theorists place special emphasis on the need for polarization observables which are particularly sensitive to individual resonance contributions[5].

From the middle of the 1970s until recently, little theoretical or experimental work has been done in the field of electromagnetic production of strangeness, mainly due to a lack of adequate experimental facilities and the complexity of the production mechanism. New theoretical investigations into the field, however, have been sparked by work at accelerators such as the Thomas Jefferson National Accelerator Facility (TJNAF) in Newport News, VA with its continuous electron beam and the CEBAF Large Acceptance Spectrometer (CLAS).

As part of the larger kaon physics program at TJNAF, the primary reaction of interest to this thesis, shown in Fig. 1.1 is

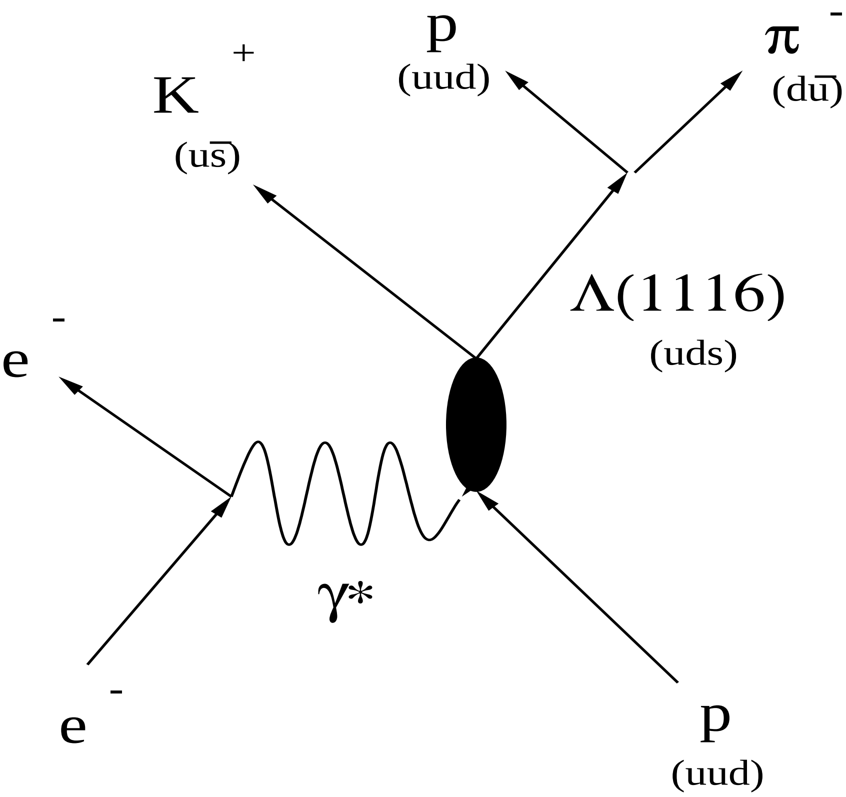

Figure 1.1. The reaction of primary focus to this thesis is shown in cartoon form. The quark structure of some of the particles is written in parenthesis beneath the particle.

$$e + p \rightarrow e' + K^+ + (\Lambda(1116) \rightarrow p + \pi^-). \tag{1.1}$$

In this reaction, the initial electron, which enters the figure from the bottom left corner, interacts with the target proton, shown entering from the bottom right corner, and scatters in a new direction. This interaction occurs through the exchange of a single photon, γ^*, described as being virtual since it can not be detected experimentally. The interaction between the proton and this virtual photon creates a positive kaon and a lambda, whose mass, 1116 MeV/c^2, is shown in parenthesis. The $\Lambda(1116)$ travels for a certain distance and then decays into a proton and a negative pion. The experiment described in this thesis used the CLAS spectrometer to detect the proton from this decay as well as the scattered electron and the positive kaon.

The detected energies and momenta from these three particles and the knowledge that energy and momentum are conserved, allows the energy and momentum from the undetected negative pion, $\Lambda(1116)$, and γ^* to be reconstructed.

The interesting physics involved in this reaction can be found in the quark structure of the hadrons involved, shown in parenthesis in Fig. 1.1. The target proton contains two up quarks,u, and a down quark, d. The interaction of the proton and the virtual photon, though, creates a strange, s, -antistrange, $\bar{s}$ quark pair through a strong interaction. The creation of the $\Lambda(1116)$, therefore, forces the creation of new quarks. Thus, by studying the $\Lambda(1116)$, knowledge can be gathered about quark creation.

The $\Lambda(1116)$ is also an unstable particle and must decay. The mass of the $\Lambda(1116)$, however, is too light for the $\Lambda(1116)$ to decay into another strange particle and a nucleon. Therefore, strangeness can not be conserved in this reaction. This forces the $\Lambda(1116)$ to decay weakly. In weak decays, the parity quantum number is not conserved. As shall be seen in later sections, parity non-conservation is what enables the angular distributions of the proton decay fragment to be used to measure the $\Lambda(1116)$ recoil polarization. These facts make the $\Lambda(1116)$ an interesting laboratory to study the elemental forces and structure of nature.

To set the groundwork for a complete discussion of the electroproduction of the $\Lambda(1116)$, the first section of this chapter will discuss the basic formalism involved in electron scattering experiments, as well as the particulars of induced $\Lambda(1116)$ polarization. The two models typically used to describe $\Lambda(1116)$ electroproduction will be presented in the following section. In the third section, the previous measurements for electromagnetically produced $\Lambda(1116)$ induced polarization are discussed. The fourth section will discuss the motivation behind this experiment and the reasons for using the CLAS detector. The last section of this chapter will then give a brief overview of the remaining chapters of this thesis.

1.2 Formalism

1.2.1 Mathematical Formalism

Standard four-vector notation is used throughout this thesis, where

$$x^\mu = (x_0, \mathbf{x}). \tag{1.2}$$

A metric is chosen such that the Lorentz invariant contraction between two four-vectors is given by

$$x^\mu y_\mu = x_0 y_0 - \mathbf{x} \cdot \mathbf{y} \tag{1.3}$$

and

$$x^\mu x_\mu = x_0 x_0 - \mathbf{x} \cdot \mathbf{x} = (x_0, \mathbf{x})^2. \tag{1.4}$$

Three-vectors are typically represented in bold face, although they occasionally appear as $\overrightarrow{x}$. Unit vectors are given with the notation $\hat{\mathrm{x}} \equiv \frac{\mathrm{x}}{|\mathrm{x}|}$.

This thesis also uses the natural c.g.s. units in which $\mathrm{c} \equiv \hbar \equiv 1$.

1.2.2 Physics Variables

The electroproduction of $\Lambda(1116)$ through the reaction

$$e + p \rightarrow e' + K^+ + \Lambda(1116) \tag{1.5}$$

is best understood using Fig. 1.2. The momentum four-vectors of the individual particles, defined as (E, $\mathbf{p}$), are presented as

$$e_{1_\mu} + p_\mu = e_{2_\mu} + k_\mu + l_\mu \tag{1.6}$$

or inside the parenthesis of Fig. 1.2. The target proton has no initial momentum in the laboratory frame and therefore has a momentum four-vector characterized as ($\mathrm{M_p}$,

0), where $\mathrm{M_p}$ is the mass of the proton. The momentum of the initial electron in this framework lies solely along the z-axis such that the momentum three-vector of the initial electron can be written as $(0, 0, \mathrm{p_{Beam}})$. This initial electron and the scattered electron define the electron scattering plane, while the three-vector momenta of the K^+ and $\Lambda(1116)$ define the hyperon production plane. The angle between these two planes is defined as ϕ_{cm}.

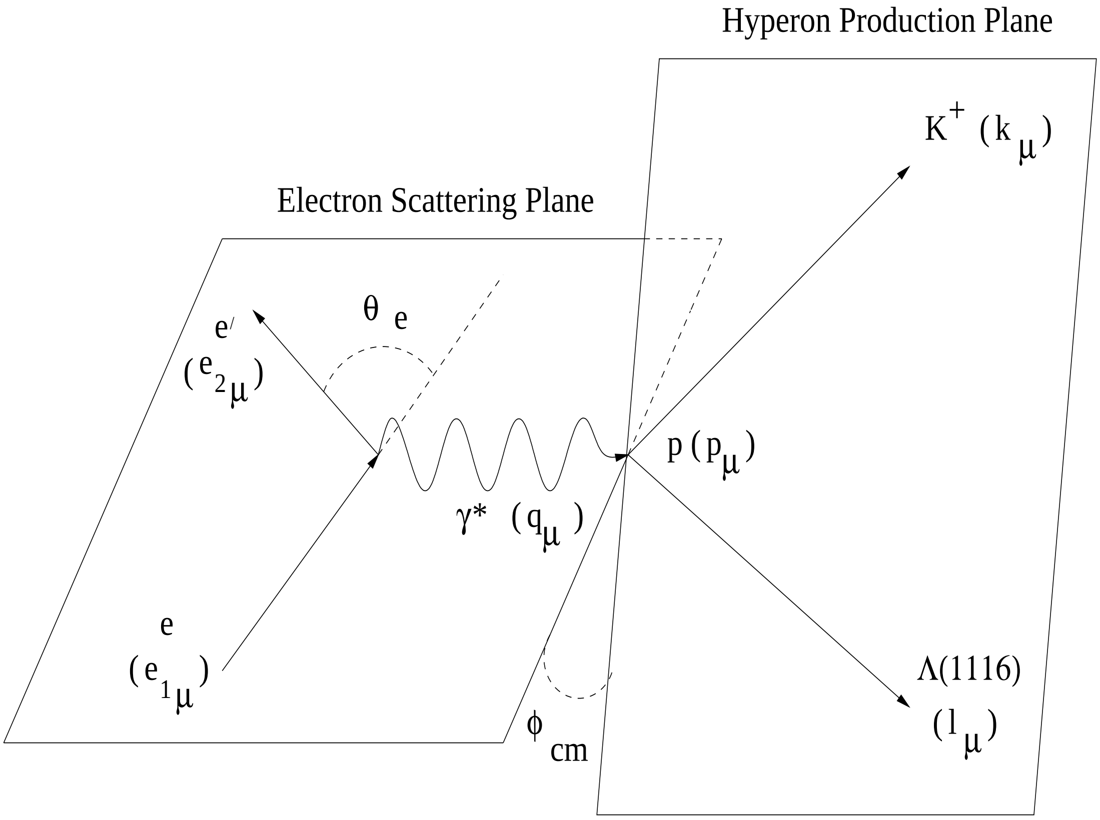

Figure 1.2. Lab frame schematic of electroproduction of the $\Lambda(1116)$ off a hydrogen target. The momentum four-vectors of the individual particles are represented in parenthesis. The angle between the incident and scattered electrons is θ_e, while the angle between the electron scattering plane and the hyperon production plane is ϕ_{cm}. The interaction between the electron and the target photon is mediated by a virtual photon of mass $-Q^2$ and energy ν.

Using the one-photon exchange approximation, the interaction between the incident electron and the target proton is mediated by a virtual photon, represented as γ^* in Fig. 1.2. The momentum four-vector for this virtual photon, which lies in both the electron scattering plane and the hyperon production plane, is written as

$$q_\mu = e_{1_\mu} - e_{2_\mu} = (\nu, \mathbf{q}), \tag{1.7}$$

where ν is the energy of the virtual photon. The invariant quantity Q^2 can then be formed from the virtual photon momentum four-vector using the relation

$$-Q^2 = \nu^2 - \mathbf{q^2} \tag{1.8}$$

where Q^2 is the negative mass squared of the virtual photon. Q^2 can also be written as

$$Q^2 = 4EE' \sin^2(\theta_e/2), \tag{1.9}$$

where E and E$'$ represent the energies of the incident and scattered electrons, and θ_e is the lab scattering angle of the electron. It is apparent that in the limit of small electron scattering angles Q^2 approaches zero, giving the usual massless relationship of a real photon.

Unlike real photons which only possess transverse polarization, virtual photons can also be polarized longitudinally. The amount of transverse and longitudinal polarization, respectively, are given by

$$\epsilon = \frac{1}{1 + \frac{2\mathbf{q^2}}{Q^2} \tan^2 \frac{\theta_e}{2}}, \tag{1.10}$$

and

$$\epsilon_L = \frac{Q^2}{\nu^2}\epsilon. \tag{1.11}$$

The last important set of equations that define electroproduction processes are the Mandelstam variables, defined as

$$s \equiv (q_\mu + p_\mu)^2 \equiv (k_\mu + l_\mu)^2, \tag{1.12}$$

$$t \equiv (p_\mu - l_\mu)^2 \equiv (k_\mu - q_\mu)^2, \tag{1.13}$$

and

$$u \equiv (q_\mu - l_\mu)^2 \equiv (k_\mu - p_\mu)^2. \tag{1.14}$$

These variables are equivalent to the squared mass of the intermediate particle in the Feynman diagram description of these scattering processes shown in Fig. 1.3. One such exchanged mass frequently used is the mass in an s-channel diagram of the intermediate hadronic state, W, which is equal to $\sqrt{s}$, or equivalently

$$W^2 = (q_\mu + p_\mu)^2 = M_p^2 + 2M_p\nu - Q^2. \tag{1.15}$$

In Sec. 1.3, the utility of these various diagrams will be discussed in more detail.

1.2.3 Cross Sections

The general form of the cross section for kaon electroproduction is given in the standard notation [6] as

$$\frac{d^5\sigma}{d\Omega_{E'}\,d\Omega_K\,dE'} = \Gamma\frac{d\sigma_\nu}{d\Omega_K}, \tag{1.16}$$

where the virtual photon flux is defined as

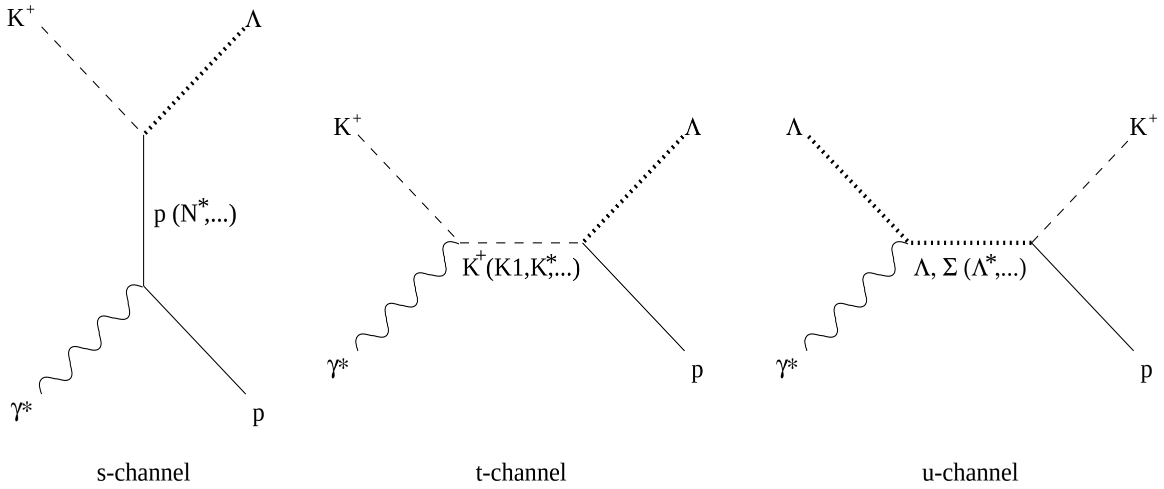

Figure 1.3. Feynman diagrams used to model Λ(1116) electroproduction. These figures illustrate the Mandelstam variables s, t, and u. For example, s is the squared mass of the intermediate particle in the s-channel diagrams.

$$\Gamma = \frac{\alpha}{8\pi^2}\frac{W}{M_p^2 E^2}(W^2 - M_p^2)\left[\frac{1}{Q^2(1-\epsilon)}\right] \tag{1.17}$$

The cross section for a polarized target and a polarized beam is then given in terms of response functions $R_i^{\beta\alpha}$ as

$$\begin{aligned}\frac{d\sigma_\nu}{d\Omega_K} &= KS_\alpha S_\beta[R_T^{\beta\alpha} + \epsilon_L R_L^{\beta\alpha}\sqrt{2\epsilon_L(1+\epsilon)}({}^cR_{TL}^{\beta\alpha}\cos\phi_{cm} + {}^sR_{TL}^{\beta\alpha}\sin\phi_{cm}) \\ &+ \epsilon({}^cR_{TT}^{\beta\alpha}\cos 2\phi_{cm} + {}^sR_{TT}^{\beta\alpha}\sin 2\phi_{cm}) \\ &+ h\sqrt{2\epsilon_L(1-\epsilon)}({}^cR_{TL'}^{\beta\alpha}\cos\phi_{cm} + {}^sR_{TL'}^{\beta\alpha}\sin\phi_{cm}) + h\sqrt{1-\epsilon^2}R_{TT'}^{\beta\alpha}], \end{aligned} \tag{1.18}$$

where

$$K = \frac{|\mathbf{k}|}{k_\gamma^{cm}}, \tag{1.19}$$

$\mathrm{k}_\gamma^{\mathrm{cm}}$ is the virtual photon momentum in the center of mass system, and $|\mathbf{k}|$ is the center of mass momentum of the kaon. Here ϕ_{cm} is the angle of the hadron production plane, defined by the kaon and Λ(1116) momenta, with respect to the electron scattering plane. The helicity of the electron beam is defined as h. A sum is implied over the superscripts and subscripts α and β which refer to the target and $\Lambda(1116)$ polarizations, respectively. The superscripts c and s refer to the cosine or sine term of the response function with which they are associated.

The operators for the polarization projection are defined as

$$S_\alpha = (1, \mathbf{S}), \tag{1.20}$$

and

$$S_\beta = (1, \mathbf{S}'), \tag{1.21}$$

with

$$\mathbf{S} = (\hat{S_x}, \hat{S_y}, \hat{S_z}), \tag{1.22}$$

and

$$\mathbf{S}' = (\hat{S_{x'}}, \hat{S_{y'}}, \hat{S_{z'}}). \tag{1.23}$$

The electron-plane coordinates, shown in Fig. 1.4, are defined by the unprimed coordinate system with $\hat{z}$ along $\mathbf{q}$, $\hat{y}$ normal to the electron scattering plane, and $\hat{\mathrm{x}} = \hat{\mathrm{y}} \times \hat{\mathrm{z}}$. The primed coordinate system is defined by the hadron production plane so that $\hat{z'}$ points along the kaon momentum vector, $\hat{y'}$ is normal to the hyperon production plane and $\hat{\mathrm{x}'} = \hat{\mathrm{y}'} \times \hat{\mathrm{z}'}$.

For the case with no beam, target, or recoil polarization Eq. 1.18 becomes

$$\sigma_0 = \left(\frac{d\sigma_\nu}{d\Omega_K}\right)^{00} = K[R_T^{00} + \epsilon_L R_L^{00} + \sqrt{2\epsilon_L(1+\epsilon)}R_L^{00}\cos\phi_{cm} + \epsilon R_{TT}^{00}\cos 2\phi_{cm}], \tag{1.24}$$

which gives $\mathrm{KR}_\mathrm{i}^{00} = \sigma_\mathrm{i}$, the usual unpolarized cross section notation.

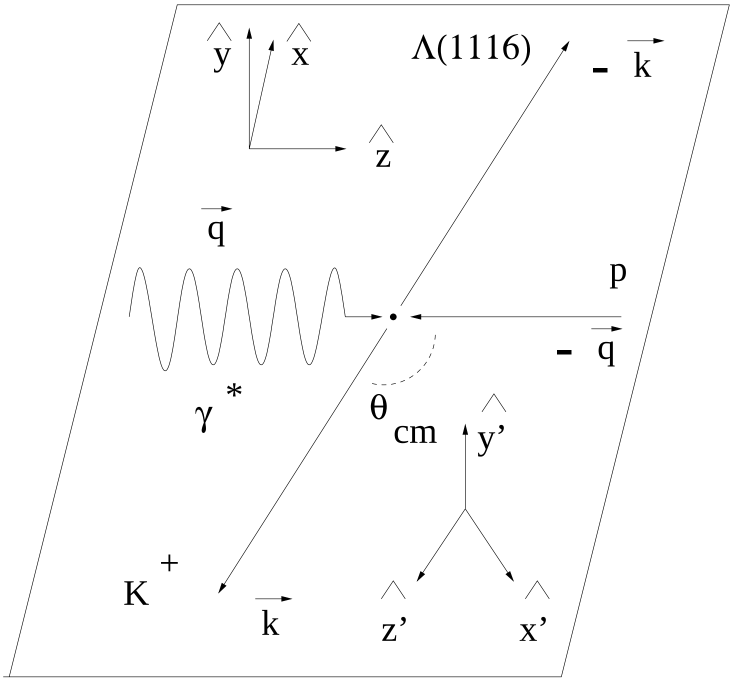

Figure 1.4. Schematic showing the directions of two different frames of reference used in this analysis. The directions $\hat{z}$, which points along the direction of the virtual photon, $\hat{y}$, which points out of the electron scattering plane, and $\hat{x}$ define directions used in the center of mass frame. The directions $\hat{z'}$, $\hat{x'}$, and $\hat{y'}$ are the directions used in the $\Lambda(1116)$ rest frame. $\hat{z'}$ points along the direction of the motion of the K^+. $\hat{y'}$ points out of the hyperon production plane and $\hat{x'}$ is defined by the cross product of $\hat{y'}$ and $\hat{z'}$.

For the current case of an unpolarized beam or target but a measured recoil polarization, Eq. 1.18 reduces to

$$\frac{d\sigma_\nu}{d\Omega_K} = \sigma_0(1 + P^0_{x'}\hat{S_{x'}} + P^0_{y'}\hat{S_{y'}} + P^0_{z'}\hat{S_{z'}}), \tag{1.25}$$

The $P^0_{j'}$ represent the induced $\Lambda(1116)$ polarizations and can be written in terms of the response functions as

$$\begin{aligned} P^0_{x'} &= \tfrac{K}{\sigma_0}\left(\sqrt{2\epsilon_L(1+\epsilon)}R^{x'0}_{TL}\sin\phi_{cm} + \epsilon R^{x'0}_{TT}\sin 2\phi_{cm}\right), \\ P^0_{y'} &= \tfrac{K}{\sigma_0}\left(R^{y'0}_{T} + \epsilon_L R^{y'0}_{L} + \sqrt{2\epsilon_L(1+\epsilon)}R^{y'0}_{TL}\cos\phi_{cm} + \epsilon R^{y'0}_{TT}\cos 2\phi_{cm}\right), \\ P^0_{z'} &= \tfrac{K}{\sigma_0}\left(\sqrt{2\epsilon_L(1+\epsilon)}R^{z'0}_{TL}\sin\phi_{cm} + \epsilon R^{z'0}_{TT}\sin 2\phi_{cm}\right). \end{aligned} \tag{1.26}$$

To improve statistics and to accommodate finite bin sizes, Eq. 1.25 must be integrated over ϕ_{cm}. The polarization projection operators $\hat{S_{j'}}$ must therefore be written in terms of the coordinates $\hat{x}$, $\hat{y}$, and $\hat{z}$. The hadron production coordinates can be related to the unprimed coordinates in the electron plane by counterclockwise rotation of ϕ_{cm} about $\hat{z}$ followed by a counterclockwise rotation of θ_K about $\hat{y'}$. The rotation matrix to accomplish this task can be written as

$$\mathcal{R} = \begin{pmatrix} \cos\theta_K \cos\phi_{cm} & \cos\theta_K \sin\phi_{cm} & -\sin\theta_K \\ -\sin\phi_{cm} & \cos\phi_{cm} & 0 \\ \sin\theta_K \cos\phi_{cm} & \sin\theta_K \sin\phi_{cm} & \cos\theta_K \end{pmatrix}. \tag{1.27}$$

In the electron scattering frame, the polarization projection operator can then be written in terms of the hyperon production plane as

$$S' = \mathcal{R}S = \begin{pmatrix} \cos\theta_K \cos\phi_{cm}\hat{S}_x + \cos\theta_K \sin\phi_{cm}\hat{S}_y - \sin\theta_K\hat{S}_z \\ -\sin\phi_{cm}\hat{S}_x + \cos\phi_{cm}\hat{S}_y \\ \sin\theta_K \cos\phi_{cm}\hat{S}_x + \sin\theta_K \sin\phi_{cm}\hat{S}_y + \cos\theta_K\hat{S}_z \end{pmatrix}, \tag{1.28}$$

The cross section can be rewritten using the relationships for $\hat{S_{j'}}$ as

$$\frac{d\sigma_\nu}{d\Omega_K} = \sigma_0(1 + P^0_x\hat{S}_x + P^0_y\hat{S}_y + P^0_y\hat{S}_y), \tag{1.29}$$

where the P^0_j are the observed induced polarization of the $\Lambda(1116)$ with the electron plane coordinates and are equal to

$$\begin{aligned} P^0_x &= P^0_{x'}\cos\theta_K\cos\phi_{cm} + P^0_{y'}(-\sin\phi_{cm}) + P^0_{z'}\sin\theta_K\cos\phi_{cm}, \\ P^0_y &= P^0_{x'}\cos\theta_K\sin\phi_{cm} + P^0_{y'}\cos\phi_{cm} + P^0_{z'}\sin\theta_K\sin\phi_{cm}, \\ P^0_z &= P^0_{x'}(-\sin\theta_K) + P^0_{z'}\cos\theta_K. \end{aligned} \tag{1.30}$$

By integrating ϕ_{cm} from 0 to 2π the cross section becomes greatly simplified as

$$\int_0^{2\pi} \frac{d\sigma_\nu}{d\Omega_K} d\phi_{cm} = \left(\int \sigma_0\right)(1 + P_xS_x + P_yS_y + P_zS_z), \tag{1.31}$$

with

$$\int \sigma_0 = 2\pi K(R_T^{00} + \epsilon_L R_L^{00}), \tag{1.32}$$

and the P_j^0 are

$$\begin{aligned}
&P_x^0 = 0, \\
&P_y^0 = \pi\sqrt{2\epsilon_L(1-\epsilon)}\frac{K}{\int \sigma_0}(R_{TL}^{x'0}\cos\theta_K + R_{TL}^{y'0} + R_{TL}^{z'0}\sin\theta_K), \\
&P_z^0 = 0.
\end{aligned} \tag{1.33}$$

Thus, with the above binning conventions and without a polarized beam or target, the $\Lambda(1116)$ induced polarization can only be observed along the axis normal to the hyperon production plane. The projections along the other two axes must be zero.

1.2.4 Λ(1116) Polarization

The previous section illustrates how the $\Lambda(1116)$ induced polarization can be related to certain response functions. This section briefly demonstrates how the weak decay of the $\Lambda(1116)$ makes it possible to determine this induced polarization directly from the asymmetry in its decay angular distribution.

Following the convention of Ref. [7], to examine the polarization of the $\Lambda(1116)$, first consider the associated mesonic production process

$$\pi^- p \to \Lambda(1116)K^0. \tag{1.34}$$

In this process, governed by the strong force, the $\Lambda(1116)$ can be (and generally is) spin-polarized. Since the strong force conserves parity the $\Lambda(1116)$ must be polarized with its spin, σ, transverse to the hyperon production plane, because only this projection is invariant under a parity transformation of the coordinate system(x,y,z → -x,-y,-z). Polarization in the production plane does change sign, and is therefore not allowed.

Since the mass of the $\Lambda(1116)$ is less than the mass threshold for a strong decay into a nucleon and a kaon, the lightest strange meson, strangeness can not be conserved in the reaction. As a result, the $\Lambda(1116)$ decays weakly, an interaction in which parity is not conserved. This fact, as shall be seen in the following paragraphs, is what allows the detection of the polarization of the $\Lambda(1116)$.

For this discussion, the direction of the $\Lambda(1116)$ polarization is defined to be along the z-axis of the $\Lambda(1116)$ rest frame, as shown in Fig 1.5. Looking at the decay channel $\Lambda(1116) \rightarrow \mathrm{p}\pi^-$, the angular distribution of the emitted π^- or proton will depend on the relative orbital angular momentum, l. With $\mathrm{J}_\Lambda = \frac{1}{2}$, $\mathrm{J_z} = \pm\frac{1}{2}$, and $\mathrm{J_{Proton}} = \frac{1}{2}$, the spins of the proton and the $\Lambda(1116)$ could be aligned with l=0 or anti-aligned with l=1. This leads to a general expectation of a combination of s- and p-waves.

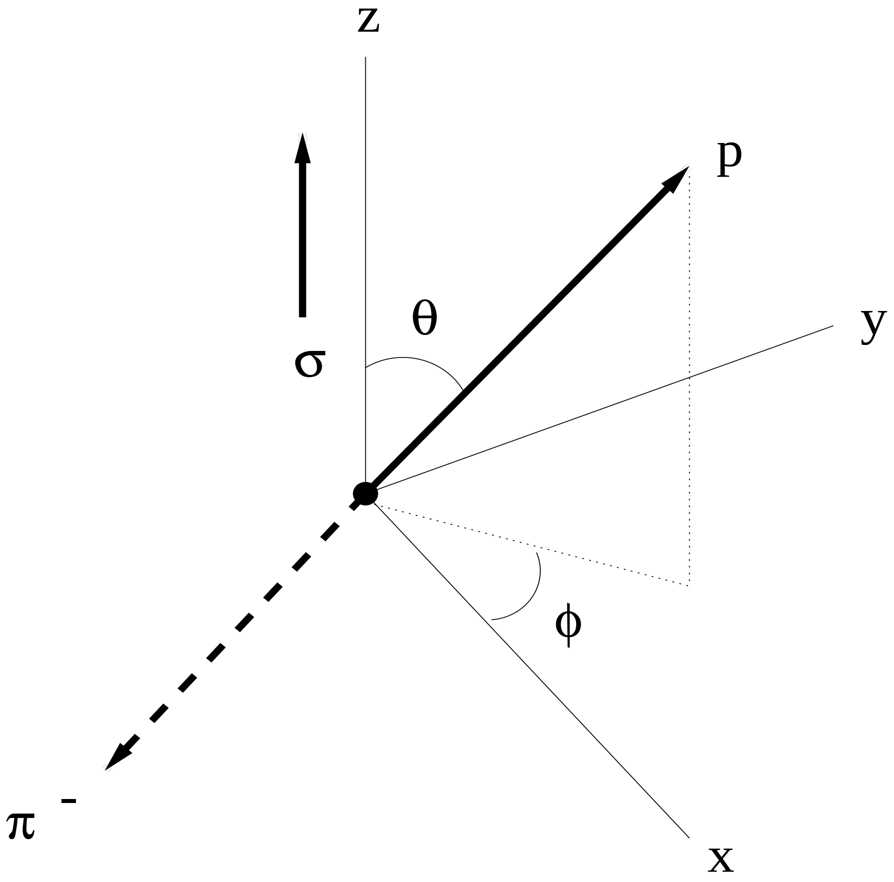

Figure 1.5. Definition of axes and directions in $\Lambda(1116)$ decay [7]. Here σ is the direction of the $\Lambda(1116)$ spin and θ is the polar angle of the proton from the $\Lambda(1116)$ decay.

Denote the z-component of the proton spin vector by m_1 and the z-component of l by m_2. For the s-wave case, m_2 must be equal to zero and the wave function would be $Y_l^m = Y_0^0$. Therefore, for $J_z = +\frac{1}{2}$, the total wave function is

$$\psi_s = a_s Y_0^0 \chi^+, \tag{1.35}$$

where a_s is the s-wave amplitude and χ^+ is the proton spin-up wave function for the $m_1 = +\frac{1}{2}$ state. For the p-wave $m_1 + m_2 = +\frac{1}{2}$, so either $m_2 = 0$ and $m_1 = +\frac{1}{2}$ or $m_2 = +1$ and $m_1 = -\frac{1}{2}$.

Using Clebsch-Gordon coefficients for adding a J = 1 spin with a J = $\frac{1}{2}$ spin, the $J_{total} = m = +\frac{1}{2}$ spin is given as

$$\psi_p = a_p \left[\sqrt{\frac{2}{3}} Y_1^1 \chi^- - \sqrt{\frac{1}{3}} Y_1^0 \chi^+ \right], \tag{1.36}$$

where a_p is the p-wave amplitude. In general, both the s- and p-wave amplitudes can be complex.

If both s- and p-waves are present, the total wave function is therefore written as

$$|J = 1/2, m_z = 1/2\rangle = \psi = \psi_s + \psi_p = \left[a_p \sqrt{\frac{2}{3}} Y_1^1 \right] \chi^- + \left[a_s Y_0^0 - a_p \sqrt{\frac{1}{3}} Y_1^0 \right] \chi^+. \tag{1.37}$$

The resulting angular distribution, using the orthogonality of χ^+ and χ^-, becomes

$$\psi^* \psi = a_p^2 \left(\sqrt{\frac{2}{3}} Y_1^1 \right)^2 + \left(a_s Y_0^0 - a_p \sqrt{\frac{1}{3}} Y_1^0 \right) \left(a_s Y_0^0 - a_p^* \sqrt{\frac{1}{3}} Y_1^0 \right), \tag{1.38}$$

where one of the phases is arbitrary and a_s is taken to be real. Substituting into Eq. 1.38 the spherical harmonics, $Y_0^0 = 1$, $Y_1^0 = \sqrt{\frac{1}{3}} \cos\theta$, and $Y_1^1 = -\sqrt{\frac{2}{3}} \sin\theta$ leads to

$$\psi^*\psi = |a_p|^2 \sin^2\theta + |a_s|^2 + |a_p|^2 \cos^2\theta - a_s[a_p + a_p^*] \cos\theta = |a_s|^2 + |a_p|^2 - 2a_s Re(a_p^*) \cos\theta. \tag{1.39}$$

If α is introduced such that

$$\alpha = \frac{2a_s Re(a_p^*)}{|a_s|^2 + |a_p|^2}, \tag{1.40}$$

the angular distribution can be rewritten as

$$I(\theta) = 1 - \alpha \cos\theta. \tag{1.41}$$

In this formalism, θ is defined relative to the $\Lambda(1116)$ spin, a direction which can not be measured directly. Measurements are instead made relative to the hyperon production plane. If θ is redefined in this manner, Eq. 1.41 becomes

$$I(\theta) = 1 - \alpha P \cos\theta, \tag{1.42}$$

where P, which is measured in this thesis, is the average induced polarization of the $\Lambda(1116)$. The parity violation is therefore manifested by an up-down asymmetry of the decay proton relative to the hyperon production plane.

Returning to the discussion of parity, the parity of a system is equal to the product of the parity of its parts. Therefore, for the $\Lambda(1116)$ decay, parity conservation requires

$$\pi_\Lambda = \pi_{Proton} \pi_{Pion} (-1)^l, \tag{1.43}$$

would hold true. Since the parity of both the $\Lambda(1116)$ and the proton is +1 and the parity of the π^- is -1, $(-1)^l = -1$ for parity conserving reactions. The l=0 s-wave state in this case violates this rule and parity is not conserved. The l=1 p-wave state conserves parity in this reaction. For α to be non-zero, both the s- and p-waves must be present. Fortunately, the $\Lambda(1116)$ decays weakly, a process in which parity may be violated. As a result, the polarization of the $\Lambda(1116)$ can be measured.

1.2.5 Definition of Missing Mass

A concept used repeatedly in this thesis is missing mass. In this technique, the physics laws of conservation of energy and conservation of momentum are used to calculate the energy and momentum of a particle or particles not directly measured. These quantities are then combined to determine the mass of the missing particle.

An example of this technique is used in identifying possible hyperon candidates. In this experiment, the momentum four-vectors e_{1_μ}, e_{2_μ}, k_μ in Fig. 1.2 were measured. The momentum four-vector of the unmeasured hyperon can be deduced by requiring the total four-momentum of the system to be conserved:

$$(e_{1_\mu} + p_\mu) = (e_{1_\mu} + k_\mu + l_\mu) \tag{1.44}$$

and

$$(q_\mu + p_\mu) = (k_\mu + l_\mu). \tag{1.45}$$

Shifting terms in Eq. 1.45 gives

$$l_\mu = (q_\mu + p_\mu - k_\mu), \tag{1.46}$$

or in expanded notation,

$$(E_l, \mathbf{l}) = (\nu + M_p - E_K, \mathbf{q} - \mathbf{k}). \tag{1.47}$$

Squaring both sides and collecting terms gives

$$m_l^2 = (\nu^2 - |\mathbf{q}|^2) + (E_K^2 - |\mathbf{k}|^2) + 2\nu M_p - 2E_K(\nu + M_p) - 2\mathbf{q}\cdot\mathbf{k}. \tag{1.48}$$

Finally, replacing the relevant terms with Q^2 and the kaon mass yields the expression for the missing mass of the hyperon as

$$m_l^2 = -Q^2 + M_K^2 + 2\nu M_p - 2E_K(\nu + M_p) - 2\mathbf{q}\cdot\mathbf{k}. \tag{1.49}$$

This same technique is also employed to determine the mass of the undetected π^- from the $\Lambda(1116)$ decay.

1.3 Model Descriptions

Unlike pion photoproduction, the production of strangeness is complicated by the more complex role played by the strange quark versus the roles played by the u and d quarks[4]. An increased number of resonances could contribute to the process due to the additional degree of freedom. There is, however, a limited amount of data against which theorists can test their models [4].

In order to overcome the limited experimental data, these models do not rely solely on $\Lambda(1116)$ electroproduction data. Instead, they attempt to simultaneously model the cross sections of numerous, similar reactions, such as

$$\begin{gathered}
\gamma + p \to K^+ + \Lambda(1116), \\
\gamma + p \to K^+ + \Sigma^0(1192), \\
\gamma + p \to K^0 + \Sigma^+(1189), \\
e + p \to e' + K^+ + \Lambda(1116), \\
e + p \to e' + K^+ + \Sigma^0(1192),
\end{gathered} \tag{1.50}$$

which are expected to have similar production mechanisms.

The two standard model types employed are the isobaric and Regge models. Both of these model types employ the same two dynamic constraints, crossing symmetry and duality, limiting the type and number of diagrams used. Crossing is an exact symmetry of the S matrix that relates reactions involving particles (antiparticles) in the initial/final state with reactions where the corresponding antiparticles (particles) are in the final/initial state [8]. For example kaon photoproduction, (γ, K^+), and radiative capture, (K^-, γ) are crossing related reactions for these kaon production models. Because the reactions are governed by the same dynamical mechanism, any parameterization must apply simultaneously to both sets [5].

Dolen, Horn, and Schmid [9] found that interference models which include resonances in both s- (u-) and t-channels simultaneously, include certain diagrams for the low energy π-N scattering twice. These results lead to the concept of duality between s-, u-, and t-channel resonances in π-N scattering. This also leads to speculation that all hadronic interactions may share this property [5]. Both types of models, therefore, attempt to account for higher order s-channel diagrams by using low order t-channel diagrams.

1.3.1 Isobaric Models

Isobaric models attempt to explicitly calculate the kaon production amplitudes using Feynman diagrams, shown in Fig. 1.3, and first order perturbation theory, in which each diagram corresponds to the exchange of one particle or resonance. This technique is known as the tree approximation. The relevant diagrams are the extended Born terms for the exchange of a proton (p), kaon (K), and hyperon (Y) and the resonant terms for the exchange of the N*, K*, and Y* resonances [4].

Within this general approach, isobaric models differ in which particular diagrams are employed in the model and whether the coupling constants, which correspond to each diagram's vertices, are constrained. For example, the model proposed by David, *et al.*[4], only uses s-channel diagrams in which J $\leq$ 5/2, the J $=$ 1/2 u-channel diagrams, and the K*(892) and the K1(1270) resonances in the t-channel. These choices, however, are largely phenomenological. This fact is further demonstrated

Table 1.1. Exchanged particles used and the coupling constants derived for various isobaric models of KΛ production [4].

Particle	(I)J^{π}	Coupling	Model Description		
			AS [10]	WJC [5]	SL [4]
Λ	(0) $1/2^{+}$	$g_{K\Lambda N}/\sqrt{4\pi}$	-4.17 ± 0.75	-2.38	-3.16 ± 0.01
Σ	(1) $1/2^{+}$	$g_{K\Sigma N}/\sqrt{4\pi}$	1.18 ± 0.66	0.27	0.91 ± 0.10
$K^{*}(892)$	(1/2) 1^{-}	$G_V/4\pi$	-0.43 ± 0.07	-0.16	-0.05 ± 0.01
		$G_T/4\pi$	0.20 ± 0.12	0.08	0.16 ± 0.02
K1(1270)	(1/2) 1^{+}	$G_{V1}/4\pi$	-0.10 ± 0.06	0.02	-0.19 ± 0.01
		$G_{T1}/4\pi$	-1.21 ± 0.33	0.17	-0.35 ± 0.03
N1(1440)	(1/2) $1/2^{+}$	$G_{N1}/\sqrt{4\pi}$	-1.41 ± 0.60		-0.01 ± 0.12
N4(1650)	(1/2) $1/2^{-}$	$G_{N4}/\sqrt{4\pi}$		-0.04	
N6(1710)	(1/2) $1/2^{+}$	$G_{N6}/\sqrt{4\pi}$		-0.06	
N7(1720)	(1/2) $3/2^{+}$	$G^{a}_{N7}/4\pi$			-0.04 ± 0.01
		$G^{b}_{N7}/4\pi$			-0.14 ± 0.04
N8(1675)	(1/2) $5/2^{-}$	$G^{a}_{N8}/4\pi$			-0.63 ± 0.10
		$G^{b}_{N8}/4\pi$			-0.05 ± 0.56
L1(1405)	(0) $1/2^{-}$	$G_{L1}/\sqrt{4\pi}$		-0.07	-0.31 ± 0.06
L3(1670)	(0) $1/2^{-}$	$G_{L3}/\sqrt{4\pi}$	-3.17 ± 0.86		1.18 ± 0.09
L5(1810)	(0) $1/2^{+}$	$G_{L5}/\sqrt{4\pi}$			-1.25 ± 0.20
S1(1660)	(1) $1/2^{+}$	$G_{S1}/\sqrt{4\pi}$			-4.96 ± 0.19

in Table 1.1 by the lack of consistency in the derived coupling constant values from three of the most popular isobaric models.

1.3.2 Regge Models

The Regge models also start with the standard Feynman diagram formalism. In Regge models, however, the usual pole-like Feynman propagator of a single particle is replaced by a Regge propagator. The exchange of a Regge trajectory then represents the exchange of a family of particles with the same internal quantum numbers [11]. The vertex structure of the Feynman diagrams which correspond to the first materialization of the trajectory are kept.

Following the notation of [12], one can write the pseudoscalar hadronic current for photoproduction via t-channel kaon exchange as

$$j^{\mu}_{K:t-exchange} \propto ie \not{\kappa} \overline{Y}_f (\kappa - p_K)^{\mu} \times \mathcal{P}^K_{Regge} \times g_{K\Lambda N} \gamma^5 N_i, \tag{1.51}$$

where $\kappa_\mu = (q - p_K)^\mu$ is the momentum four-vector of the exchanged kaon, Y_f is the Lambda spinor, q^μ is the photon momentum four-vector, p^μ_K is the kaon momentum four-vector, $g_{K\Lambda N}$ is the coupling constant at the (pΛK$^+$) vertex, and N_i is the proton spinor. The Regge propagator, $\mathcal{P}^K_{Regge}$, is of the form,

$$\mathcal{P}^K_{Regge} = \left(\frac{s}{s_0}\right)^{\alpha_K(t)} \left(\frac{\pi \alpha'_K}{\sin \pi \alpha_K(t)}\right) \left(\frac{\mathcal{S}_K + e^{i\pi\alpha_K(t)}}{2}\right) \left(\frac{1}{\Gamma(1 + \alpha_K(t))}\right), \tag{1.52}$$

where s and t are the conventional Mandelstam variables, s_0 is a mass scale, α_K and α'_K represent the Regge trajectory, $\mathcal{S}_K = \pm 1$ is the signature of the trajectory, and Γ is the standard Gamma function. In this framework,

$$\alpha_K(t) = \alpha'_K(t - m^2), \tag{1.53}$$

and

$$\alpha'_K = 0.7. \tag{1.54}$$

As the first pole on the trajectory is approached, the Regge propagator in Eq. 1.52 reduces to the Feynman propagator. A similar current operator and propagator can be constructed for the pseudovector coupling of the K^* mesons. In the model in Ref. [11], the only parameters are those of the first materialization of the trajectories with the external particles ($g_{K\Lambda N}$, $g_{K^*\Lambda N}$, $\ldots$), which are determined so as to describe all existing high energy data.

The Regge photoproduction model is extended to an electroproduction model by multiplying the separately gauge invariant K and K* t-channel diagrams by a monopole form factor. For the model in Ref. [13], this factor is given as,

$$F_{K,K^*}(Q^2) = \frac{1}{1 + Q^2/\Lambda^2_{K,K^*}}, \tag{1.55}$$

where Λ^2_{K,K^*} are mass scales that are essentially free parameters, but can be fixed so as to fit the high Q^2 behavior of the separated electroproduction cross sections, σ_T and σ_L. The coupling constants at the (KΛN) and (K^* Λ N) vertices are kept the same.

1.4 Previous Data

Although a modest amount of $\Lambda(1116)$ electroproduction cross section data exists [12] [14], there is a definite scarcity of any electromagnetically produced $\Lambda(1116)$ induced polarization data. A few photoproduction experiments off hydrogen targets which had measured the $\Lambda(1116)$ recoil polarization were performed in the 1960's [15]-[19]. All of these experiments used a magnetic spectrometer on one side of the beam to measure the K^+. On the other side of the beam were placed two telescopes, one above the hyperon production plane and one below the plane, to detect the proton from the $\Lambda(1116) \rightarrow p\pi^-$ decay. Primarily these measurements were taken near threshold with $\theta_{cm} \sim 90°$. The results of these experiments are summarized in Table 1.2. The situation recently improved for photoproduction due to an experiment that used the ELSA electron stretcher ring and the SAPHIR detector [20]. This experiment took data over the full range of $\cos\theta^K_{cm}$ and $1.688 < \mathrm{W} < 2.152$ GeV. The results from this experiment are plotted in Fig. 1.6.

Results for $\Lambda(1116)$ polarization in electroproduction are even more scarce. In 1999, L. Teodorescu *et al.* used the Jefferson Lab Hall C spectrometers to make the first measurement of the recoil polarization of the electroproduced $\Lambda(1116)$ [21]. In this experiment, the scattered electron was measured in one magnetic spectrometer while the K^+ and proton were detected in a second magnetic spectrometer. A total of 40 kinematically complete events were measured at $Q^2 = 1.50\,GeV^2$ and $\theta^{cm}_{K\gamma} = 14°$.

Table 1.2. Results of photoproduced $\Lambda(1116)$ induced polarization.

Experiment	E_γ (MeV)	θ^K_{cm} (deg)	Polarization
Cornell[15]	1000 ± 19	93 ± 4.3	0.23 ± 0.11
Cornell[15]	1026 ± 23	87 ± 4.3	0.21 ± 0.10
Cornell[15]	1056 ± 29	80 ± 4.6	0.40 ± 0.13
Cornell[15]	1056 ± 29	80 ± 4.6	0.36 ± 0.13
Cornell[15]	1095 ± 30	91 ± 4.0	0.09 ± 0.11
Cornell[15]	1121 ± 33	90 ± 3.5	0.37 ± 0.11
Frascati[17]	1050 ± 20	85 ± 6	0.39 ± 0.15
Frascati[17]	1018 ± 20	93 ± 7	0.30 ± 0.13
Frascati[17]	963 ± 10	91 ± 9	0.19 ± 0.14
Frascati[17]	1020 ± 30	61 ± 7	0.16 ± 0.12
Caltech[18]	1098 ± 5.3	89.9 ± 5.1	0.337 ± 0.089
Caltech[18]	1187 ± 8.5	90.2 ± 4.6	0.296 ± 0.067
Caltech[18]	1292 ± 11.6	89.8 ± 4.3	0.082 ± 0.065
Tokyo[19]	1160	46.0	0.54 ± 0.09
Tokyo[19]	1160	70.0	0.44 ± 0.10
Tokyo[19]	1160	90.0	0.27 ± 0.14
Tokyo[19]	1100	47.6	0.38 ± 0.12
Tokyo[19]	1100	72.8	0.48 ± 0.10
Tokyo[19]	1100	94.4	0.32 ± 0.19
Tokyo[19]	1054	49.8	0.28 ± 0.12
Tokyo[19]	1054	76.8	0.07 ± 0.13

From this data sample, limits of the recoil polarization were quoted to be between -0.21 and +0.89.

1.5 Motivation For Current Work

This thesis extends the previous electroproduced $\Lambda(1116)$ polarization data set by covering a large kinematic region, which is comparable to the statistical improvements measured at SAPHIR for the photoproduction data set. Data were taken for this current experiment in the region $1.61 < W < 2.2$ GeV and $0.5 < Q^2 < 2.5\ GeV^2$. Data cover the full range of ϕ_{cm} and $\cos\theta^K_{cm}$. Fig. 1.7 compares the kinematic coverage of this experiment and previous polarization measurements, with the exception of the SAPHIR data.

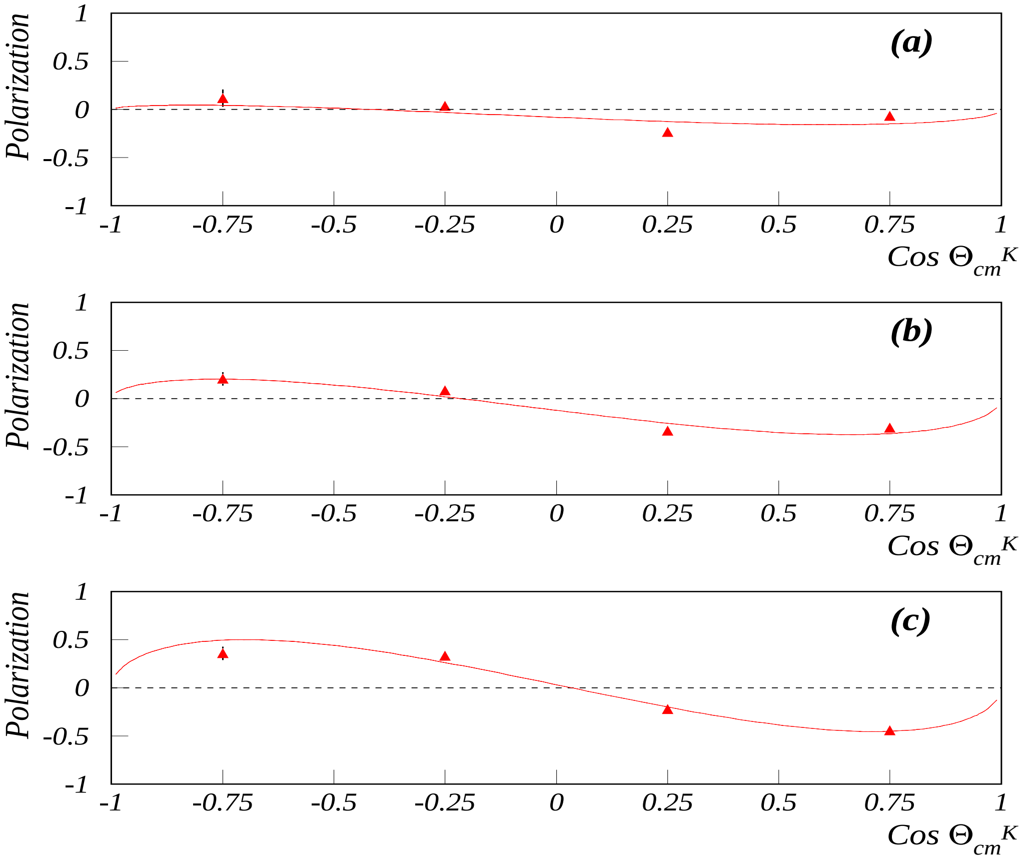

Figure 1.6. Recoil polarization results from SAPHIR for W bins (a) $1.602 \leq W < 1.716$ GeV, (b) $1.716 \leq W < 1.873$ GeV, and (c) $1.873 \leq W < 2.152$ GeV [20]. The lines represent fits to the data by Legendre polynomials up to l=1.

Since the $\Lambda(1116)$ decays weakly, its polarization information is transferred to its decay products through their angular distributions. In this context, the $\Lambda(1116)$ is a self analyzing particle. The decay mode $\Lambda(1116) \rightarrow p\pi^-$ and the detection of the proton was chosen for this particular analysis for two main reasons. First, this decay channel has the largest $\Lambda(1116)$ branching ratio as shown in Table 1.3. In addition, CLAS has a much larger acceptance for this decay than for the neutral particle decay channels. In theory, the $\Lambda(1116)$ polarization, though, could have been determined from either the decay proton or π^-. The proton was chosen since, for the majority of events, the π^- doesn't traverse a fiducial region of CLAS.

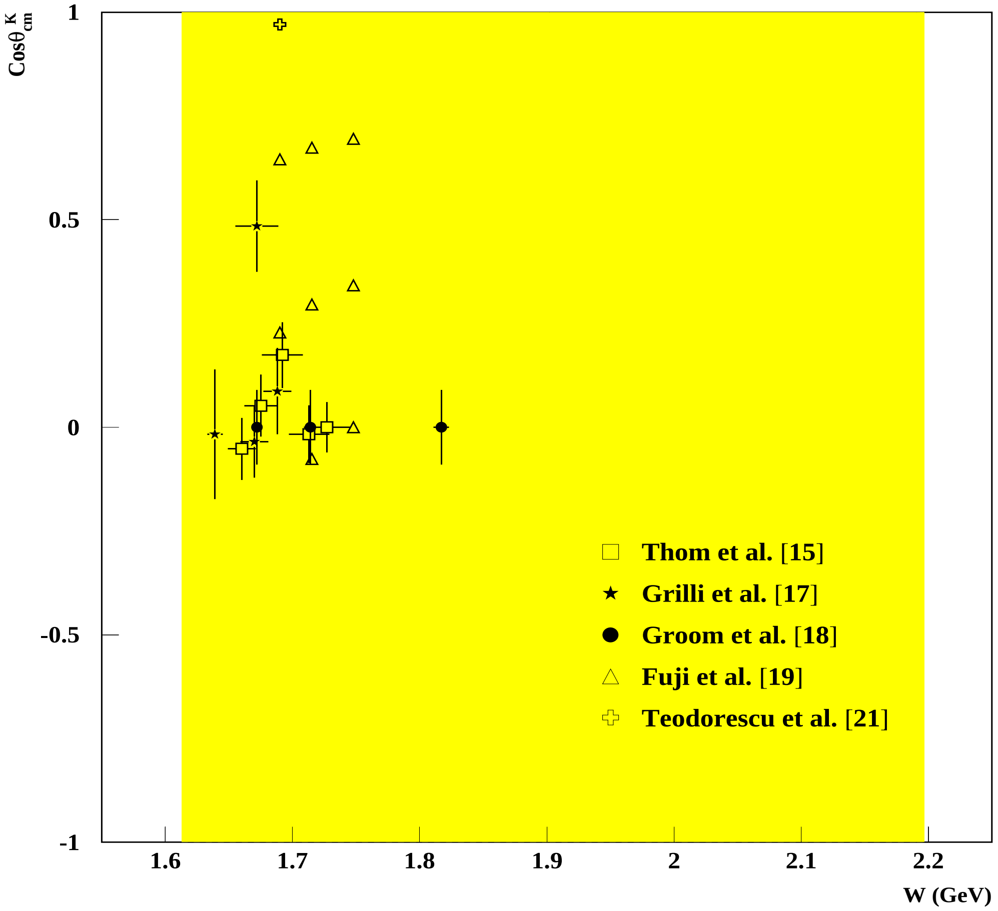

Figure 1.7. Kinematic coverage of previous Λ(1116) recoil polarization measurements. The current CLAS data covers the full kinematic range of $\cos\theta_{cm}^{K^+}$ for the W region from 1.61 GeV to 2.2 GeV.

Table 1.3. Λ(1116) decay modes [22].

Decay Mode	Fraction
p π^-	(63.9 ± 0.5) %
n π^0	(35.8 ± 0.5) %
n γ	(1.75 ± 0.15) x 10^{-3}
p π^- γ	(8.4 ± 1.4) x 10^{-4}
p e^- $\bar{\nu}_e$	(8.32 ± 0.14) x 10^{-4}
p μ^- $\bar{\nu}_\mu$	(1.57 ± 0.35) x 10^{-4}

Table 1.4. Response functions for pseudoscalar meson production [23]. The columns α and β refer to the target and recoil polarizations respectively. The ‡ refer to response functions which do not vanish but are related to other response functions.

β	α	T	L	^{c}TL	^{s}TL	^{c}TT	^{s}TT
-	-	R_T^{00}	R_L^{00}	R_{TL}^{00}	0	R_{TT}^{00}	0
-	x	0	0	0	R_{TL}^{0x}	0	R_{TT}^{0x}
-	y	R_T^{0y}	R_L^{0y}	R_{TL}^{0y}	0	‡	0
-	z	0	0	0	R_{TL}^{0z}	0	R_{TT}^{0z}
x'	-	0	0	0	$R_{TL}^{x'0}$	0	$R_{TT}^{x'0}$
y'	-	$R_T^{y'0}$	‡	‡	0	‡	0
z'	-	0	0	0	$R_{TL}^{z'0}$	0	$R_{TT}^{z'0}$
x'	x	$R_T^{x'x}$	$R_T^{x'x}$	$R_T^{x'x}$	0	‡	0
x'	y	0	0	0	‡	0	‡
x'	z	$R_T^{x'z}$	$R_T^{x'z}$	‡	0	‡	0
y'	x	0	0	0	‡	0	‡
y'	y	‡	‡	‡	0	‡	0
y'	z	0	0	0	‡	0	‡
z'	x	$R_T^{z'x}$	‡	$R_L^{z'x}$	0	‡	0
z'	y	0	0	0	‡	0	‡
z'	z	$R_T^{z'z}$	‡	‡	0	‡	0

Due to the limited data available for electroproduced strangeness, the various theoretical production models are not well constrained. This polarization data should go a long way towards constraining these models since it presents new results against which models may be tested. For example, as shown in Table 1.4, certain response functions are available only through polarization studies.

While electroproduction provides information complimentary to other production mechanisms, it also offers advantages over $\Lambda(1116)$ experiments using a real photon or a hadron as a probe. First, the interaction between the electron and the nucleon is governed by QED, which is a well understood formalism and is calculable. Therefore, one can probe the behavior of an unknown and complicated object, the nuclear current J_μ, with an interaction whose behavior is well understood [24]. Secondly, by examining a limited energy and momentum range, the virtual photon mediating the interaction can be tuned to transfer variable values of energy and momentum independently. Thus, by adjusting the momentum transferred, the spatial features of the nuclear electromagnetic current may be studied. Additionally, the virtual photon, unlike a real photon, has both longitudinal and transverse polarizations. The transversely polarized photon interacts with the electromagnetic 3-vector current density, whereas the longitudinal polarized photon interacts with the charge density of the nucleus [25]. Probing hadronic systems with virtual photons provides additional insight into the basic reaction mechanism (resonance formation, polarization and interference effects, etc.) and also to fundamental hadronic structure information (electromagnetic form factors) [5]. Lastly, the interaction of the electron and kaon with the surrounding matter is relatively weak, greatly reducing distortions in the reaction entrance and exit channels.

The relative weakness of the interaction of the electron, though, also has the drawback that the resulting cross sections are greatly reduced when compared to hadronic probes. The CLAS detector, however, was designed with such a limitation in mind [26]. The high duty factor electron beam at TJNAF and the large acceptance of CLAS compensate for this cross section reduction. Additionally, the large acceptance of CLAS allows the detection of at least three of the four final state particles. As a result, kinematically complete events can be selected leading to a much cleaner data set.

1.6 Contents of Thesis

The second chapter of this thesis will discuss in detail the CLAS detector in the Hall B end station of the TJNAF. A complete discussion of data reconstruction including particle and event identification is presented in Chapter 3. Chapter 4 discusses the work performed as part of this thesis and as part of the CLAS service work to handle the large job of preparing the complete physics data set for the entire collaboration. A discussion of the analysis techniques, including acceptance calculations, are presented in Chapter 5. The last chapter of this thesis discusses the results of this analysis and the conclusions drawn from this work.

CHAPTER 2

EXPERIMENTAL APPARATUS

2.1 Overview

The $ep \to e'K^+(\Lambda(1116) \to p\pi^-)$ experiment was performed at the Continuous Electron Beam Facility (CEBAF) at the TJNAF in Newport News, VA. This facility is devoted to the investigation of the electromagnetic structure of mesons, nucleons, and nuclei, using high duty electron and photon beams in the energy range $\sim$ 0.8 - 6.0 GeV. These beams are produced by a 100% duty cycle electron accelerator, and can be split and simultaneously delivered to the three experimental end stations, Halls A, B, and C. Hall A contains two high resolution magnetic spectrometers with a resolution of $\delta p/p \leq 10^{-4}$ for the simultaneous detection of scattered electrons and hadrons. Hall C is equipped with two medium resolution spectrometers, $\delta p/p \leq 10^{-3}$, which have complementary momentum ranges. The data presented in this thesis were taken at Hall B which contains a large acceptance medium resolution toroidal spectrometer that is described in this chapter.

2.2 The Accelerator

The TJNAF accelerator, shown in Fig. 2.1, utilizes a racetrack design in which two anti-parallel superconducting linear accelerators, known as linacs, are connected by two 180° isochronous achromatic magnetic re-circulating arcs. At the heart of the accelerating structure are 338 superconducting RF niobium cavities which have a nominal accelerating gradient of 5 MeV/m. Polarized electrons are continuously generated at the injector and enter the north linear accelerator with an energy of 45 MeV. The electrons gain 400 MeV for each pass through one of the linacs. After passing through both linacs, the beam can be extracted at the beam switchyard and sent to one or more of the three experimental halls. If the electron bunch is not extracted, it can be recirculated through the accelerator up to four more times. Thus, the experimental halls can receive electron bunches at energies of $n/5 * E_{max}$ where $n = 1 \ldots 5$. Accelerator component modifications have allowed E_{max} to increase to 5.8 GeV from the original design specifications of 4.045 GeV. Due to the lack of synchotron radiation the spread in the beam energy is $\Delta E/E \leq 10^{-4}$ [27].

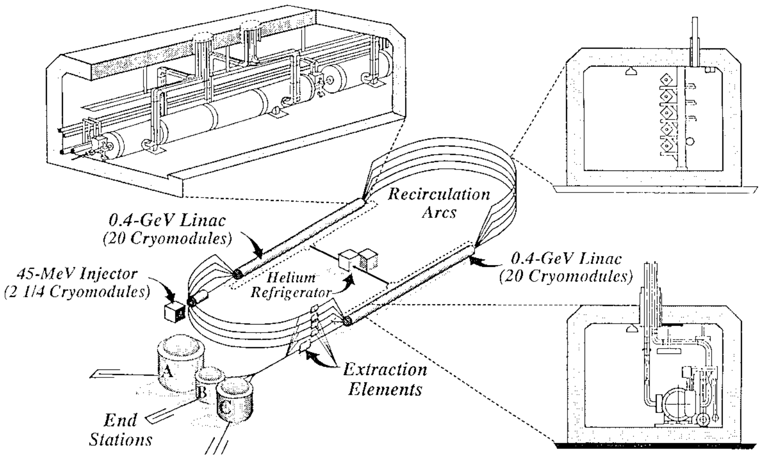

Figure 2.1. A graphical representation of the TJNAF accelerator design shows the two linacs as well as the end stations. The top left and bottom right figure enhancements show an enlarged view of the linac cryomodules. The insert at the top right shows the recirculation arcs used to connect the two linacs.

Although advertised as a continuous electron beam, there is some variation in the electron beam intensity since the beam contains some microstructure. The RF power in the niobium cavities determines this microstructure and dictates that there are separate electron pulses occurring at a frequency of 1497 MHz. This structure allows the three experimental halls to operate simultaneously at three different energies. After each pass through the accelerator, a transverse radio frequency separator at the beam switchyard can be activated to extract every third bunch of electrons to be delivered to one of the three experimental halls. The experimental halls therefore receive electron packets at a frequency of 499 MHz, or every 2.004 ns. In Hall B, during the E1C experiment operating at an average beam current of 3.5 nA, this microstructure led to beam delivery in 2 ns intervals of packets containing approximately 43 electrons.

2.3 Hall B

2.4 The CEBAF Large Acceptance Spectrometer

Hall B is devoted to experiments which require a large acceptance detector to observe several, uncorrelated particles in the final state, or for measurements in which the luminosity is limited by beam, target or accidental background. The heart of Hall B is the nearly 4π CEBAF Large Acceptance Spectrometer (CLAS), seen in Fig. 2.2, 2.3, 2.4, and 2.5, which is centered around a six gap superconducting toroidal magnet. This magnet divides the spectrometer azimuthally into six independently wired segments, or sectors. The readout for each sector lies in the shadow of the torus coils so that no additional coverage of the detector is lost. Each segment contains three layers of Drift Chambers (DC) for charged particle track reconstruction and momentum measurements. Beyond the drift chambers are the Cĕrenkov Counters (CC) used to identify electrons from their Cĕrenkov radiation. Each segment of CLAS also contains Time of Flight Scintillators (SC) for measuring the velocity of charged particles. The timing signal from the SC along with the reconstructed path length and the momentum measurement from the DC determines the masses of the charged particles. The outermost system in each sector of CLAS is the Electromagnetic Calorimeter (EC), used for neutral particle detection and the separation of electrons from fast moving negatively charged pions.

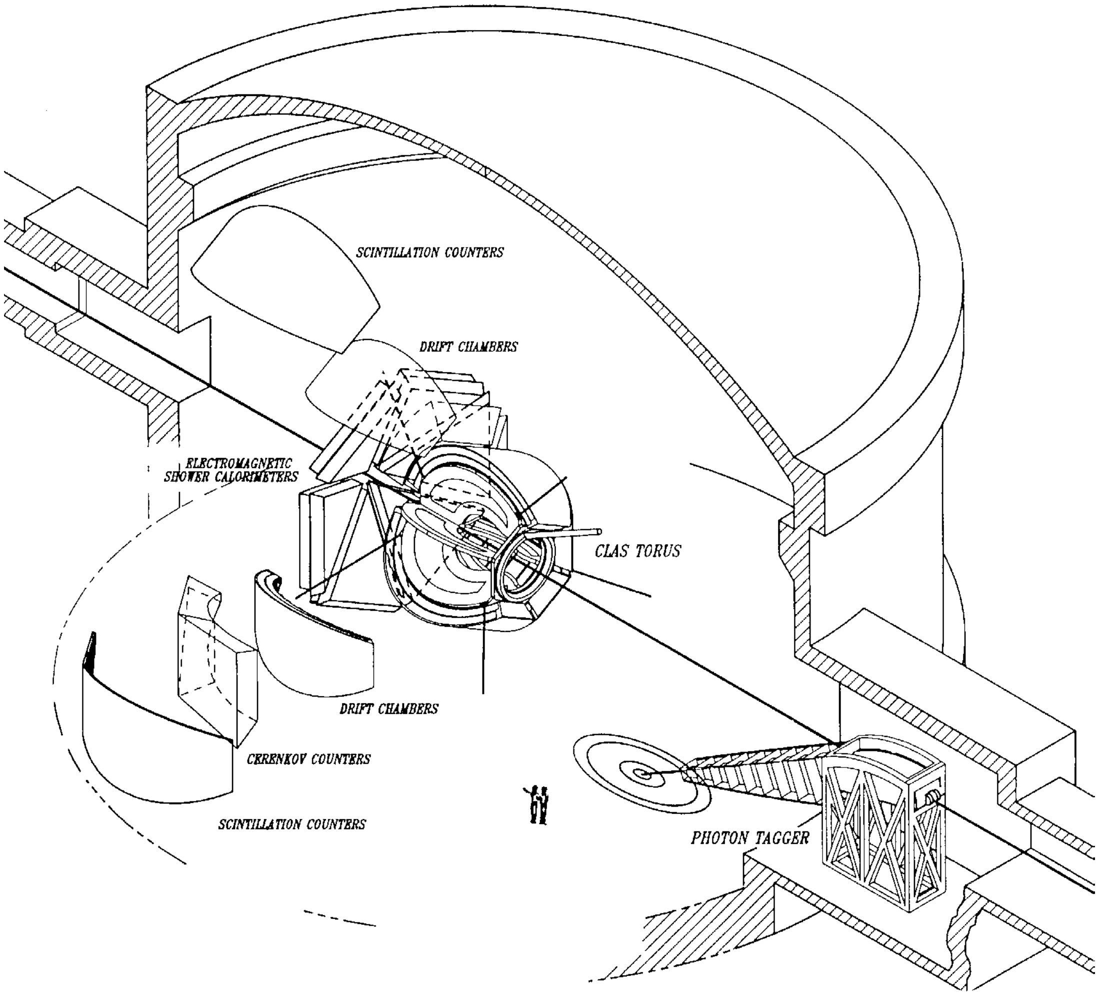

Figure 2.2. The CLAS spectrometer in Hall B with the detector components pulled out from their resident positions in the closest two sectors to show detail. The electron beam enters the hall from the lower right part of the figure. The two figures at the bottom of the figure are shown for perspective.

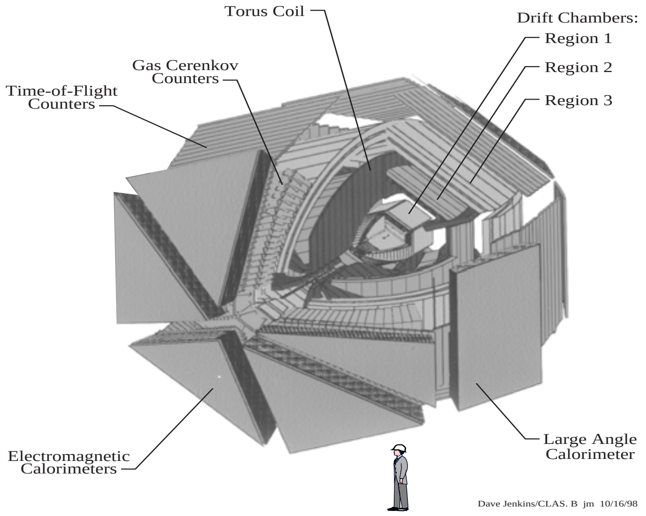

Figure 2.3. A three dimensional view of the CLAS spectrometer. Some detector components of one sector are removed to show detail.

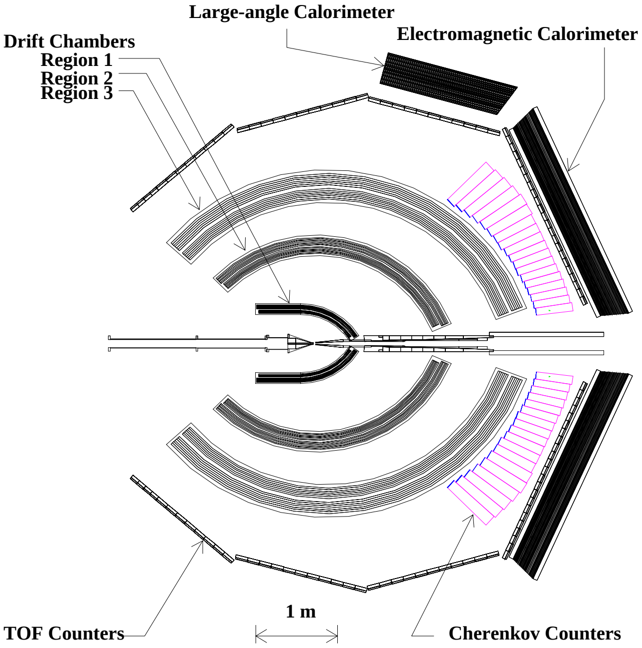

Figure 2.4. Cross sectional view of the CLAS spectrometer bisecting two opposing sectors. Clearly labeled are the drift chambers, Cĕrenkov counters, electromagnetic calorimeters, and TOF counters. The electron beam enters the figure from the left.

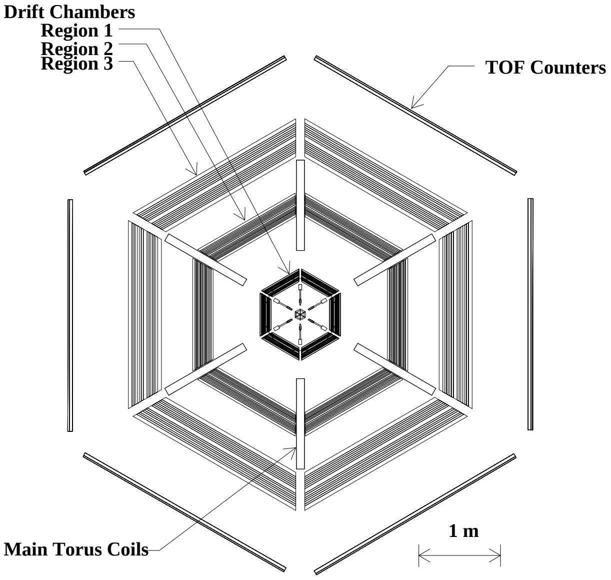

Figure 2.5. A cross sectional view of the CLAS spectrometer through the target. The SC, DC and torus coils are shown. The six structures inside of the Region 1 drift chamber which lie along the same lines as the main torus are the minitorus. The star structure at the heart of the figure is the target.

2.4.1 Toroidal Magnets

2.4.1.1 Main Torus

All six of the iron free coils of CLAS's toroidal superconducting magnet are 5 m long and 2.5 m wide. These coils limit the azimuthal coverage of CLAS to approximately 80%. Integrating over the ϕ-component of the magnetic field as a function of the particle emission angle produces values of 2 T·m in the forward directions and 0.5 T·m for scattering angles greater than 90°. The coils are arranged around the beam line to produce a magnetic field which points primarily in the ϕ-direction and approximates a toroidal geometry. Thus, charged particles exiting the target are bent either towards or away from the beam, while their trajectories in the azimuthal direction are left relatively unchanged.

The maximum current on the main torus is 3860 A. During the E1C run period, the main torus was run at three different currents: 1500, 2250, and 3375 A. For the remainder of this thesis, the data sets are identified by the beam energy and percent of the maximum torus current at which the data were taken. For example, data taken at an electron beam energy of 4.2 GeV and the main torus operating at 2250 A, is referred to as the 4.2 GeV 60% field data set.

2.4.1.2 Mini Torus

The outer two regions of the drift chambers are protected from Möller scattered electrons which result from electrons scattering off other electrons. Möller scattered electrons are the dominant source of background in electron scattering experiments, by the toroidal magnetic field. The inner regions of the drift chambers, however, are before the main torus field, and are unprotected from this radiation, which diminishes the drift chamber performance. The innermost layer of drift chambers is therefore protected by the field generated by small toroidal coils placed in the cavities of the main torus. The coils of the minitorus, seen in Fig. 2.5, are made of normal conducting materials and only occupy space inside the shadows of the main torus. As a result, the minitorus does not provide any additional obstruction to particles passing through CLAS. The minitorus field is small compared to the field from the main torus and there is very little overlap between the fields from the two magnets. The polarity of the minitorus is such that low energy electrons are bent back towards the beam line and out of the acceptance of CLAS.

2.4.2 Drift Chambers

The first detectors encountered by particles that exit the target are the drift chambers, which are used for measuring the trajectory and momentum of charged particles. The principle behind drift chambers is that charged particles ionize the gas in the chamber as they traverse it. Since the gas, a 90% Ar -10% CO_2 mixture for CLAS, is in an electric field, the ionized electrons move towards the chamber's sense wires while the positive charged particles move in the opposite direction. As the electrons move towards the sense wire they collide with other atoms in the gas, resulting in additional ionization and an amplification of the signal. The time it takes electrons to drift to the sense wires is measured and provides an accurate determination of the track location.

The CLAS drift chambers cover a laboratory polar angular range of 8° to 142°, and up to 80% of the azimuthal range. Each sector of CLAS contains three separate sets of drift chambers, known as regions, located at three radial distances from the target. The Region I drift chambers are closest to the target and are in the nearly field free region of the torus bore. This region is used to determine the initial trajectory of the charged particles as they exit the target. Region II is located between the torus coils in the area where the magnetic field is the strongest. At this point, the curvature of the particle's trajectory will be at a maximum, thus enabling good momentum determination. Region III, like Region I, is located outside of the shadow of the coils, where the magnetic field intensity is small. This region fixes the trajectory of the particle prior to its traversal of the outer detector subsystems of CLAS.

The DC wires are positioned in layers such that their positions are shifted by half the nominal spacing in each successive layer. The layers have a repeating pattern of two 140 μm diameter gold plated aluminum field wire layers followed by a layer of 20 μm diameter gold plated tungsten sense wires. In this manner, hexagonal drift cells are created with six field wires surrounding a sense wire. Within the 18 drift chamber regions there are a total of 35,148 of these individually wired drift cells. In each drift chamber region these layers are combined to create two superlayers. In the first superlayer, the wires are arranged axially to the beam direction, perpendicular to the bend of the particles. In the next superlayer, the wires are tilted at an angle of 6° stereo to provide tracking redundancy and azimuthal information.

There are numerous ways to measure the performance of the DC. Most methods revolve around measuring the proton from elastic ep collisions and comparing the results to the expected yields. One result from such a study is the tracking efficiency, the probability of identifying a track when the kinematics of the event project the track through an active part of the DC. Such a study for the E1C run period suggest the tracking efficiency is greater than 95%.

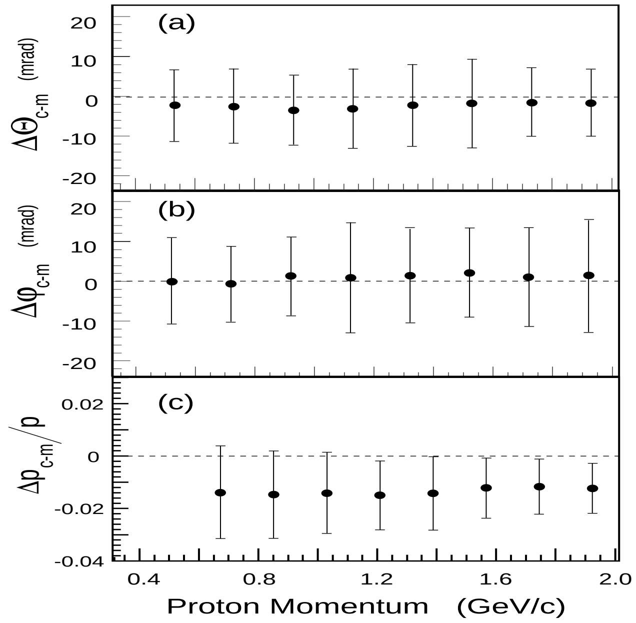

Figure 2.6. Studies of the proton reconstruction resolution from elastic scattering. (a) plots the difference between the measured and predicted proton polar angle, (b) azimuthal angle, and (c) momentum as a function of the proton momentum.[28]

Events where the electron elastically scatters off of the proton can also be used to examine the DC resolution. Measured proton kinematics are compared with the kinematics predicted from the reconstructed electron. The results of such a study versus proton momentum are shown in Fig. 2.6. Figures 2.6(a) and 2.6(b) illustrate an angular resolution of ∼10 mrad, while Fig. 2.6(c) shows that the momentum resolution, $\delta p/p$, varies from 1% to 2.5% from high to low momentum tracks. Since these figures take into account the resolution of both electron and proton tracks, the proton track resolution is close to the CLAS design goals of $\delta p/p \leq 0.5\%$ and $\delta\theta, \delta\phi \leq 2$ mrad.

The single wire resolution, whole cell averaged for each region is about 400 μm. For the overall track fit, an additional error of 300 μm for Region I, 400 μm for Region II, and 450 μm for Region III must be added to account for slight misalignments of the drift chambers and uncertainties in the magnetic field maps of the main torus and mini-torus.

For more information about the CLAS drift chambers please consult Ref. [28].

2.4.3 Cĕrenkov Counters

When a particle's speed exceeds the speed of light in a given medium, the particle creates an electromagnetic shockwave known as Cĕrenkov radiation. The threshold requirement for the onset of this effect is given by

$$v \geq c/n, \tag{2.1}$$

where n is the index of refraction of the material, c is the speed of light in vacuum, and v is the velocity of the particle. Writing Eq. 2.1 in terms of the particle's energy and mass gives the relationship

$$\gamma = E/m \geq \frac{1}{\sqrt{1 - \frac{1}{n^2}}}. \tag{2.2}$$

Based on Eq. 2.2, a careful selection of n allows the Cĕrenkov detector to act as a threshold particle detector. This is the capacity in which the CLAS CCs are used.

All six sectors of CLAS are equipped with gas Cĕrenkov counters that are used as triggering mechanisms to separate electrons from negatively charged pions. These counters occupy a region subtending an azimuthal angle of 60°, and a laboratory polar scattering angle of $8^\circ < \theta < 45^\circ$ in each sector. Since the trajectories of the particles remain in a constant plane of azimuthal angle, or ϕ, the collection optics are

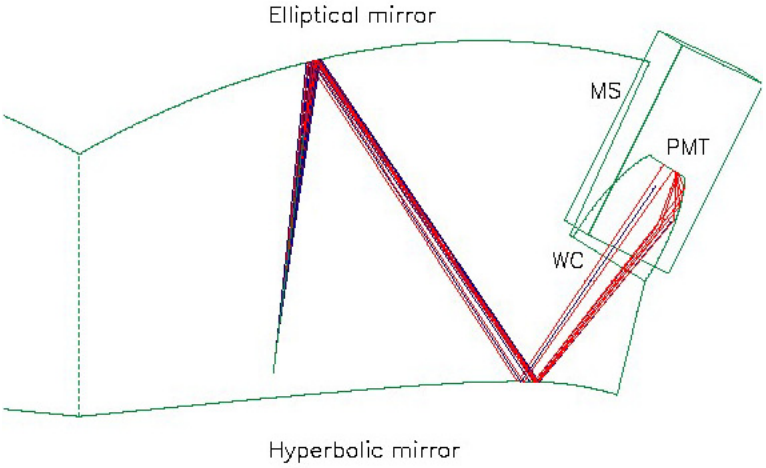

Figure 2.7. A cross sectional view of one of the 216 optical modules in the CLAS Cĕrenkov detector. The light ray details how light from a typical electron traversing the Cĕrenkov detector would be focused from the mirrors to the photomultiplier tube (PMT). The abbreviation MS refers to the magnetic shielding that protects the CC PMT from the fringe field of the CLAS main torus. [30]

designed to focus the light from the Cĕrenkov radiation in the ϕ-direction to light collecting cones and photomultiplier tubes which lie in the shadows of the torus. This focusing is done by a total of 432 hyperbolic and elliptical mirrors, which were created by vacuum depositing aluminum onto a 0.76 mm thick Lexan surface. In the θ-direction, each sector is divided into 18 regions, which are subsequently divided into two regions about the symmetry plane. This division results in 12 identical subsectors in the ϕ-direction for each θ and a total of 216 light collection modules. One such CC optical module is shown in Fig. 2.7.

The CLAS CC were designed to be part of the Level 1 trigger that separates electrons from very fast moving negatively charged pions. C_4F_{10}(perflourobutane) was chosen as the Cĕrenkov gas because it has excellent light transmission properties as well as a high photon yield. More importantly, its index of refraction (n = 1.00153) results in a electron energy threshold of about 9.24 MeV and a E_π threshold of 2.56 GeV. The CC in each of the six sectors of CLAS contains 6 cm^3 of perflourobutane.

Due to the inclusive nature of the CLAS trigger, particles can trigger the detector at the edges of the acceptance where the efficiency is poorly understood. As a result, it is important to establish fiducial volumes where the acceptance is good and large efficiency corrections are unnecessary. These fiducial definitions will be discussed in Sec. 3.3.1, but in general, for the CC, they are defined by the edges of the Cĕrenkov mirrors. A study of the efficiency within this fiducial region has shown a Cĕrenkov efficiency exceeding 99%. Outside of this fiducial region, however, the photoelectron detection inefficiency increases rapidly.

A more detailed discussion of the CC is presented in Ref. [30].

2.4.4 Time of Flight Scintillators

Scintillation counters utilize the fact that certain types of materials emit photons when they are struck by radiation that has absorption rates in the material. Each sector of CLAS uses this property to provide timing signals for physics events.

CLAS contains 57 2 cm thick rectangular scintillating counters made of Bicron BC-408, with photomultiplier tubes(PMTs) at both ends. The counters cover a laboratory scattering polar angular range of $8^\circ < \theta < 142^\circ$ and the full azimuthal range of each sector. The paddles are arranged such that they are parallel to the axial DC wires. The width was chosen so that the paddle subtends a scattering angle of $\sim 2^\circ$, leading to 15 cm wide scintillators at forward angles and 22 cm wide scintillators at large scattering angles. The scintillators range in length from 32 to 445 cm depending on the polar angle of the scintillator. The SC covers a total surface area of 206 m^2.

Design specifications for the CLAS SC call for timing resolutions of $\sigma = 120$ ps at the smallest angles, and $\sigma = 250$ ps at larger angles. Experimentally, the average time resolution for CLAS is 163 ps [29].

Please consult Ref. [29] for more detailed information about the CLAS SC.

2.4.5 Electromagnetic Calorimeters

As mentioned in Sec. 2.4.3, under ideal circumstances the CLAS CC can discriminate between electrons and fast moving pions up to pion energies of 2.5 GeV. For the $E_{beam} = 2.5$ GeV data set, pions which exceed this energy are kinematically impossible. The creation of more energetic pions at higher beam energies, however, necessitates another detection element to reject these fast moving pions.

Electromagnetic calorimeters measure the energy deposited in scintillators as layers of high density material, with which the scintillator layers are alternated, cause the particle to create showers of e^+e^- pairs and photons. In addition to detecting and triggering on electrons with energies greater than 0.5 GeV, the CLAS EC can detect photons down to an energy of 0.2 GeV. The ECs are also used to detect neutrons and can discriminate between neutrons and photons through time of flight measurements. The EC is able to provide these capabilities while also providing good energy and position resolutions.

Like the CC, the EC covers an angular range of not quite 60° in the azimuthal direction and $8^\circ < \theta < 45^\circ$ in the laboratory scattering polar angle. The ECs employ a total thickness of 16 radiation lengths, with 39 alternating layers of 10 mm thick BC-412 plastic scintillator followed by 2.2 mm thick lead sheets. Each EC has a surface shaped like an equilateral triangle, and follows a progressive geometry in which each layer covers a slightly larger area than the previous layer. This design feature helps to limit shower leakage at the edges of the fiducial volume.

All scintillator strips are sliced into 36 strips parallel to a given side of its equilateral triangle shape. Each layer's slices are rotated through an angle of 120° with respect to the previous layer. This construction leads to three separate orientations, seen in Fig. 2.8, (labeled u,v,w,) which provide stereo information on the location of the energy deposited. Each orientation is further divided into an inner

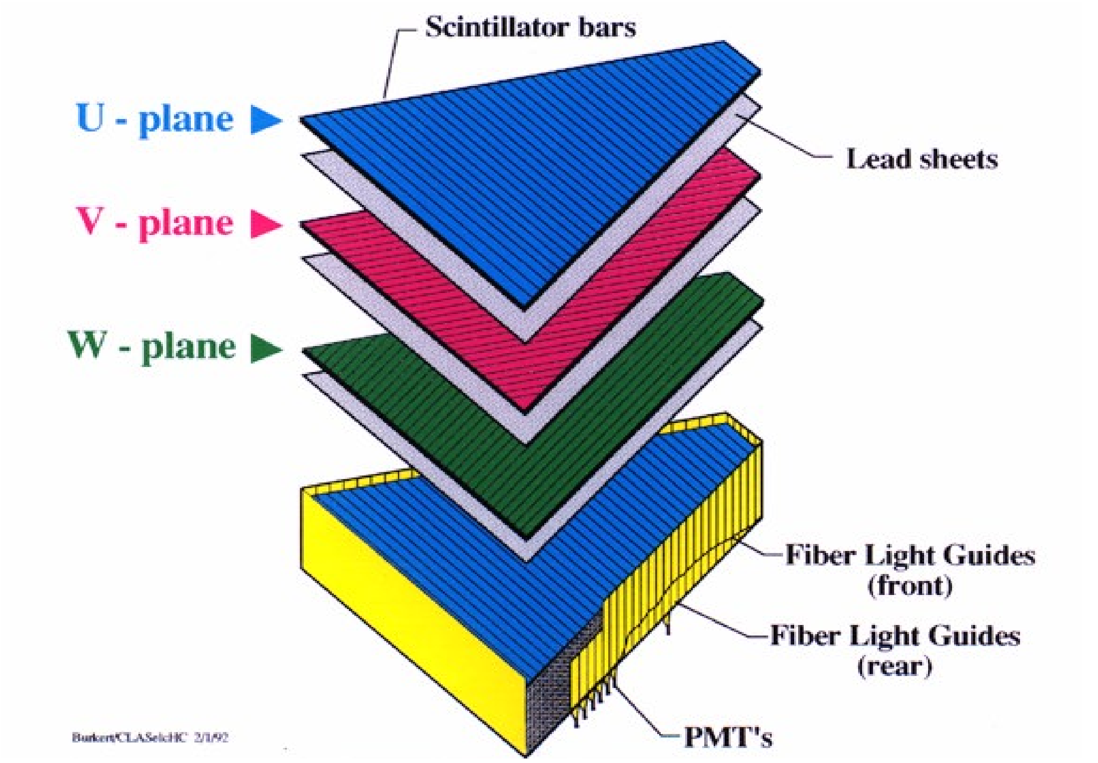

Figure 2.8. A cross sectional view of the CLAS electromagnetic calorimeters. The three orientations of the paddles described in the text can be seen in the pattern drawn on the U, V, and W planes.[31]

(5 layers) and outer (8 layers) stack to provide longitudinal sampling of the shower for better hadron identification.

In two of the six sectors of CLAS there are additional large angle electromagnetic calorimeters which extend the scattering angle coverage to 70°. These detectors, however, were not included in the trigger for the E1C data set and were also not used in any of the analysis. For those reasons they are not described in this thesis.

For more information about the CLAS electromagnetic calorimeters please consult Ref. [31].

Table 2.1. E1C Trigger Thresholds

System	Threshold(in mV)	Threshold(in GeV)
EC	80(145)	0.308(0.358)
CC	20	< 1 photo electron

2.4.6 Target

During the E1C run period, two different liquid hydrogen targets were used. The first target, a 50 mm long Al cell with a wall thickness of 150 μm and a window thickness of 1.0 μm, was used from February 8, 1999 to February 26, 1999. This target was kept at a temperature of $\sim$ 18 K and a density of 0.0730 g/cm^3. The second target, a 38.0 mm long Al cell, was used from February 28, 1999 to March 7, 1999. This second target had a wall thickness of 120 μm, a window thickness of 1.6 μm, and was kept at a temperature of $\sim$ 20.5 K and a density of 0.0695 g/cm^3.[32]

Numerous empty target runs were taken throughout the experiment to provide data to quantify the contributions of the target walls.

2.4.7 Data Acquisition System and Trigger

For this experiment, CLAS triggered on an intrasector coincidence of the CC and EC. The thresholds for this data set are summarized in Table 2.1. The EC energy thresholds are determined by multiplying the EC threshold in mV by the EC sampling fraction of 2.47. For most of the E1C data set the threshold for the running period was 80 mV. Midway through the 4.4 GeV 87% field run the threshold was changed to 145 mV. For this reason that particular beam energy and torus setting was not used in the analysis. Due to resolution effects, a higher EC energy threshold for electron identification is applied in the software, and will be discussed in greater detail in Sec. 3.3.1.

The intrasector coincidence between the CCs and the ECs was used to initiate a data acquisition readout of all of CLAS. During readout, the time-to-digital converter (TDC) and analog-to-digital converter (ADC) information from each detector component were reformatted to BOS data structures. BOS is a program system written in FORTRAN for the dynamic management of data areas and the input/output of sets of data areas [33]. Motorola Power PCs, which act as crate controllers for the VME and fastbus crates, performed these conversions. The fragments from each of the read out controllers (ROCs) are then sent to the part of the CODA(CEBAF Online Data Acquisition) 2.0 software package called the Event Builder. The Event Builder gathers all of the event fragments from each detector element and joins them together to form a complete event.

The events are then passed onto a large block of shared memory known as the Data Distribution (DD) ring. Online monitoring programs also attach to the DD ring to access the data while it is still in local memory. These programs give shift workers a real time indication of the quality of the data, as well as the health of CLAS. For example, CED (CLAS Event Display) reproduces a visual representation of which CLAS elements were activated for a given event. Online RECSIS samples events from the DD ring and quickly analyzes them online. Additionally, the monitor program histograms the TDC and ADC information from each detector component.

The last member of the DD ring is the CODA Event Recorder which writes events from the DD ring to a set of four 30 GB redundant array inexpensive disks (RAIDs). When one of these disks becomes full, subsequent data is written to one of the empty RAID disks. The data from the full disk is then archived to the JLAB tape silo through a fiber optic cable. This combination of writing and archiving ensures that data taking is never interrupted.

The E1C run period typically took data at an event rate of 2 kHz and a data rate of 8 MB/s. This resulted in an average DAQ livetime of $\sim 90\%$.

For more information on the Hall B data acquisition system please consult Ref. [34].

CHAPTER 3

RECONSTRUCTION

3.1 Overview

This section describes the method in which the CLAS reconstruction software package, *a1c*, analyzes raw data from the detector, constructs hit based and time based tracks, and eventually performs particle identification. Also included in this section are the additional particle and event identification cuts which were used to reduce the data to a set which included only $\Lambda(1116)$ events.

3.2 Track Reconstruction

Since CLAS uses a 100% duty cycle electron beam, there is no direct measure of the start time for a given event. Instead, the start time must be calculated after a first pass at DC track reconstruction and matching to the outer detector elements. In the first part of this procedure, all tracks associated with a particular event are reconstructed through a process called hit based tracking. Results from hit based tracking are then sorted to identify an electron. The length of the electron's flight path and its reconstructed momentum makes it possible to calculate a start time for each physics event. Each track is then constructed again to account for the new timing information in a process called time based tracking.

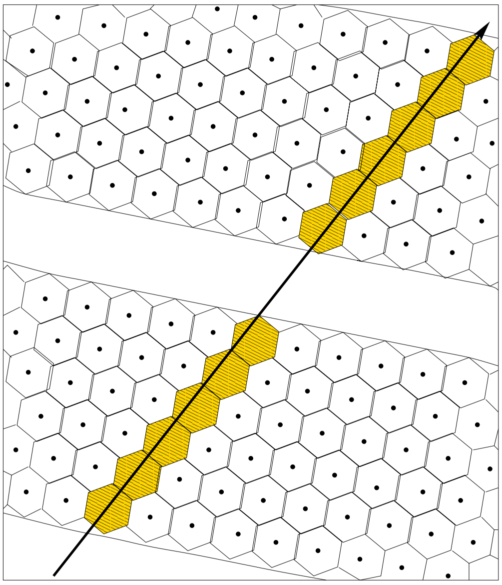

Figure 3.1. CLAS drift chamber hexagonal cell pattern. The edges of the hexagonal cells are simply shown to connect the locations of the field wires while the sense wires are shown as the black dot at the center of each cell. The gold shaded DC cells are the ones which are triggered by the charge track trajectory shown.

3.2.1 Drift Chamber Tracking

In hit based tracking, charged particle tracks are assumed to traverse the exact wire positions of hit drift chamber cells, as shown in Fig. 3.1. These wire positions are then combined into track segments within the individual superlayers of the DC. These superlayer segments are linked together from the three DC regions of each sector to form a track. Comparing the track to a special track dictionary determines the approximate momentum of the particle. This dictionary is created by simulating charged particles of different momentum traversing the three regions of the drift chamber. The track parameters for these simulations are stored in a database indexed to the momentum of the simulated particle. Due to the small drift cell size and the large number of wires, the resolution of the momentum of the particle after this stage of tracking is already of the order of 3-5% [28].

Using timing information from the electron track from each event allows for even better momentum resolution to be achieved. This is done in time-based tracking by calculating the time it took electrons freed by ionization in the DC to drift from a charged particle's path to the nearest sense wire. This drift time is given by the following equation:

$$t_{drift} = t_{start} + t_0 - t_{TDC} - t_{flight} - t_{prop} - t_{walk} \tag{3.1}$$

Eq. 3.1 uses the event start time, $\mathrm{t_{start}}$, as determined by the electron track; the fixed timing delay for the DC wire, $\mathrm{t_0}$; the raw time measured by the SC TDC, $\mathrm{t_{TDC}}$; the flight time of the particle from the reaction vertex, $\mathrm{t_{flight}}$; the signal propagation time along the wire, $\mathrm{t_{prop}}$; and the time-walk correction for short drift distances due to different ionization rates for slow and fast particles, $\mathrm{t_{walk}}$. The TDC value is subtracted because the TDC cards are operated in common stop mode. Through an appropriate function, the drift time determines the distance-of-closest-approach (DOCA) of the particle's trajectory to the closest sense wire. However, even with this information, there still exists an ambiguity as to whether the hit occurred to the left or right of a given sense wire. This ambiguity is resolved within the individual superlayers by comparing the χ^2 values of track fits for all possible combinations of drift distance signs for each hit drift cell. These new superlayer segments are again linked across the three regions of the DC and a final fit is determined for each charged track.

3.2.2 Outer Detector Matching

In hit-based tracking, the reconstructed tracks are projected to the outer detector components in an attempt to match the reconstructed hits in each of those elements. Each of these detectors has its own requirements as to what is considered a good track match. For example, the three orientations of the EC components allow the reconstruction of both a ϕ_{Lab} and θ_{Lab} angle for a given hit candidate. In this case, the track is considered a good match to the EC if the reconstructed track from the DC extrapolates to within 30 cm of the EC reconstructed hit along each of the three possible orientations. In the SC system, the width of each individual paddle constrains the θ_{Lab} angle of a particular track, and the PMTs at either end of each paddle also allows a measurement of the ϕ_{Lab} angle of each track. Such a ϕ measurement, however, would be very sensitive to the calibration, and is therefore not utilized by CLAS. As a result, a track is considered a good match to the time of flight system simply if the track candidate falls within 30 cm along the z axis of a hit in the SC. The optics of the CC system, on the other hand, are not configured to measure the ϕ_{Lab} direction of a reconstructed hit. A reconstructed track must therefore simply project to within 10° of the θ_{Lab} of a reconstructed hit in the CC to be considered a good match.

3.3 Particle Identification

After the track parameters are reconstructed for each detector element, most of the particle identification is done by the PART software package of *a1c*. The PART identification scheme is a first pass at identification, and a more comprehensive set of cuts must be used to obtain a credible set of events for an analysis of a specific reaction. The following subsections will describe the complete particle identification requirements for this analysis. The additional cuts which have been made to further reduce the data sample to $\Lambda(1116)$ events will also be described in detail.

3.3.1 Electron Identification

As mentioned in Sec. 3.2, to identify an electron, the hit based tracks are sorted in the following order:

1. momentum (-)

2. charge (+)
3. Match to EC (-)
4. Match to CC (-)
5. Match to SC (-).

The (-) and the (+) notation reflects whether the sorting order is descending or ascending, respectively, for that particular category. For example, the tracks are sorted first in descending order of their momenta and then in ascending order of their charge. Using this method, the top particle, which will be used to determine the event start time, is the negatively charged track with the largest momentum and the best match to the EC, CC, and SC. The SC is the last sorting requirement since the particle sorted to the top of the event will be used for the event start time. Based on an analysis performed by R. Thompson [36], this routine failed to correctly identify an electron only 0.38% of the time.

The second requirement for electrons in the PART scheme is that the electron track falls within the fiducial boundary of the EC. The term fiducial refers to a region of the detector where the acceptance is well understood. Due to the inclusive trigger used during the E1C run period, showers from electrons at the very edge of the calorimeter generate triggers. The shower from these events, however, is truncated and therefore difficult to accurately reconstruct. To avoid such acceptance problems, the PART identification scheme places a conservative fiducial cut on the track of the electron that requires the track to fall at least 10 cm from the edge of the EC elements along the u,v, and w projections. Note that this cut is in addition to the track matching EC cut mentioned in Sec. 3.2.2.

Requirements are also placed on the manner in which energy is deposited in the EC. Since to a good approximation the electron energy should be equal to the electron momentum, a cut can be placed around the total energy deposited in the EC versus

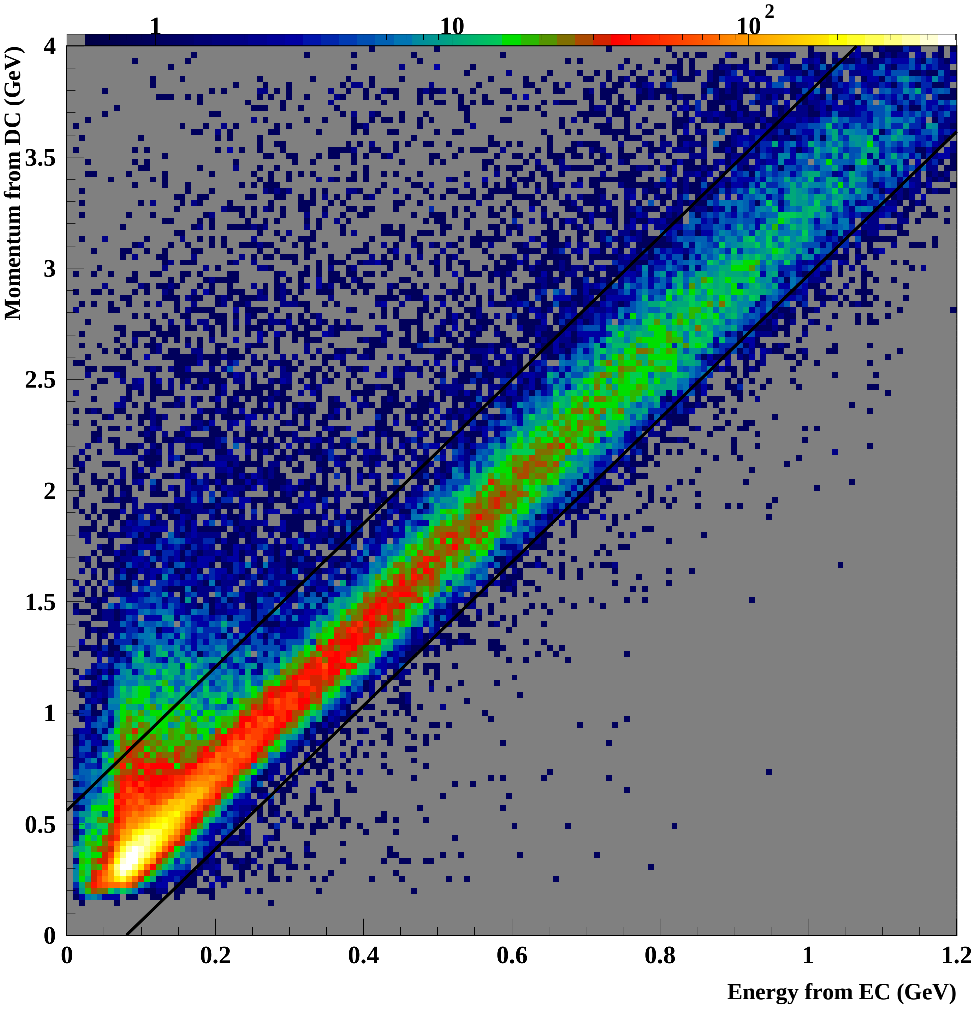

Figure 3.2. The energy deposited in the EC for negatively charged particles plotted versus the momentum for these particles as determined by the DC. The lines shown are the cuts used by the PART identification scheme to select electrons. The enhancement at an energy of about 0.1 GeV is due to high energy pions. Other cuts employed reduce this source of background.

the particle momentum as measured by the drift chamber. For negative particles with a good match to the Cerenkov detector and a fiducial match to the EC, Fig. 3.2 shows the particle's momentum determined from the DC versus the total energy the particle deposited in the EC, as well as the cuts placed around these good electrons. Numerically, the momentum of the track must satisfy the condition

$$3.23 * E - 260\,\text{MeV} < p < 3.23 * E + 560\,\text{MeV} \qquad (3.2)$$

where E is the total energy the track deposited in the calorimeter, p is the momentum of the track as measured by the drift chambers, and 3.23 is the inverse of the calorimeter sampling fraction. The events distributed above the upper momentum cut are events whose shower has been truncated by the edges of the EC so that even though they were still inside the fiducial region of the EC, their energy could not be accurately reconstructed. The horizontal enhancement at an EC energy of around 0.1 GeV is the result of negatively charged pions which will be further diminished by the next cut.

At the energies used in this experiment, electrons in the EC lose energy primarily through pair production and the subsequent showering reactions. Pions, on the other hand, will interact via ionization, and the energy they deposit is nearly independent of the pion energy. As a result, the manner in which pions and electrons deposit energy in the EC will have different signatures. In practice, pions will typically deposit $\sim$ 29 MeV in the inner stack of the EC, while electrons showering in the inner stack invariably deposit more than 80 MeV[36]. As a result, a

$$0.045\,GeV < E_{\mathrm{EC_{Inner}}} \tag{3.3}$$

cut on the energy deposited in the inner layer of the EC was used in the PART scheme to further separate pions from electrons. Figure 3.3 shows this cut and its intersection with the energy deposited in the inner layer of the EC for negatively charged particles. The concentration of events to the left of the line in Fig. 3.3 is the signature of negatively charged pions.

As mentioned previously, in addition to the PART scheme, cuts must be placed on electron candidates based on E1C specific run conditions. For example, for a given EC hardware threshold value, the reconstructed electron energy spectrum should sharply cutoff at the corresponding energy value. This, however, is not the case since amplitude fluctuations of the EC response are not sharp, leading to a distortion of the energy spectrum near threshold. As a result, a software cut is placed on the electron

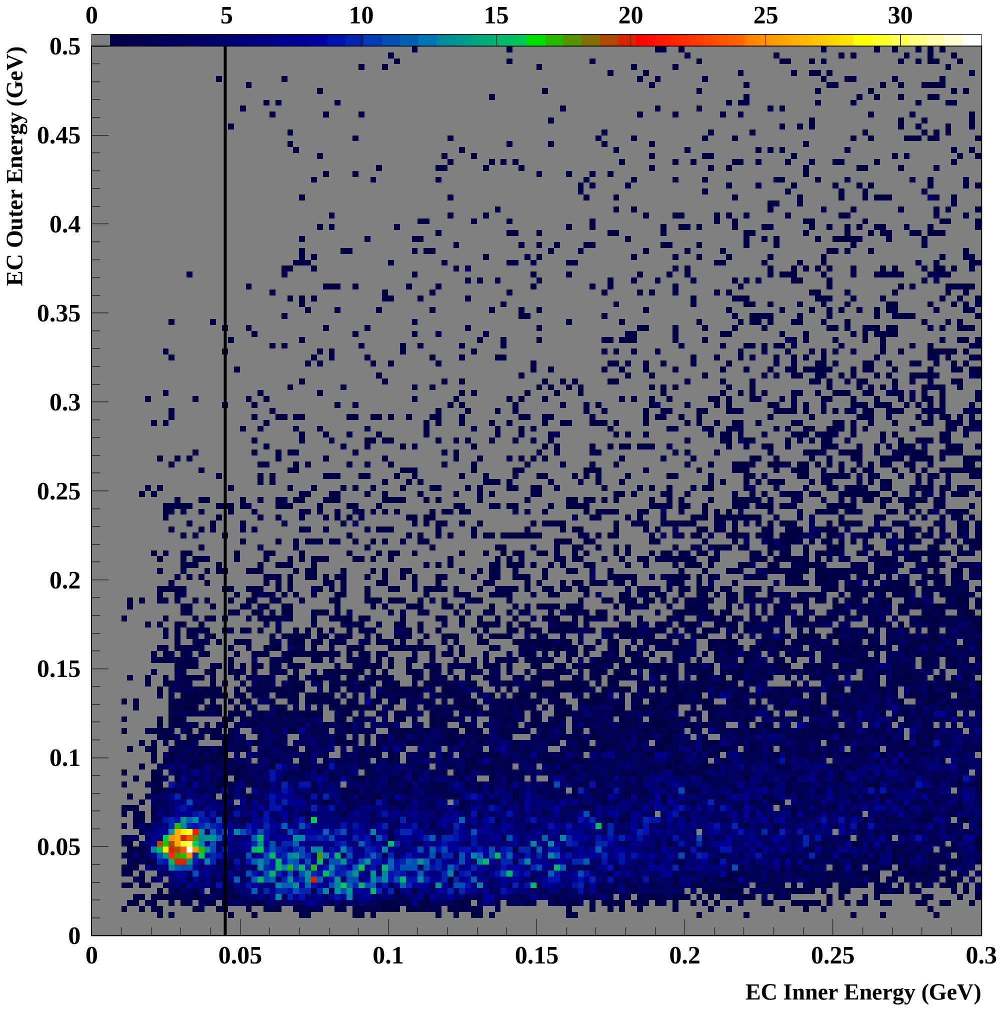

Figure 3.3. The energy deposited in the inner layer of the calorimeter for negative particles is plotted versus the energy deposited in the outer layer of the calorimeter. The concentration of events below 0.5 GeV are the minimum ionizing π^- tracks. The line shows where the electron identification cut is made at 0.045 GeV.

energy in order to minimize these effects. K. Egyian [37] made a determination of this minimal energy based on a study of inclusive electron scattering on a proton. The result of his study was an electron energy cut as determined by the following equation:

$$EEC(\text{in MeV}) = 214 + 2.47 * EC_{threshold}(\text{in mv}). \tag{3.4}$$

For the E1C data this led to an electron energy cutoff of 0.410 GeV.

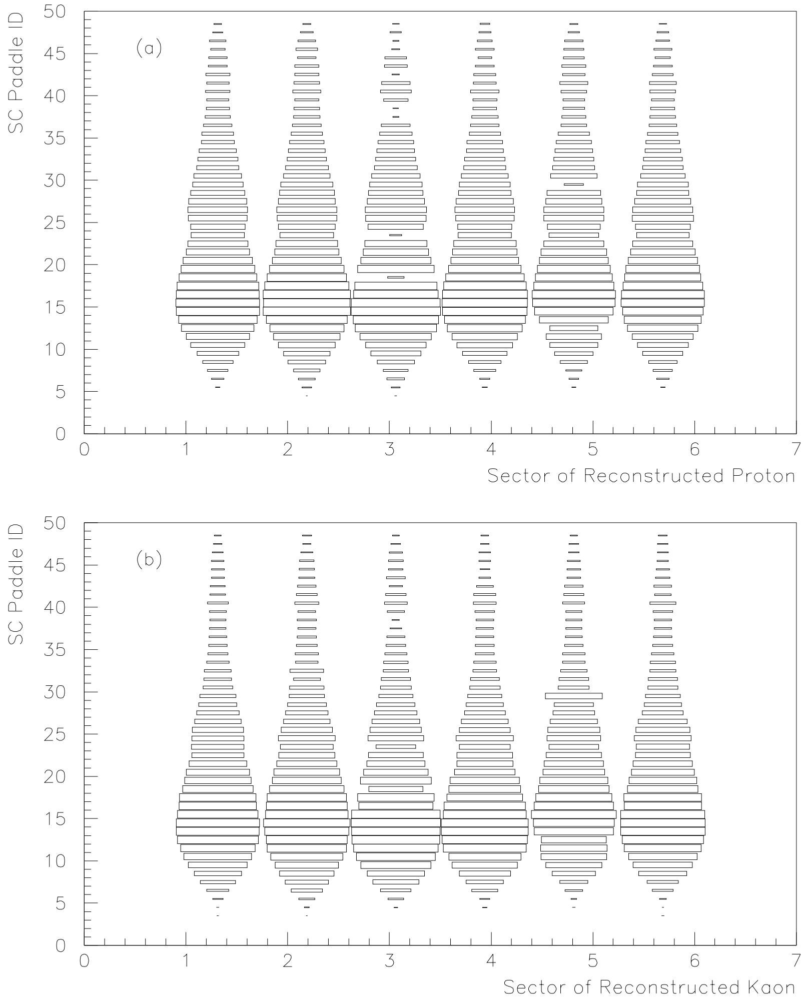

Figure 3.4. (a) SC Paddles matched with a reconstructed proton versus the sector in which the proton was reconstructed. (b) SC Paddles matched with a reconstructed positive kaon versus the sector in which the kaon was reconstructed. Using this format it is easy to find problematic SC paddles such as paddle 23 in Sector 3.

Cuts must also be made on the SC since some SC paddles malfunctioned during the E1C run period. In order to alleviate problems that might occur with simulating such performance anomalies, problematic paddles were dropped from the analysis. This is a fairly simple procedure since the symmetry of CLAS allows for consistency comparisons of the SC occupancy plots. A preliminary set of paddles was labeled as "bad" by the Time-Of-Flight group based on a detailed study of pion production. A

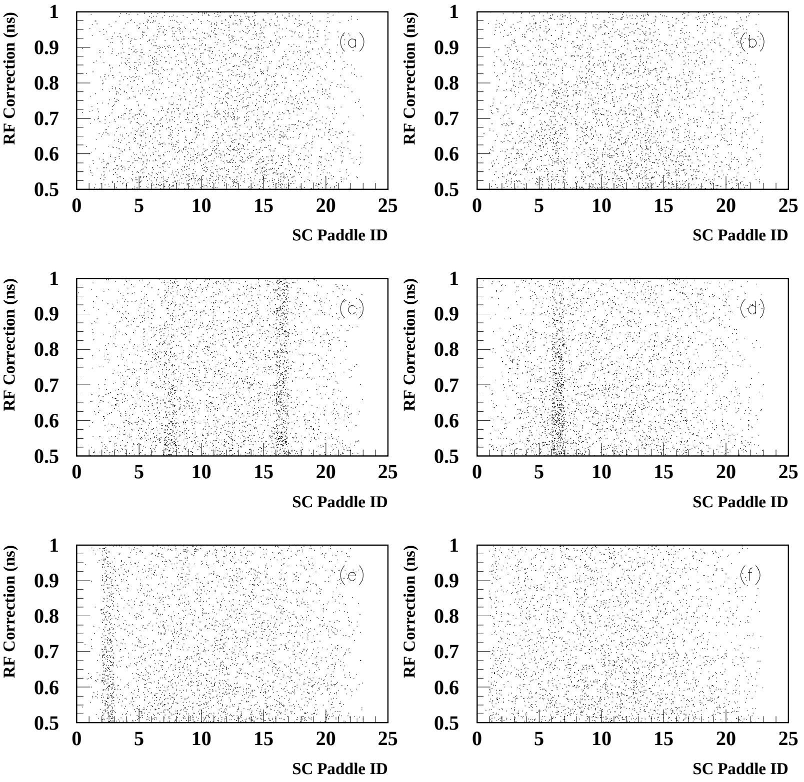

Figure 3.5. The RF correction versus the paddle hit by an electron for Sectors 1-6 are plotted in figures (a)-(f) respectively for the 2.5 GeV 40% field data. The large concentration of points in paddle 6 of sector 4, for example, suggests a problem with the RF calibration for this paddle.

similar study was performed on this data set using reconstructed protons and kaons. Figure 3.4(a) plots the sector in which the proton was reconstructed versus the paddle which the proton struck for the 2.5 GeV 40% data. The symmetric nature of the six sectors makes it is easy to see, for example, that the number of protons reconstructed in paddle 18 of sector 3 was greatly reduced compared to the other sectors. Similarly, Fig 3.4(b) shows an enhanced number of reconstructed kaons in paddle 29 of sector 5 relative to the other sectors. Some SC problems are a result

Table 3.1. Time of Flight Paddles Knocked Out From Analysis

Data Set	Sector 1	Sector 2	Sector 3	Sector 4	Sector 5	Sector 6
All	40, 41	44, 45	18, 23, 37, 38 42, 45, 46	21, 40	29, 40	26, 40
2.5GeV 40%	-	-	7, 16	6	2, 12	-
2.5GeV 60%	-	-	7, 16	6	2, 12	-
4.0GeV 60%	-	6	7, 16	6	2, 12	-
4.2GeV 60%	-	6	7, 16	6	2, 12	-

of calibration issues with individual paddles. For example, Fig 3.5 shows the RF correction versus paddle number for each of the six sectors for 2.5 GeV 40% data. This RF correction is an offset factor derived during calibration used to line up timing peaks. The same factor is applied uniformly for all paddles. Paddle 6 in sector 4 of Fig 3.5 shows a much higher concentration of events than the other paddles. For this reason, this and similar paddles are dropped from the analysis. Table 3.1 shows the complete set of SC paddles dropped from this analysis for each data set.

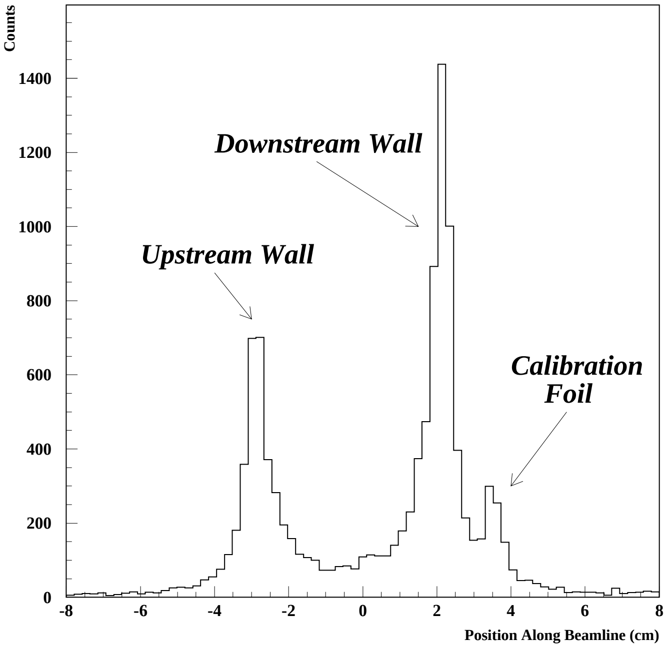

Figure 3.6. Reconstructed electron vertex position along the beamline for the 2.5 GeV 40% field empty target runs. Clearly visible are the upstream and downstream target walls as well as a foil placed in the beamline for calibration purposes.

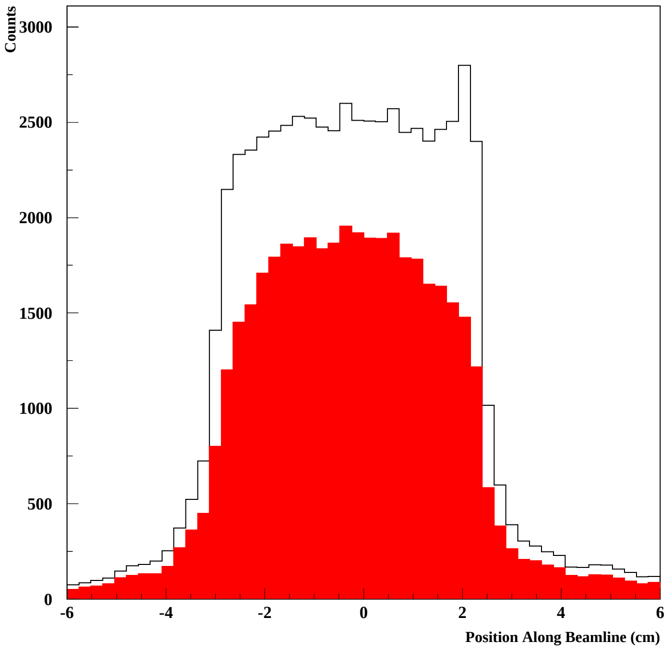

Figure 3.7. The solid line shows the vertex distribution of kaon tracks along the beam line for events which passed all cuts except an electron vertex cut for the 4.2 GeV 60% field data. The filled histogram plots the same kaon events which also passed an electron vertex cut placed exactly on the walls of the target. There is a substantial decrease in the number of kaons near the target walls in the filled histogram.

The reconstructed track as a whole may also be used to tighten the requirements for a good particle candidate. Through good angular reconstruction, for example, it is possible to fairly accurately reconstruct a track's position along the beam line. Fig 3.6 shows a plot of the electron's position along the beam direction for empty target data taken during the 2.5 GeV 40% run period. In this plot the walls of the target cell are easily identified. Preliminary analysis efforts tried to keep only electrons which were reconstructed within the target walls. A problem, however, appeared when such a cut was made. Fig. 3.7 shows a plot of the reconstructed K^+ vertex z-position along the beam line for a full liquid H2 target during the 4.2 GeV 60% field data. The solid line shows the kaon vertex position for events with electrons that passed all cuts except a vertex cut. The filled histogram plots the vertex position of kaons for events in which the electron also passed a strict vertex cut requiring it to fall exactly

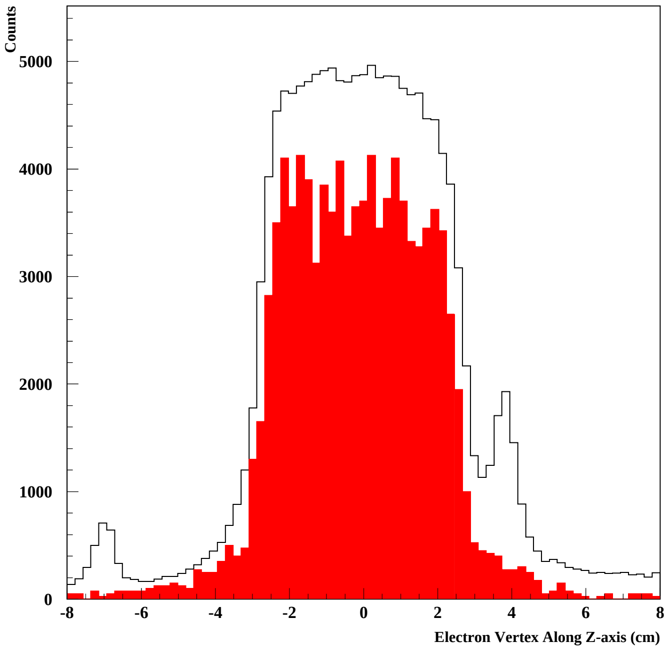

Figure 3.8. Reconstructed electron vertex position along the beamline for the 4.0 GeV 60% field production data. The solid line shows the vertex position for all electrons. For these events the two calibration foils are clearly visible. The dashed histogram plots a scaled histogram of the electron vertex for events using the -8.0 to 8.0 cm vertex cut for events with an identified "good" $\Lambda(1116)$. The two foils are no longer visible. The jaggedness of the dashed curve is due to the scaling procedure.

within the target structure. Based on this plot, it is clear that a tight cut on the electron vertex clearly throws away a number of good hadrons reconstructed within the target. As a result, a vertex cut was still imposed, but the cut now required an electron's z position along the beam to fall within -8.0 and 8.0 cm. An additional loose cut was placed on the reconstructed x and y positions of the reconstructed vertex origin to be within $x^2 + y^2 < 2.0\ cm^2$. Intuitively, it would appear that such wide cuts might be problematic. This, however, is not the case, as shown in Fig. 3.8 which plots with a solid line the electron's position along the beam line for the 4.0 GeV 60% data set. The two aluminum calibration foils installed along the beam line during this data set are clearly visible at -7.0 and 4.0 cm. The solid histogram in Fig. 3.8 shows the electron's position along the beam line for events which satisfy all of the conditions to be considered good $\Lambda(1116)$ events. In this plot, the calibration foils are clearly absent, even with the loose vertex cuts.

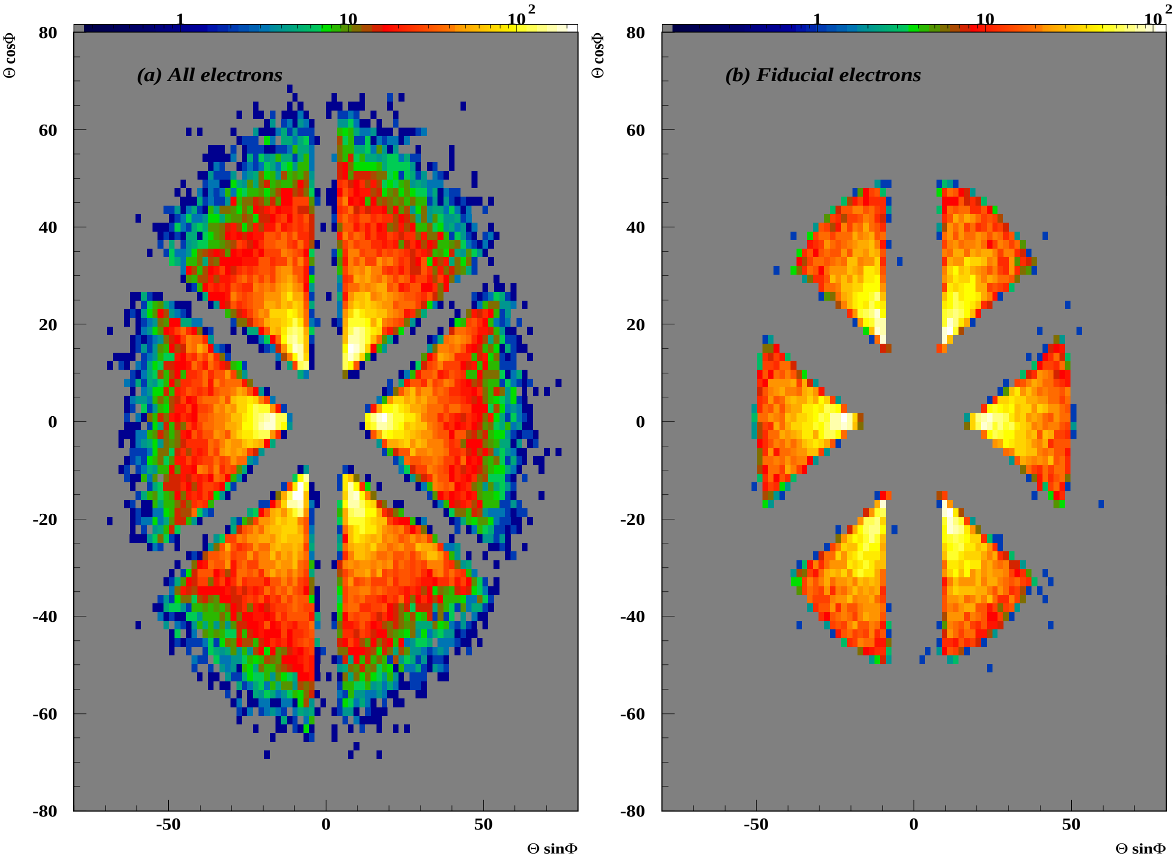

Figure 3.9. (a) The angular coverage for all electrons identified by the PART identification scheme in addition to the cuts on the time of flight counters. (b) The angular coverage of electrons which also passed the fiducial cuts.

Additionally, there is a cut on the electron that requires it to exist in another fiducial region of CLAS. This fiducial cut is different from the PART EC fiducial cut and is based on a study performed by V. Burkert. This fiducial cut eliminates regions where the exact calibration of the torus magnetic field is suspect. Figure 3.9(a) shows the laboratory azimuthal angle versus the laboratory scattering angle for all electrons while Fig. 3.9(b) shows the azimuthal angle versus the scattering angle for electrons satisfying the fiducial cut. This cut reduces the number of electrons used in this study by approximately half.

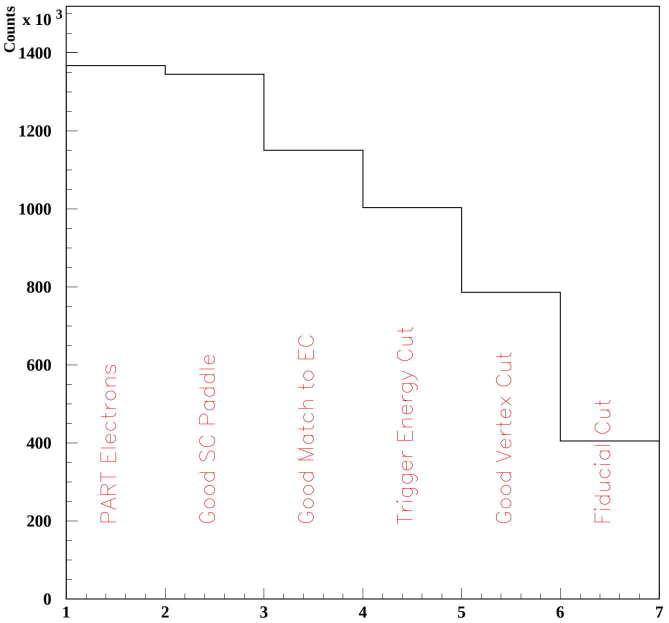

Figure 3.10. The number of electrons that survive each data reduction cut are plotted. Clearly the cut which has the largest effect on the data is the angular fiducial cut.

Figure 3.10 histograms the number of electrons in the 4 GeV data sets after each cut described in this section.

3.3.2 Hadron Identification

Once an electron track is identified, it is used to determine the start time for that particular event. The electron vertex time is calculated from the equation

$$t_{vertex} = t_{SC} - \frac{L}{c}, \tag{3.5}$$

where t_{SC} is the electron track time measured by the time-of-flight system, L is the distance the electron traveled from the vertex to the time-of-flight paddle, and c is the speed of light. This time, however, is further corrected by the radio frequency (RF) signal pulse that is synchronized to the beam bunches delivered to Hall B,

$$t_0 = t_{vertex} - (mod[t_{vertex} - rf + 200.4, 2.004] - 1.002) + \frac{Z_{vert}}{c} \tag{3.6}$$

where rf is the time of the RF signal and $\mathrm{Z_{vert}}$ is the position of the electron track along the z-axis of the beam line. The factor for the vertex position is added to compensate for target length effects.

After an event start time is calculated, a β is determined for each hadron track through the equation

$$\beta = \frac{L}{(t_{SC} - t_0) * c}. \tag{3.7}$$

The particle's mass is then determined through the relationship

$$m = \frac{|\overrightarrow{p}|}{\gamma\beta}, \tag{3.8}$$

where γ is $1/(1-\beta^2)^{0.5}$ and $\overrightarrow{p}$ is the track momentum as measured by the DC. Fig. 3.11 plots on a log scale the calculated masses for positive hadron tracks. The peaks identifying pions, kaons, protons, and deuterons are clearly visible. The mass cuts summarized in Table 3.2 are then used to identify the different types of particles in the PART system. As mentioned in Sec. 2.4.1.1, the bend of each track determines the charge of the particle.

Once a particle has been identified using the above mass cuts, it is assigned the mass attributed to that particle by the Particle Data Group (PDG) [22]. For example, each charged kaon is assigned a mass of 494 MeV. Using these nominal masses and the particle's momentum as measured by the DC, each particle's energy is determined through the equation

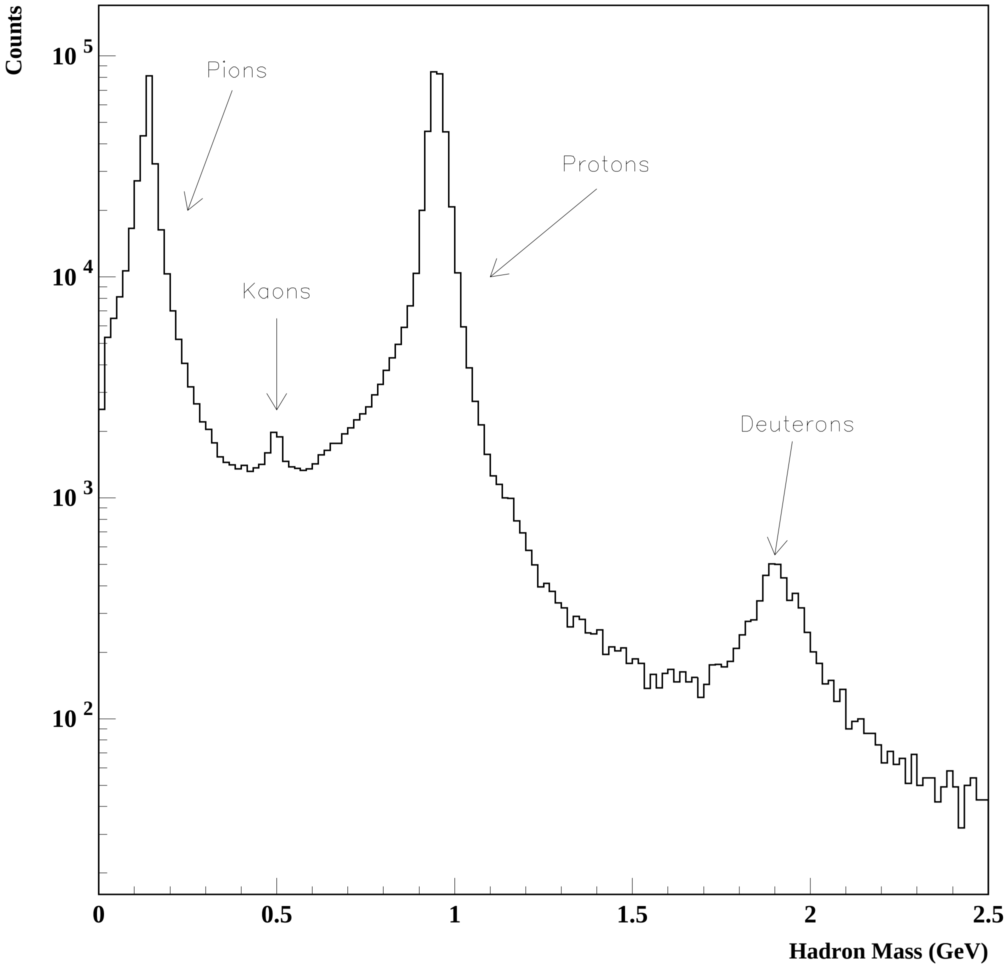

Figure 3.11. A log plot of the calculated masses of positive tracks. Clearly separable are the peaks for pions, kaons, protons, and deuterons.

$$E = \sqrt{m^2 + p_x^2 + p_y^2 + p_z^2}, \tag{3.9}$$

where p_x, p_y, and p_z refer to the particle's momentum projection along the x-, y-, and z-axes, respectively.

3.3.2.1 Kaon Identification

The PART mass cuts are not sufficient to cleanly identify real K^+ events for this analysis. Figure 3.12 shows the hadron mass distribution for a reduced data set which includes events containing an electron, proton, and K^+, as defined by

Table 3.2. PART Mass Cuts

Particle	Lower Mass Cut (GeV)	Upper Mass Cut (GeV)
Pion	0.0	0.3
Kaon	0.35	0.65
Proton	0.8	1.2
Deuteron	1.75	2.2

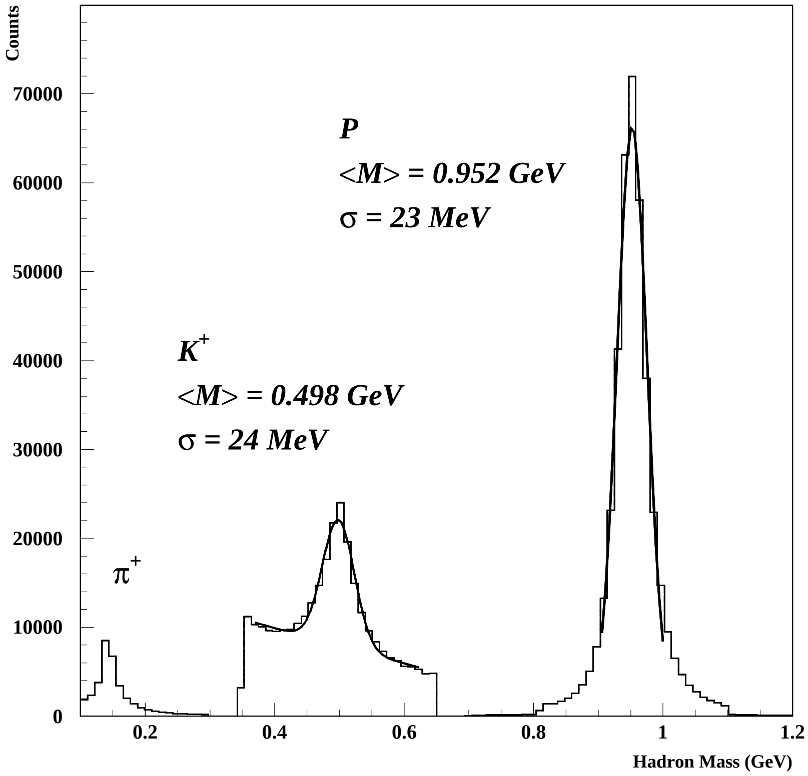

Figure 3.12. Hadron mass distribution for events which contain an electron, a kaon, and a proton based solely on the PART particle identification system.

the PART identification scheme. Although the proton distribution can be fit to a simple Gaussian with a resolution of 23 MeV, the kaon candidates sit on a substantial background. A fit for the kaon mass must therefore include a linear term as well as a Gaussian function. For low momentum kaons this background is due to protons. For the majority of events, though, the linear term is a result of high momentum pions. This is due to the fact that as particles approach the speed of light, CLAS's ability to determine the mass becomes limited. Figure 3.13 illustrates this effect by plotting the momentum distribution of positive hadrons versus their β. At a momentum of $\sim$ 1.25 GeV one can see the high momentum pions are bleeding into the kaon curve.

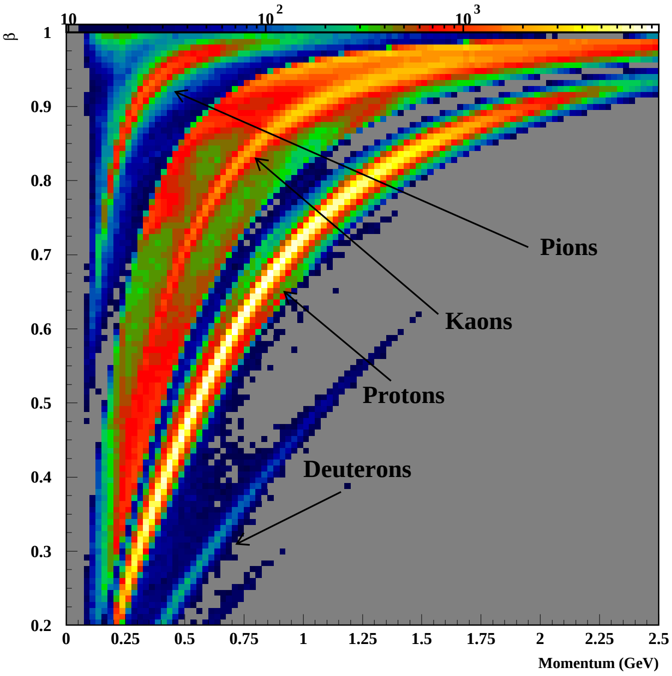

Figure 3.13. Hadron measured momentum versus β from the DC for the 4 GeV data. Although protons are cleanly separable from the other two particles at the momentum used in this experiment, the pions and kaons begin to mix at around 1.25 GeV.

It makes sense, therefore, to look at the kaon mass for various momentum bins. Figure 3.14(a)-(f) shows the kaon mass for different 0.4 GeV wide bins of the kaon momentum. As the kaon momentum increases, the resolution of the kaon mass peak gradually worsens until the disappearance of a signal for kaons with momentum between 2.0 and 2.4 GeV. For this reason, a maximum momentum of 2.0 GeV was established for kaon candidates for this experiment. Additionally, it is clear that a momentum dependent mass cut is necessary for the kaon candidates. This could be accomplished through the use of two methods. The first method involves binning the kaons for different momentum ranges, fitting each of those plots with a Gaussian and then making a 2σ cut around the kaon mass depending on which momentum bin the prospective kaon falls in. The second method is to use the knowledge of the

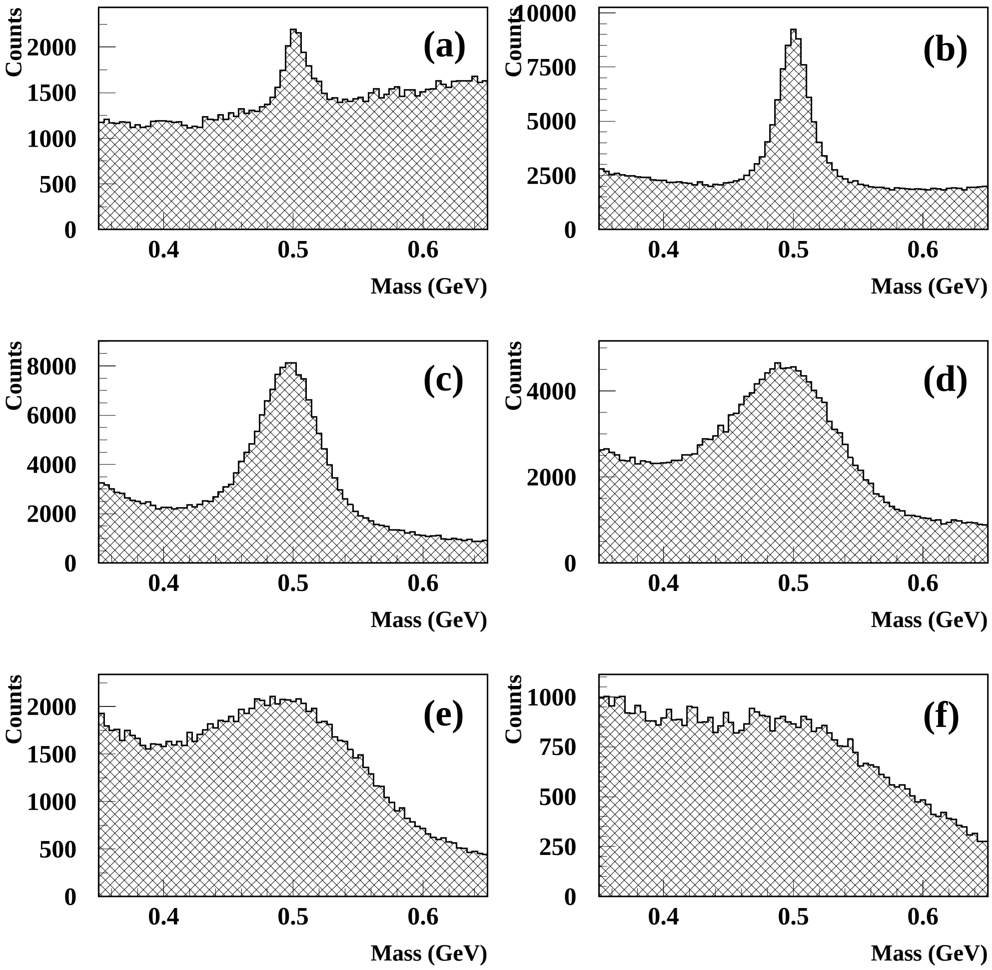

Figure 3.14. Kaon mass distributions for different bins of kaon momentum.(a) p < 0.4 GeV, (b) 0.4 < p < 0.8 GeV, (c) 0.8 < p < 1.2 GeV, (d) 1.2 < p < 1.6 GeV, (e) 1.6 < p < 2.0 GeV, (f) 2.0 < p < 2.4 GeV.

resolution of the time-of-flight system to create a continuous momentum dependent function describing the width of a mass cut. Such a calculation was performed by the SACLAY [38] group and gives the functional form of the mass cut as

$$\delta m = 4 * (0.005 + 0.00005 * p + 0.01 * p^2). \tag{3.10}$$

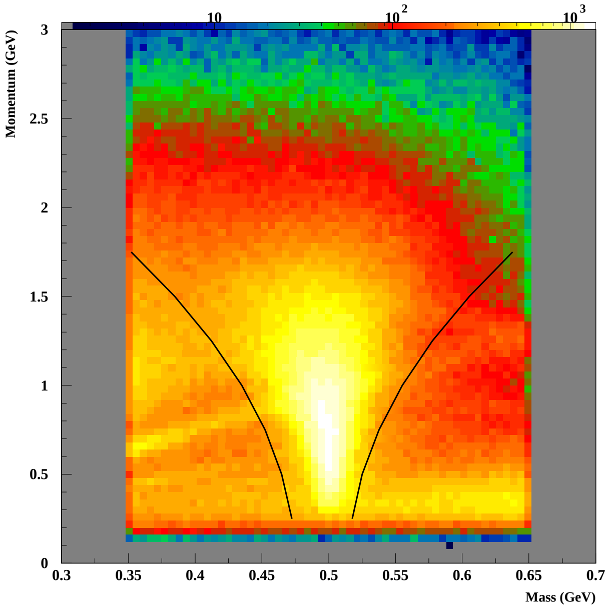

Figure 3.15. A log plot of kaon momentum versus mass. The curved lines on either side represent the momentum mass cut as described by Eq. 3.10.

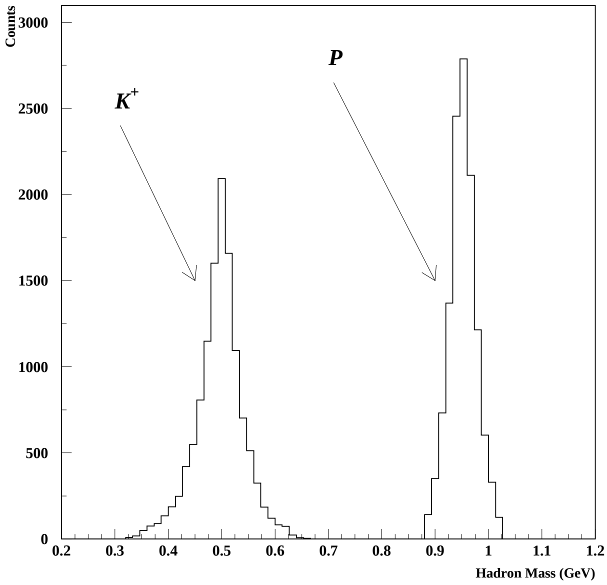

Figure 3.16. Mass distribution for positive hadrons in events in which a good $\Lambda(1116)$ event is identified according to all of the cuts specified in this chapter. The π^+ background under the kaon peak is no longer visible.

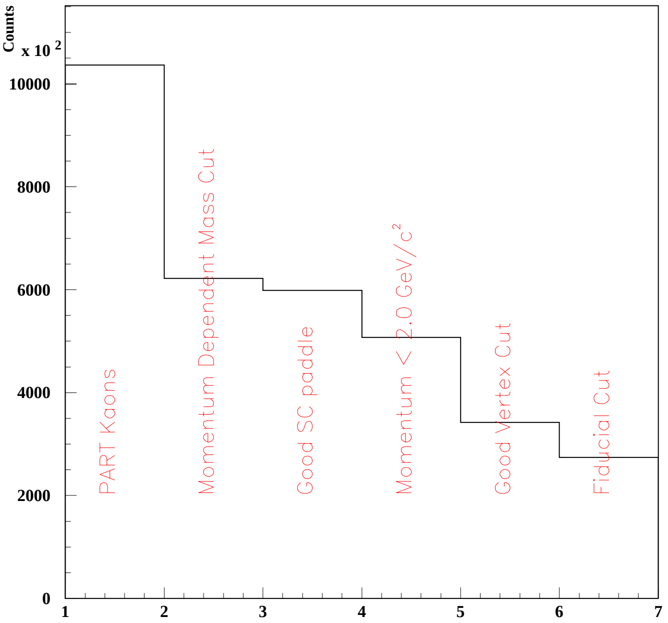

Figure 3.17. The number of tracks as a function of each kaon identification cut.

The mass centroid employed while using the mass cut on this data set was 0.5 GeV. This cut is shown as the solid lines in Fig. 3.15 and closely parallels a 2.5σ cut.

As is the case for electrons tracks, kaon tracks are only kept if they were also reconstructed in a fiducial volume of CLAS, have a good match to an SC paddle, were not reconstructed to one of the paddles labeled as bad in Table 3.1, and fall within the target vertex cuts. Although these cuts intuitively might seem minor, the cumulative effects of the cuts on $\Lambda(1116)$ events described in this chapter produce a clean kaon peak devoid of most background as can be seen in Fig. 3.16, which plots the hadron masses identified as containing $\Lambda(1116)$ production.

Figure 3.17 summarizes the reduction in the number of kaons for each particle identification cut.

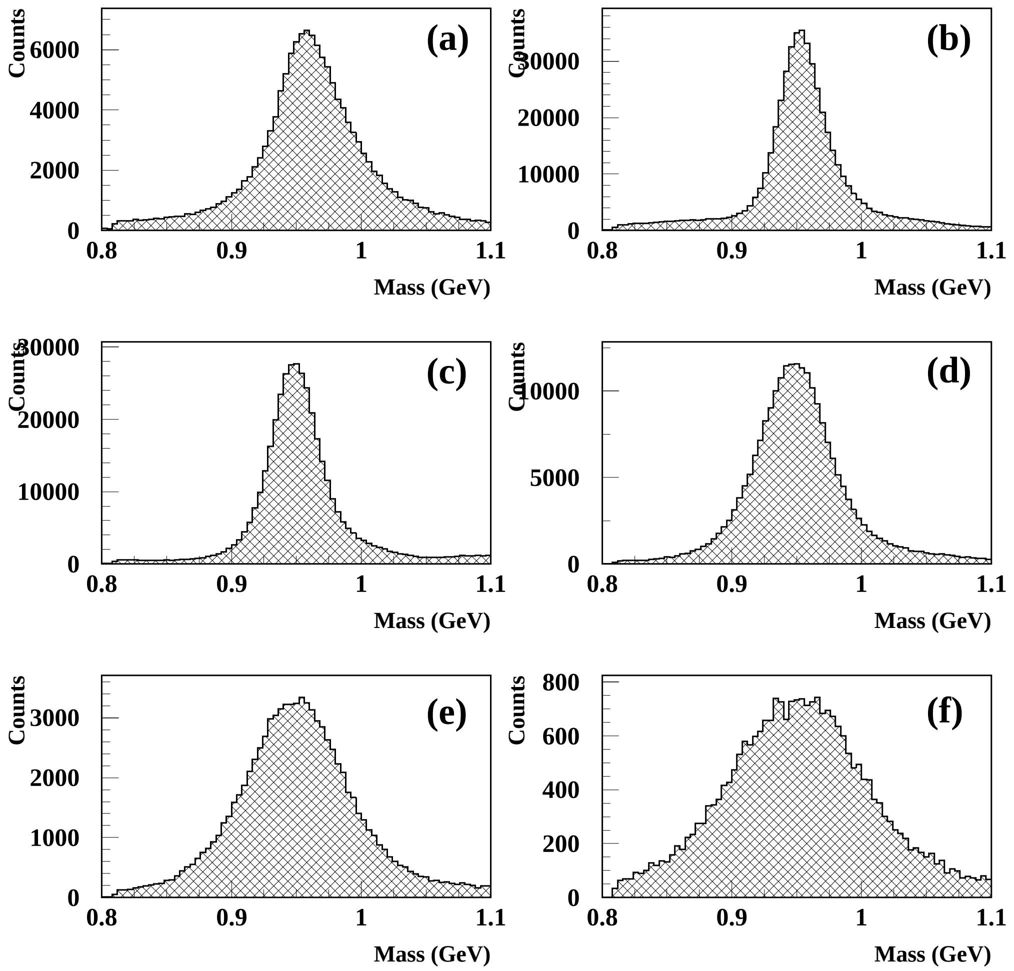

Figure 3.18. Proton mass for different momentum bins. (a) $p < 0.4$ GeV, (b) $0.4 < p < 0.8$ GeV, (c) $0.8 < p < 1.2$ GeV, (d) $1.2 < p < 1.6$ GeV, (e) $1.6 < p < 2.0$ GeV, (f) $2.0 < p < 2.4$ GeV.

3.3.2.2 Proton Identification

The PART mass cut for the protons was too large for this analysis. As can be seen in Fig. 3.12, the proton mass peak does not contain any appreciable backgrounds comparable to the one under the kaon peak. Also, as is shown in Fig. 3.18, the proton mass resolution does not diminish as quickly as the kaon mass resolution for increasing particle momentum. A constant 2σ mass cut was therefore placed on the proton candidates. This cut, which is represented by the solid lines in Fig. 3.19, was determined through a Gaussian fit of the proton peak of Fig. 3.12 and requires the mass to be between 0.883 and 1.021 GeV.

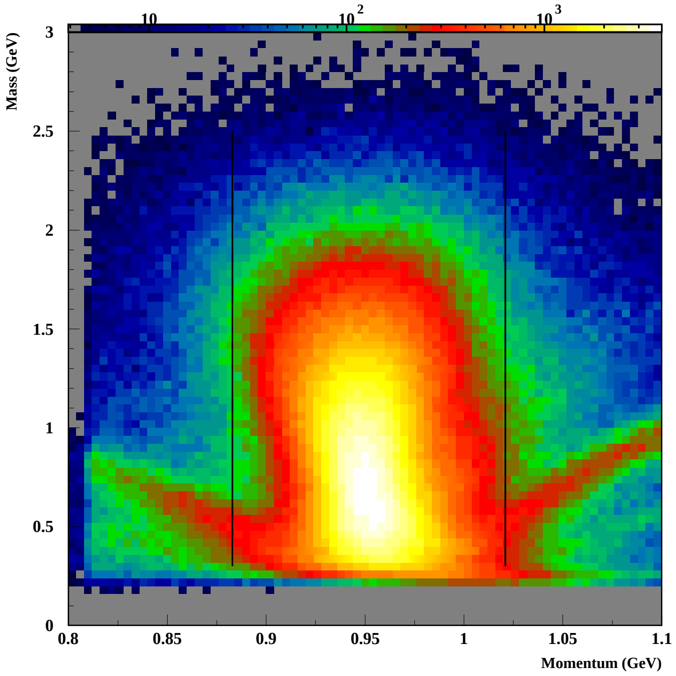

Figure 3.19. A log plot of proton mass versus momentum. The vertical lines represent the mass cut as described in Sec. 3.3.2.2.

One interesting feature in Fig. 3.18 is the fact that the mass resolution for the lowest momentum bin is worse than the resolution for the second lowest momentum bin. This is due to the fact that a dE/dx correction is larger for protons with momentum less than 0.4 GeV than for the higher momentum protons. A study of this correction factor will be presented in Sec. 5.5.2, but the main result of this study is that a minimum momentum cut of 0.45 GeV and a maximum momentum cut of 2.4 GeV were placed on proton candidates. The upper cut was placed on the data since this is the mass at which a 2σ momentum dependent cut around kaon candidates overlaps a 2σ momentum dependent cut around proton candidates.

Similarly to the electrons and kaons, protons are only kept if they are reconstructed in a fiducial volume of CLAS, have a good match to an SC paddle, and are not reconstructed to one of the paddles labeled as bad in Table 3.1. In this analysis, however, no cut is made on the reconstructed vertex of the proton. Since the $\Lambda(1116)$ decays weakly, there is a flight length of $c\tau \approx 7.89$ cm [22] before the creation of the proton. Thus, there is an offset between the initial event vertex and the point at which the proton vertex is reconstructed. Making a tight cut on the proton vertex is therefore counterproductive and may have unpredictable consequences.

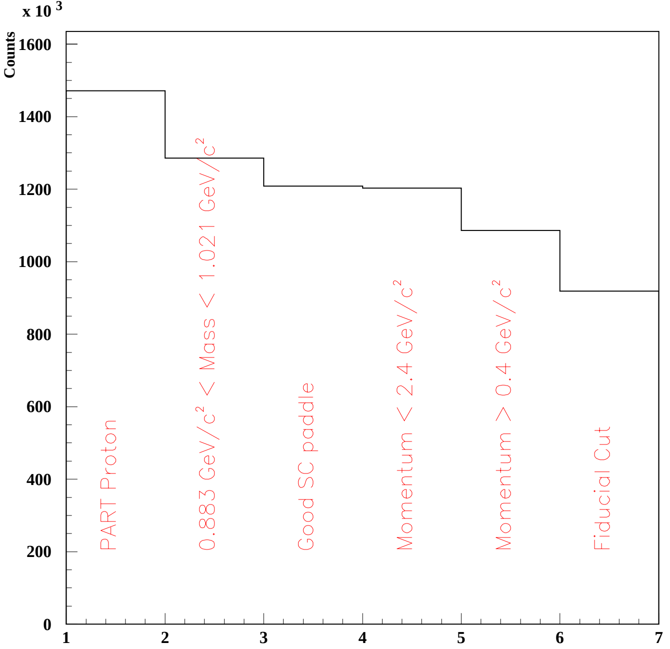

Figure 3.20. The number of proton events as each proton identification cut is applied.

Figure 3.20 plots the reduction in the number of protons for each particle identification cut.

3.3.2.3 Pion Identification

For a small handful of events, it is also possible to additionally detect the π^- from the $p\pi^-$ decay of the $\Lambda(1116)$. Due to the already limited statistics for these four particle events, severe cuts are not placed on pion candidates. A π^- is considered a good particle simply if its mass is between 0.1 and 0.2 GeV, it has a good SC match, it does not transverse one of the paddles labeled as bad in Table 3.1, and it is reconstructed in a fiducial region of CLAS. The mass cut was determined by looking at the π^+ mass in Fig. 3.12. The looseness of these cuts is not detrimental since the pion is not essential for the main analysis of $\Lambda(1116)$ polarization but is instead used later in the identification of bad $\Lambda(1116)$ events. This use is discussed in the next section.

3.4 Event Reconstruction

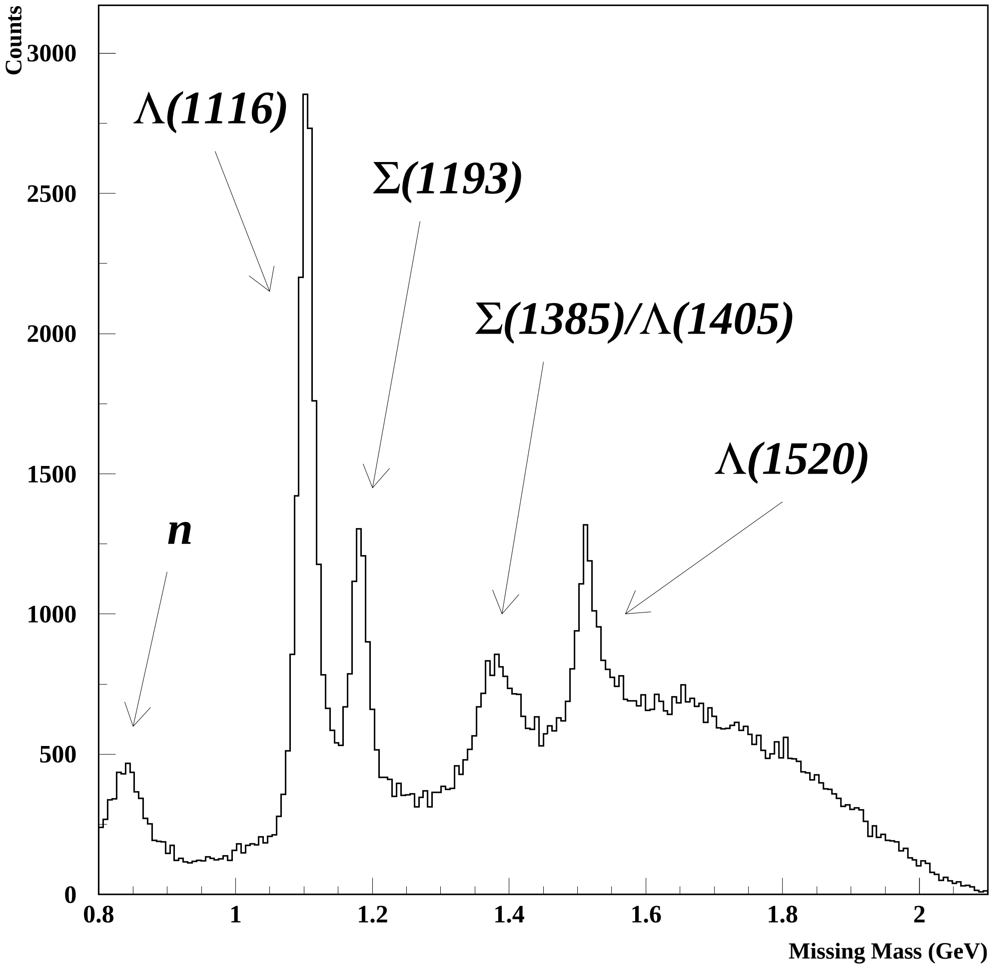

Figure 3.21. Missing mass from an electron and K$^+$ for events which contain a good electron and a good kaon. The neutron peak is due to events in which a π^+ was misidentified as a K^+.

Once the individual particles are identified, the requirements for good $\Lambda(1116)$ events can be established. The key method utilized is the missing mass technique, the definition of which can be found in Sec. 1.2.5. Using this technique, a missing mass spectra for events which contain both a good electron and a good kaon, according to the specifications described in Sec. 3.3, for a few runs from the 4.0 GeV 60% field data set, is plotted in Fig. 3.21. In this figure, a clean spectra for the lower lying hyperons is clearly visible. The peaks for the $\Lambda(1116)$, $\Lambda(1520)$, and $\Sigma(1193)$ are easily distinguished from the background. The resolution of CLAS and the chosen channel, however, does not allow for a clean separation of the $\Lambda(1405)$ and $\Sigma(1385)$ peaks. A neutron peak can also be seen due to events in which a π^+ track was misidentified as a K^+ track.

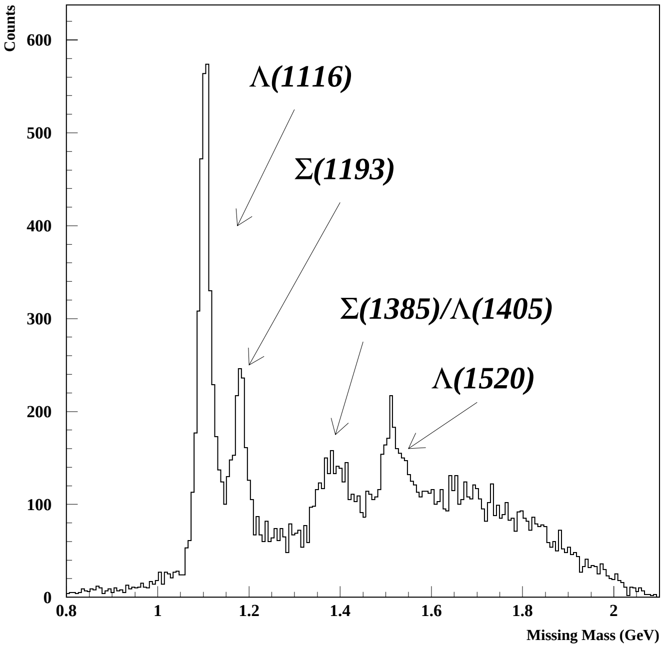

Figure 3.22. Missing mass from an electron and kaon for events with a good electron, good kaon, and good proton.

For the same data set, when the event also contains a good proton according to the requirements specified in Sec. 3.3, the neutron peak is removed from the electron-kaon missing mass spectra, as shown in Fig. 3.22. The presence of the proton also provides for a cleaner $\Lambda(1116)$ data set through the use of the squared missing mass from the detected electron, kaon, and proton, as plotted in Fig. 3.23 for

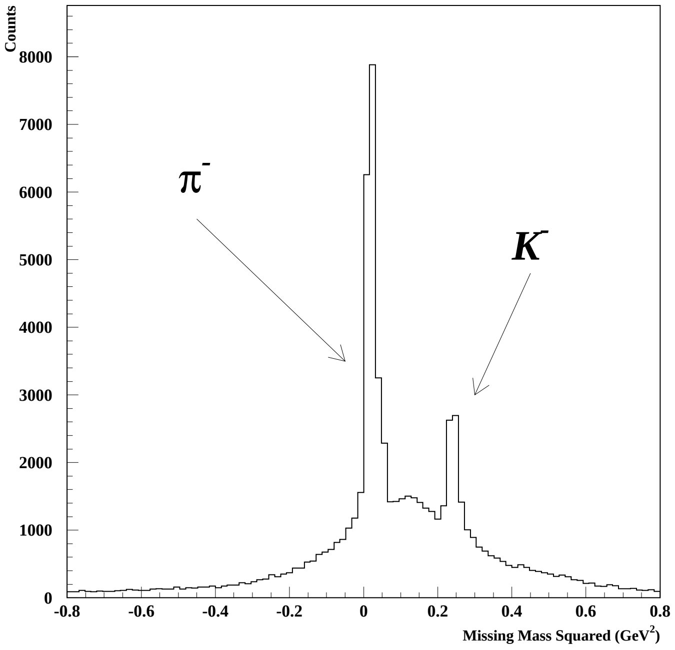

Figure 3.23. Missing mass squared from an good electron, good kaon, and good proton.

both the 4.2 and 4.0 GeV data sets. The squared value of the missing mass is used in this case since resolution effects alone could lead to a negative squared mass of the π^-. Two peaks are clearly visible, and separable, corresponding to a missing π^- and a missing K^-. The K^- events are mainly due to the decay of the $\Lambda(1520)$ through the branching ratio $\Lambda(1520) \rightarrow pK^-$. The π^- events result from the $\Lambda(1116)$ decay in which this thesis is interested. The underlying broad spectra is the result of some particle misidentification, but is mostly from other hyperons which decay into either the $\Lambda(1116)$ or the $\Lambda(1520)$. For example, the $\Sigma(1193)$ decays 100% of the time via the decay channel $\Sigma(1193) \rightarrow \Lambda(1116)\gamma$. The extra energy from this photon is one of the reasons for the tail on the squared missing mass of the π^-. A tight cut requiring the squared missing mass of the electron, kaon, and proton to fall between -0.01 and 0.03 GeV^2, is therefore placed on $\Lambda(1116)$ candidate events.

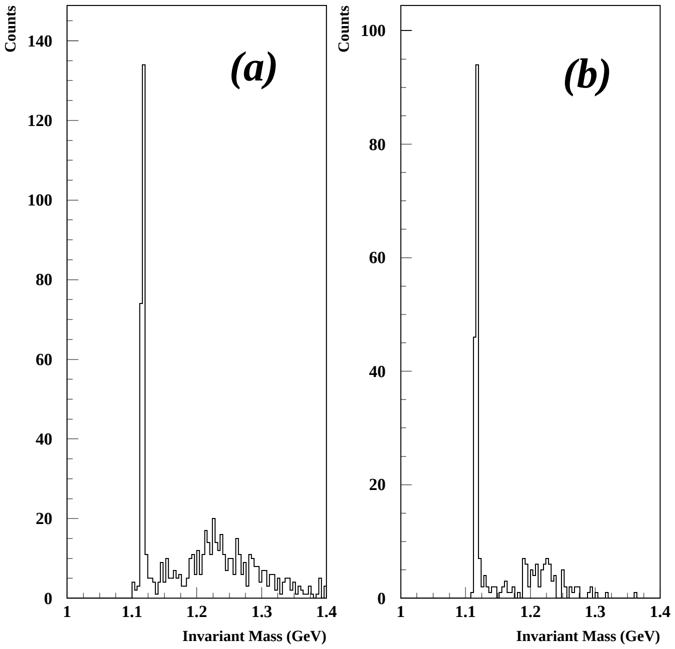

Figure 3.24. a) The invariant mass of the proton and pion for events which have a good electron, K^+, proton, and π^- as defined in Sec. 3.3. (b) The pπ^- invariant mass for events which additionally satisfied an electron-K^+ missing mass cut and an electron-K^+-proton missing mass squared cut. The background distribution at around in 1.225 GeV in (a) is clearly reduced in (b). Still these events are cut out of the final data sample.

As mentioned in Sec. 3.3.2.3, for a handful of events the π^- is also detected in CLAS. Figure 3.24(a) plots the invariant mass of the pπ^- pair for events which had a good electron, kaon, and proton according to the requirements set forth in Sec. 3.3. A very clear $\Lambda(1116)$ peak exists centered at 1.116 GeV. There is, however, another structure that appears to be centered around an invariant mass of 1.225 GeV. If cuts are placed around the electron-K^+ missing mass and the electron-K^+-proton missing mass squared for these same events, the second structure in Fig. 3.24(b) is greatly reduced. Still, for events which had a good pion, as defined in Sec. 3.3.2.3, in addition to the other three particles, a cut was applied requiring the invariant mass to be between 1.11 and 1.12 GeV.

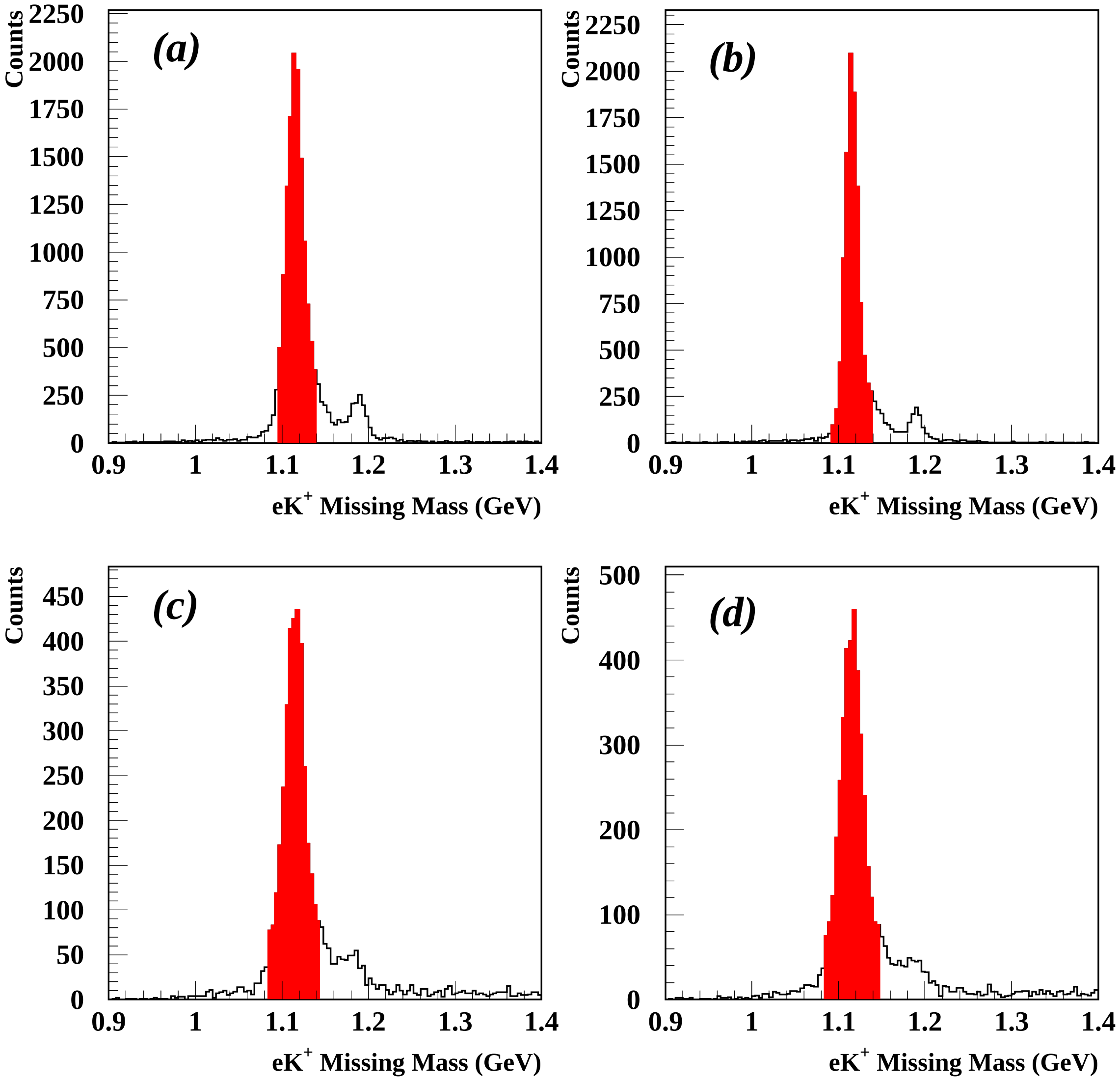

Figure 3.25. The electron-K^+ missing mass spectra are plotted for the (a) 2.5 GeV 40% field data, the (b) 2.5 GeV 60% data set, the (c) 4.0 GeV 60% data set, and the (d) 4.2 GeV 60% data set. The red highlighted area in each plot shows the events kept after the 2σ cut.

Table 3.3. Electron-K^+ missing mass cuts for $\Lambda(1116)$ events.

		$\Lambda(1116)$ Mass Cuts (GeV)	
Beam Energy (GeV)	Torus Current (A)	Lower	Upper
4.2	2250	1.086	1.146
4.0	2250	1.086	1.142
2.5	1500	1.092	1.139
2.5	2250	1.096	1.134

Figures 3.25(a)-(d) show the electron-K^+ missing mass spectra for the 2.5 GeV 40% field, 2.5 GeV 60% field, 4.0 GeV 60% field, and 4.2 GeV 60% field data sets respectively after the above cuts are applied to the data. The background events are clearly reduced from the previous missing mass spectra although a small $\Sigma(1193)$ peak is still visible in each spectra. The $\Lambda(1116)$ peaks for each data set are fit with for Gaussian distribution. A 2σ cut, summarized in Table 3.3, is then applied to extract the $\Lambda(1116)$ events. These events are shown in Fig. 3.25 by the red highlighted areas.

Figure 3.26 shows the reduction in the number of events as each particle identification cut is applied and then as the missing mass cuts are applied.

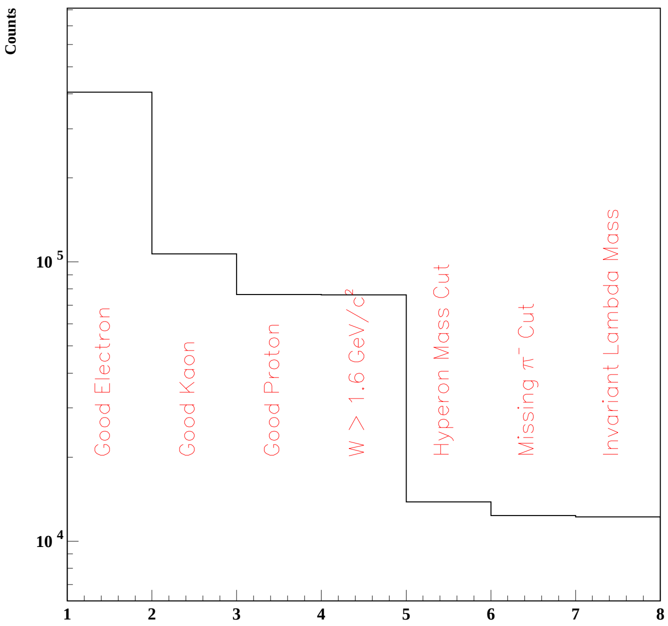

Figure 3.26. A log plot of the number of events which survive after each data reduction cut. The first three columns plot the number of events which contain that particle in addition to the particles mentioned previously.

CHAPTER 4

DATA PROCESSING

In the E1 experiment terminology, cooking refers to the process in which the data is calibrated, the quality of the reconstruction code assessed, and data reconstruction suitable as input to publishable physics analysis is performed. As in the typical usage of cooking, there are terms which must be understood before one can proceed. Therefore, the first two sections of this chapter define the terms important to cooking the E1 data. The first section of this chapter describes the two databases essential to the cooking process while the second section defines concepts important to cooking the E1 data set, such as tagging, freezing, and production libraries.

Once there is an understanding of the cooking terminology, there are a set of steps that must be followed carefully to produce publication quality data. For this reason, the sequence of operations performed, as part of this thesis, on the E1C data set are enumerated in the third section of this chapter. The fourth section gives a description of the computer hardware and software, including the scripts written as part of this thesis for the entire E1 experiment, to manage this task.

Pushing the cooking analogy one last time, when one gets a recipe it might not necessarily fit the particular requirements for your needs. As a result, some modifications may need to be made to produce the desired results, such as scaling down the amount of ingredients used. For example, the typical cooked file size is much larger than is necessary. As a result, the data files are passed through a few stages before being analyzed. These procedures will be discussed in the last section of this chapter.

For more detailed information about the cooking process than is presented in this chapter, one should consult Ref. [35].

4.1 Off-line Databases

The first database important to the production of quality data is the Mapmanager database, which stores the detector calibration constants derived for the data. For the majority of the information stored in this database, the values were obtained from separate calibration programs extraneous to the cooking scripts. The information in this database is stored in a time stamp method such that particular values can be requested by identifying a certain time or a particular run. If there is an entry for that run number in the database, that entry is returned. If an entry does not exist for that particular run, the value that is returned is the information for the last preceding run. The information in the Mapmanager database is stored in binary format. As a result, a number of scripts and subroutines have been written to allow users to create, access, or remove a database entry. When the software package for each of the independent detector systems is initialized, for example, the code usually has a call to retrieve the standard values from this Mapmanager database.

The second database, a relational database written in Perl commonly known as the off-line database, stores information about each cooked data file in an associative array key-value format. All the information stored in this database is derived solely from the cooking process. Examples of the information stored are the executable command lines used to run certain cooking processes or the location of the files that the cooking process produced. Additionally, the output from the cooking programs is parsed for useful pieces of information and stored in the off-line database. A full list of the variables stored in this database can be found in Appendix B of [35] along with a brief definition of each quantity.

4.2 Tagging, Freezing and Production Libraries

When processing large quantities of data, it is important to maintain a careful record of the procedures followed to maintain reproducibility. There are two techniques that are used in CLAS to ensure this type of reproducibility.

The first technique, tagging, utilizes CVS, a software repository that monitors all of the CLAS software. CVS keeps a log of the time dependence of the software source code. It also keeps track of who made changes to the software, what changes they made, and also any comments that the person making the change wanted to record. Thus, it is possible to check out all of the CLAS software to see how it looked at one particular moment in time. The ability to retrieve a particular version of the code is especially important when cooking the data. First, it allows one to track down possible bugs introduced into the analysis code. Secondly, CVS allows one to apply a meaningful name to a particular set of software in the technique known as tagging. For example, the code that was used to cook the E1C data was tagged PROD-1-9, which indicates that this release was the ninth version of the production libraries.

Equally important to the software are the detector calibration values that are stored in the Mapmanager database. As mentioned before, these values are called when initializing the software packages for each of the detector components. If different values are used to initialize the software, one would not be able to reproduce previous results. Unfortunately, CVS does not economically store binary files. Therefore, a copy of the Mapmanager database in its entirety is copied to two locations. The first location is the archive tape silo and the second location is a work disk where the database is accessed during cooking. After cooking begins these versions will not be altered in any way and the write permission will be removed from all of the files. In effect, the stored values are frozen.

4.3 Cooking Sequence of Operations

The first step of the cooking process, shown as a flow chart in Fig. 4.1, does not require the actual processing of any data. Known as “step 0”, this stage of the cooking concentrates on the detector calibrations that can be performed without the output of tracking. The goal of this stage is to calibrate the data to a high enough level to allow the determination of an acceptable start time for time based tracking. For example, the one photo-electron peak position for the CC may be determined from special calibration runs. Also, the time-walk corrections for the SC can be determined from TOF laser calibration runs [39].

Step 1 of the cooking process is used to refine the time based tracking calibration. Evenly spaced runs are selected from the run period and about 100K events from each of these runs is thoroughly processed using the full set of calibration and monitoring programs. In addition to allowing the calibration of the DC, this stage also allows users to assess the quality of the calibrations performed on the data in step 0. Additionally, the chefs, the people in charge of cooking the data, may assess the quality of the current version of the cooking scripts and reconstruction software if any changes have been made. At this stage of the cooking process, it is advantageous to find problems so that they may be corrected before a full scale first pass through the data is performed.

In Step 2 of the cooking, known as “Pass 0,” a more complete set of runs is chosen from the data in order to analyze enough events to fully calibrate the TOF system and provide a data set with which people can refine analysis codes and calibrations. At this time, the CLAS chef tags a version of the source code as the production library. From this tagged code, the chef builds the full set of executables which will be used to analyze the data. A version of the Mapmanager database is also frozen. The quality of the code and calibrations are then assessed in Step 3 of the cooking

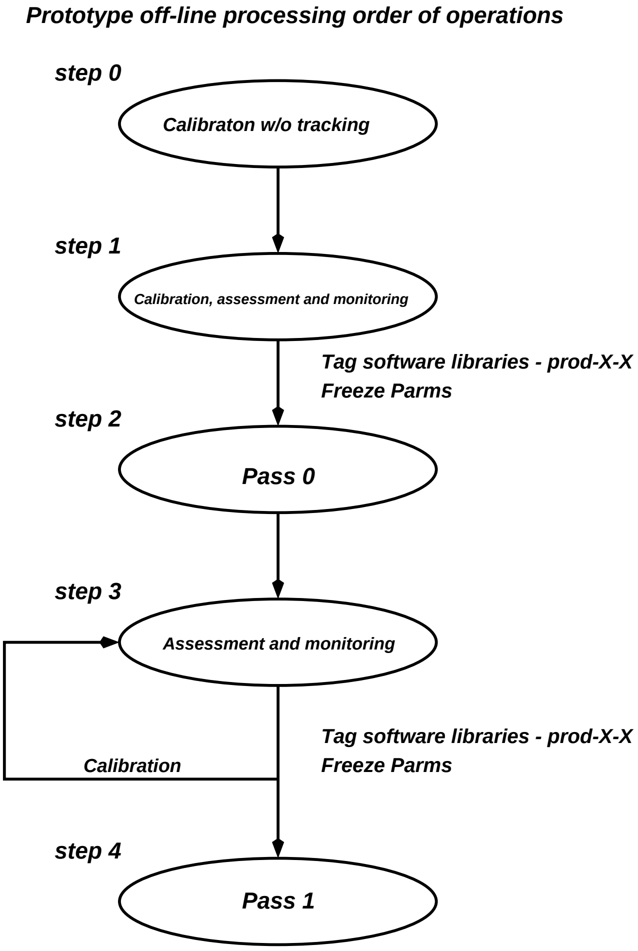

Figure 4.1. Flow chart for the production of cooked data [35]. Steps two and three may be repeated multiple times before the chef proceeds to step 4 or the Pass 1 cooking.

process. If the data is good, the cooking continues on to Step 4. If the data is bad, the chef repeats Steps 2 and 3 until the run group is satisfied with the results.

Step 4 of the cooking is the "Pass 1" stage. At this point, the full data set is completely processed with no selection criteria. At the end of this stage, the run group examines the database entries for the full set of runs to decide on a list of runs usable in an analysis set. In E1C, the selection criteria for good runs was fairly simple. If hardware failure occurred at any time during a run, that run was labeled as a “silver” run. The rest of the runs were labeled as “gold” and approved for physics analysis.

4.4 Cooking Tools

4.4.1 Cooking Hardware

Data from the experiment are archived to a set of STK 9840 and STK Redwood tape drives. When these data files are cooked, they are copied from the tapes to a large cache disk and then to dual processor Pentium II machines running RedHat Linux, where they are processed. The seventy machines, which made up the JLAB off-line CPU batch farm, ran at CPU clock speeds between 300 and 500 MHz and had an 18 GB disk. While the E1C data was processed, the farm was configured such that no more than three jobs ran on each dual processor machine at one time. A diagram of the network layout for the JLAB off-line farm can is shown in Fig. 4.2.

Once a given farm node finishes processing an E1C data file, the cooked data files are written to tape while the diagnostic and filtered files are instead written to a 1 TB work disk. Since the diagnostic and filtered files are created to assess and summarize the quality of the cooking process, it is essential to keep them in a location easily accessed by the entire collaboration. When the space remaining on this work disk drops below 25%, though, these files are copied as a group to tape. By writing a large quantity of the monitoring files to the silo at one time, the overall load on the tape software and drivers is reduced. Writing the cooked files to the work disk, however, is not feasible since the large size of the cooked files from the farm causes the work disk to reach capacity before the files can be archived to tape.

4.4.2 Cooking Software

There are two distinct types of cooking software. The first type are the cooking scripts which do no actual physics analysis. Instead, these scripts define the

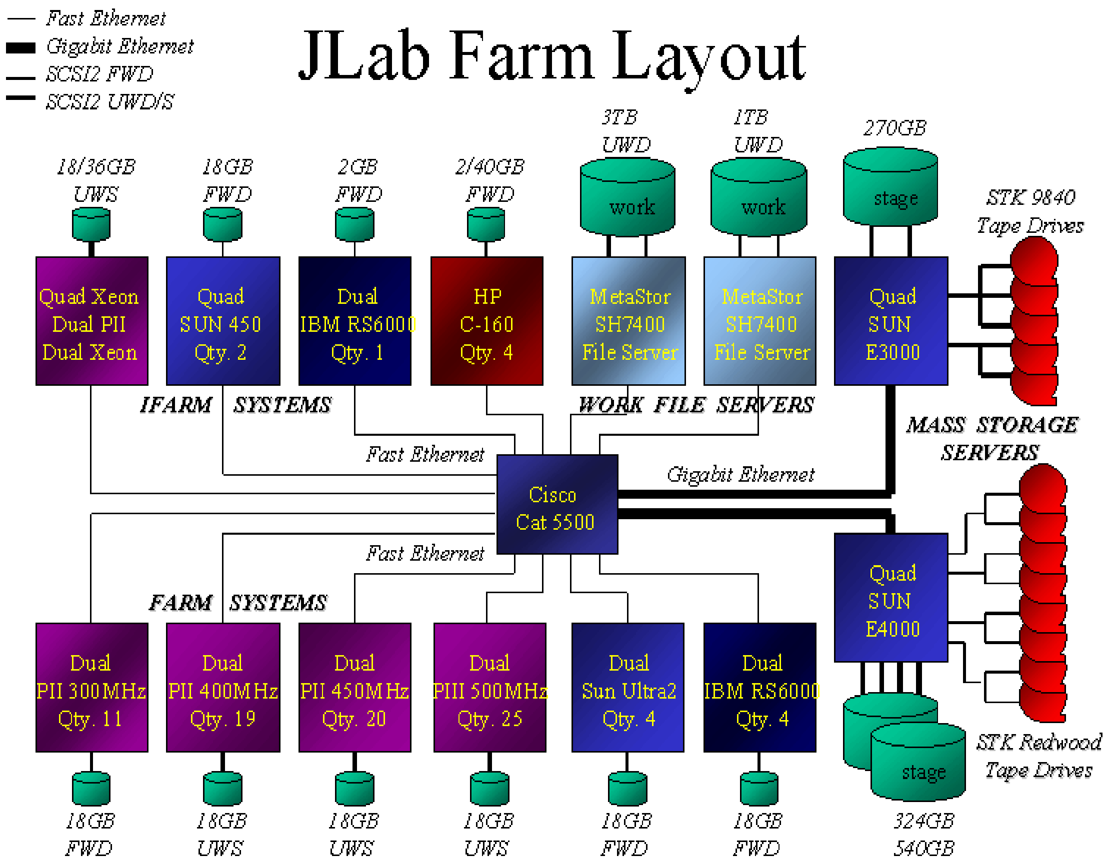

Figure 4.2. Schematic of the JLAB farm layout.

procedures that run the cooking process: submitting a request to the silo, submitting the cooking job to the farm, and copying the cooked files to the silo. The second type are the cooking executables which actually perform physics analysis, such as reconstructing tracks, monitoring the particle identification, and filtering out unwanted events.

4.4.2.1 Cooking Scripts

The JLAB farm is managed by the software package Load Share Facility (LSF). This package handles the prioritization of jobs, the job submission to the farm, and the allocation of resources to those jobs. LSF, however, does not provide any utilities to help a user keep track of a large number of submitted jobs. For this reason, a set of Perl scripts was written to control the whole cooking process and the user's interactions with LSF.

As mentioned before, large numbers of tape requests put a strain on the throughput of the JLAB tape silo system. As a result, it is desirable to minimize the number of requests made on the system. The first Perl script used in this process is *get_tape_info.pl*. This script queries the tape silo's MySQL database to find the tape volumes on which certain runs occur. In this way, the user can gather information about how to retrieve data from the silo in a way that minimizes the number of tape swaps. The output from *get_tape_info.pl* can then be used to directly make the requests from the tape silo for certain files. Once the files are retrieved from the silo and placed on the cache disk, the chef runs the next script in the cooking process, *Process_Run*. *Process_Run* runs the entire cooking process from the submission point of view. First, it calls the script *nextRun* which checks to make sure the run has not already been cooked. If it has not, *Process_Run* calls the script *makeSub* which creates a file that will be used by LSF to identify the resources necessary to run the job on the farm, such as which queue to use and which input file(s) LSF needs to copy to the farm node. These scripts are flexible enough to run any job on the batch farm.

For the cooking process, the script used on the farm was *RunJob*. Where *ProcessRun* handles the job at the submission end, *RunJob* manages the tasks that will be performed by the farm node. This script is simply a Perl wrapper around the physics processing executables which will be discussed in the next section. This being said, *RunJob* performs two important tasks with the output of these jobs. First, if the job produces any text messages, *RunJob* uses the capabilities of Perl as a parsing language to retrieve useful information about the physics results and stores that information in the off-line database. Secondly, *RunJob* handles moving the job's output files to their final location, either on the work disk or the tape silo. A schematic of *RunJob*'s functions are presented in Fig. 4.3.

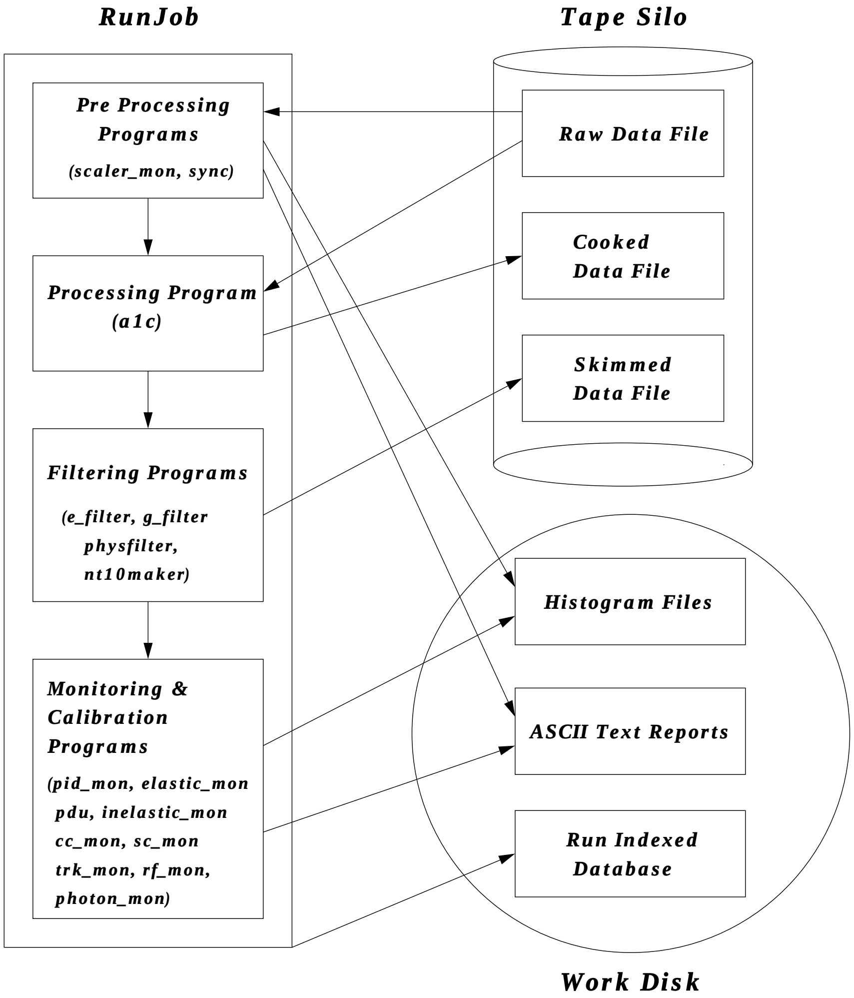

Figure 4.3. Schematic for the Perl script *RunJob* and how it interacts with the work disk and the tape silo [35].

4.4.2.2 Processing Executables

The first type of executable run on the data file is called a pre-processing executable. These programs do not require the data to be reconstructed but instead run on the raw data file. An example of this type of program is *sync*, which searches for bad synchronization events and creates a text file delineating the event numbers between which the bad synchronization event occurred. A synchronization event occurs after every thousand data events. The synchronization events are special triggers that check whether any crate controllers have received too many or too few gates. The processing executable then uses this information to drop those events from the subsequent cooked data file since it would be counterproductive to spend time on events in which event fragments are mixed.

The second type of program that runs on the raw data files is called a processing executable. For the E1 experiment the only processing executable was *a1c*. This program queries the Mapmanager database for the calibration values of each individual system, serves as an engine for the individual detector reconstruction software packages and creates a number of reconstructed BOS banks for each system. Combining the information from these banks to identify particles and constructing momentum four-vectors for those particles is then the job of *a1c*. This information is then stored in the cooked data file.

The next type of executables run on the cooked data files are the monitoring and calibration programs. The output format from these programs is a histogram file, an ASCII file, or both. These files are used to assess the quality of the data or to calibrate certain parts of the detector. The following is a list of the monitoring and calibration programs run on the E1 data set as well as a description of each executable's purpose:

- *cc_mon* looks at the calibration constants for the CC.
- *sc_mon* looks at the occupancy of the various SC paddles and performs rudimentary TOF efficiency calculations.
- *pdu* looks at the number of dead and hot wires in the DC.
- *rf_mon* calculates the corrections that must be made to the rf time to calculate particle masses accurately.
- *trk_mon* looks at the efficiency of the tracking code.

- *pid_mon* looks at the yields and characteristics for various particle types.
- *elastic_mon* looks at the yields for elastic events.
- *inelastic_mon* looks at the yields for a number of inelastic physics channels.

These executable are extremely useful in monitoring the health of the experiment over time. Using the results from *pid_mon* stored in the off-line database, for example, make it easy to examine the target stability during the 4.2 GeV 60% run period by examining the number of deuterons as shown in Fig. 4.4.

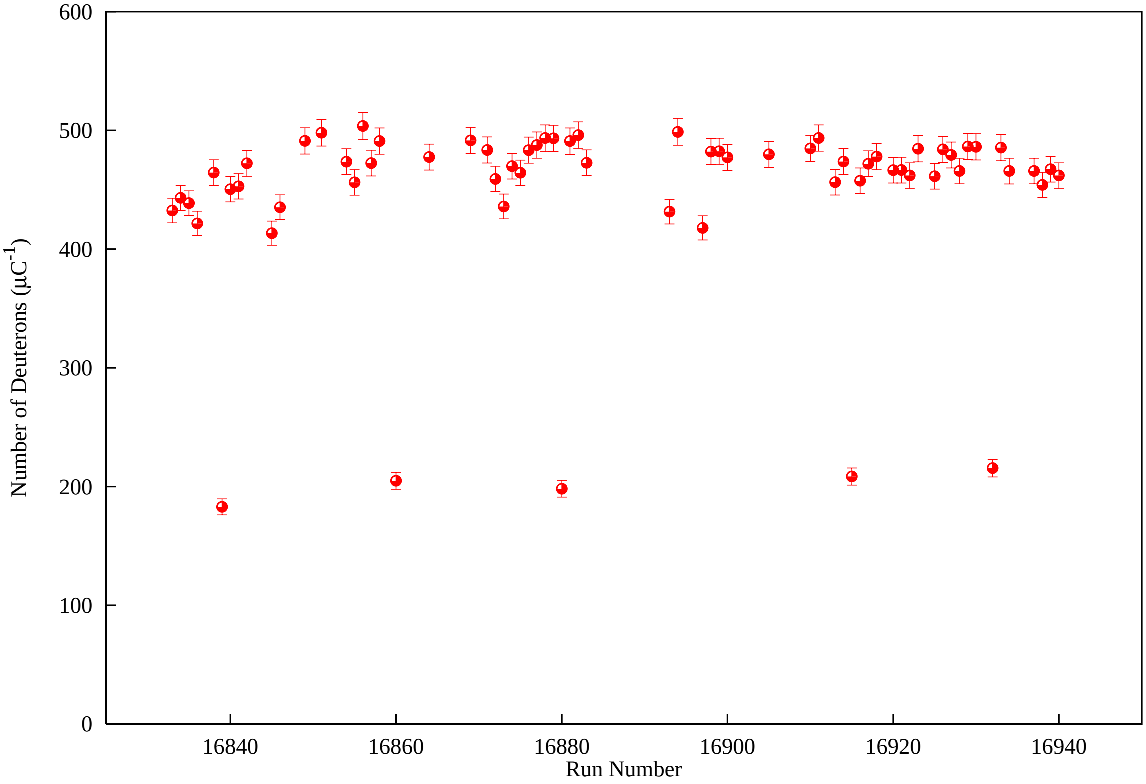

Figure 4.4. Number of deuterons normalized to the Faraday cup for runs taken during the 4.2 GeV 60% portion of E1C.

The last type of executable is the filtering program. These executables skim through the cooked data file to extract certain physics event topologies based on rudimentary particle identification. These skimmed files are quite useful since they allow users to store all of their data files on a simple SCSI disk attached to their local machine. This is especially useful since it limits the strain on the tape silo throughput. The following is a list of the filtering programs run on the E1C data:

- *e_filter* filters out hyperon candidates by keeping events which had a W value greater than 1.6 GeV/c^2 and a hadron whose mass squared was between 0.09 GeV^2/c^4 and 0.49 GeV^2/c^4
- *KK_filter* filters out $\Lambda(1520)$ and $\phi(1020)$ candidates.
- *physfilter* was used in a variety of ways to filter high multiplicity events. One example that was used was a filter for events which had two positive and two negative tracks.
- *nt10maker* was used to read in the BOS file and convert the data to ntuple format.

4.5 Data Reduction

The Hall B data acquisition system creates raw data files that are 2 GB in size. The reconstruction banks created in the cooking process, however, typically increase the size of each event by 150%. This gain is offset, though, by a requirement used by *a1c* that each cooked event contains at least one negative track. For the 4 GeV electron beam energy data, for example, this reduces the cooked file size to about 1.7 GB. Since on average there are 13 data files for each of the 343 runs used in this $\Lambda(1116)$ analysis this leads to 7.580 TB of data.

In order to make the data analysis manageable, the size of the files must therefore be reduced. The first reduction employed is the use of the filtered files created by *e_filter* during the cooking. Although the typical file size for these files in only 31 MB that would still result in 138 GB of data. The next procedure to reduce the data size involves using the program called *bankfilter*. This program gives the user the ability to remove a user specified list of BOS banks from the data file. A discussion among the E1 collaborators working on hyperon production produced a list of BOS banks which were extraneous to the analysis of the hyperon data and could be removed. Once these BOS banks were removed from the data file, the typical file size became 13 MB. Although this is a substantial reduction from the initial 1.7 GB total for this analysis the file size can be reduced further.

The last data reduction step performed on this data was another filter program. Since the important events for this analysis are ones which contain an electron, kaon, and a proton, it was unnecessary to keep events which did not contain at least these three particles. The data was therefore processed with an electron, kaon, proton filter which reduced the standard data file size to approximately 2.5 MB. At this point, all of the data fits comfortably on an inexpensive 18 GB SCSI disk mounted on a desktop Linux box.

An analysis of the data before and after reduction proved that no good $\Lambda(1116)$ decay events were lost in the process. Table 4.1 illustrates, as an example, the size of one data file from run 17233, which was taken during the 4.0 GeV 60% data set, as each of the data reduction methods were employed.

Table 4.1. File sizes for data file 17233.A05 throughout the data reduction steps.

Reduction Method Employed	File Size (in Bytes)
Raw Data File	2146402440
Cooked Data File	1728378000
e_filter File	31194000
DC0 Bank dropped	24285600
HEVT, EVNT, ECPB, DCPB, SCPB, LCPB, CCPB Banks Dropped	20732400
DSPC, FBPM, L2H, L2S, ELSR Banks Dropped	18644400
HBTR, HBER, HDPL, TRKS Banks Dropped	16038000
DHCL, DSTC, DSPS, ECS, RCST, S1ST, SCS, STS, TGS Banks Dropped	13089600
Electron, Proton, Kaon Filter	2422800

CHAPTER 5

ANALYSIS

5.1 Overview

Section 1.2.3 discusses the theoretical definition of the cross section for $\Lambda(1116)$ electroproduction. To determine this cross section experimentally the following relationship is used:

$$\frac{d^4\sigma}{dW dQ^2 d\Omega^*_{cm}} = \frac{N}{\mathcal{L} \cdot \Delta}, \tag{5.1}$$

where N is the number of events detected in a particular kinematic range and $\mathcal{L}$ is the integrated luminosity, or the product of the number of particles in the beam and the number of particles in the target. Δ is defined as the volume of the kinematic range or

$$\Delta = \Delta W \Delta Q^2 \Delta\Omega^*_{cm}. \tag{5.2}$$

However, not all of the events which occur inside the liquid hydrogen target are recorded. Therefore, the right hand side of Eq. 5.1 must be divided on an event by event basis by a correction factor, $\mathcal{C}$, to account for the events that are not reconstructed.

This correction factor can be written as

$$\mathcal{C} = \frac{\mathcal{T}}{\mathcal{A} \cdot \mathcal{R}}. \tag{5.3}$$

For the reaction analyzed in this thesis, $\mathcal{A}$, the acceptance correction, is the most important factor in Eq. 5.3. As will be discussed in the second section of this chapter, this correction is mainly due to events containing tracks whose trajectories traverse regions in which CLAS has no coverage or poor detection efficiency. Lesser effects also contributing to this factor, and discussed in this section, are the detector's resolution, unstable particles that decay in flight, the trigger efficiency, and the efficiency of the reconstruction software. The second most important factor to the overall correction, radiative effects denoted by $\mathcal{R}$, discussed in the third section of this chapter, is due to events in which the charged particles emit either a real or virtual photon causing the event to fail reconstruction or to be reconstructed in a different area of kinematics. The last factor, $\mathcal{T}$, the empty target correction factor, which is discussed in the fourth section of this chapter, is due to events which originated from the walls of the hydrogen target and not the liquid hydrogen itself. Additional correction factors, as well as a summary of the systematic errors present in this measurement, are discussed in the last section of this chapter.

5.2 Acceptance

Acceptance is typically defined to be a fractional value in the range of 0-1, for an event generated in a particular kinematic range, or bin, to be reconstructed in that same bin. For example, if 50 events are generated in a particular bin but only 5 of those events are reconstructed by CLAS, the acceptance for that bin is 10%. Therefore, the number of events measured by CLAS in that particular n-dimensional bin must be divided by 0.1 to correct for the unrecorded events. The number of dimensions needed for an accurate acceptance function depends on the number of degrees of freedom in the reaction.

Despite only detecting three of the four particles in the final state of the reaction

$$e + p \rightarrow e' + K^+ + (\Lambda(1116) \rightarrow p + \pi^-), \tag{5.4}$$

the acceptance function for this reaction depends on the degrees of freedom of all four final state particles. Since the masses are fixed for all outgoing particles, each reconstructed track has three degrees of freedom, one for each momentum projection, leading to a total of twelve degrees of freedom. If eleven of the momentum projections are known, though, the last degree of freedom is also known through conservation of energy. Similarly, by using conservation of momentum along the x-, y-, and z-axes, three more degrees of freedom are eliminated, bringing the remaining total to eight degrees of freedom. Binning the acceptance function in terms of particle momentum projections though is not very useful. Instead, eight physics variables that are of greatest interest to this thesis, discussed in Sec. 1.2, which also describe the event completely, are used: the laboratory angle, ϕ_{lab}, of the scattered electron, the reconstructed mass of the $\Lambda(1116)$, Q^2, W, ϕ_{cm}, $\cos\theta_{cm}$, ϕ^p_{rf}, and $\cos\theta^p_{rf}$.

The degrees of freedom can be reduced further by making some assumptions. First, since the $\Lambda(1116)$ is a weakly decaying particle, the width of its mass peak is essentially zero. As a result, it is safe to assume that the acceptance does not vary across the mass peak. Secondly, since it is a laboratory quantity, it safe to average over the ϕ_{lab} angle of the scattered electron, leaving a total of six degrees of freedom.

Ideally, a continuous acceptance function using these six degrees of freedom would be used for this reaction. In reality, though, the limited computing power available to model this experiment forces the function to be discrete, breaking the acceptance function into six-dimensional kinematic ranges, or bins. The primary factor determining the size of these bins is the statistical error of the correction. This uncertainty should be no larger than the statistical uncertainty in the same bin for the real data. Attention must also be paid to the practicality of the bin size. For example, a six dimensional acceptance function in which each dimension has ten divisions would result in one million bins. If each of these bins were to possess a statistical uncertainty of 10%, with an average acceptance of 5%, it would be necessary to simulate a total of 2 billion events for each experimental setup. For the data used in this thesis, that would require the generation of at least 8 billion events. As is discussed in more detail in Sect. 5.2.1, this is no small task.

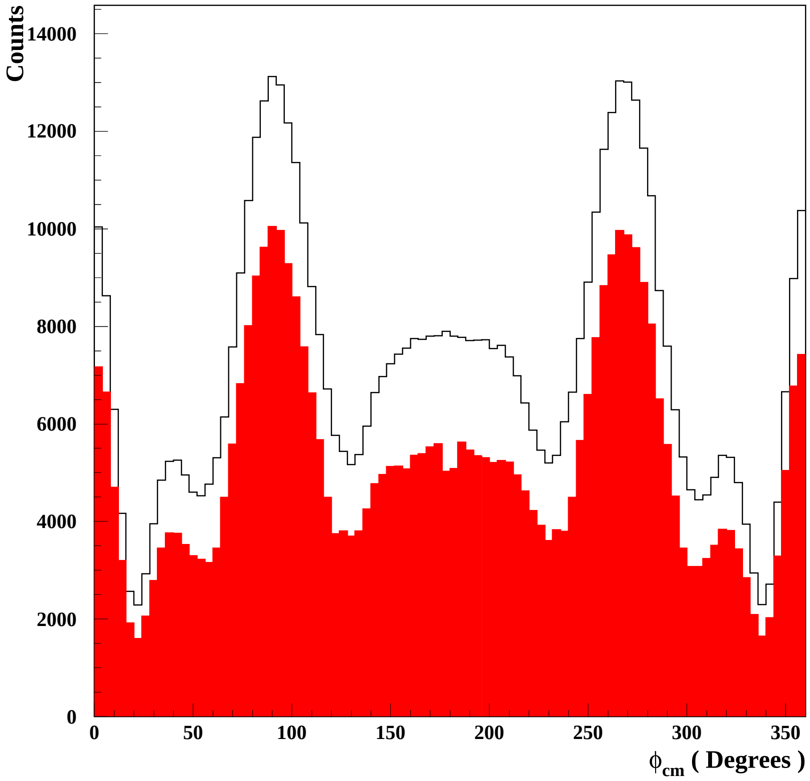

Figure 5.1. The unshaded histogram plots ϕ_{cm} for events generated for the 2.5 Gev 60% data set. The shaded area shows the same distribution for events in which the simulated event did not undergo bin migration. The statistics of this plot support a bin purity of 72%.

A second factor in the determination of the bin size is bin migration, in which an event generated in one bin is reconstructed in a different bin. One possible cause for this shift could simply be the resolution of the detector. Due to this bin migration, the acceptance correction factor is defined as

$$A = \frac{d^6 N^R(W, Q^2, \cos\Theta_{cm}, \Phi_{cm}, \cos\Theta_p, \Phi_p)}{d^6 N^T(W, Q^2, \cos\Theta_{cm}, \Phi_{cm}, \cos\Theta_p, \Phi_p)}, \tag{5.5}$$

where N^T refers to the number of events generated, or thrown, in a particular bin and N^R refers to the number of events reconstructed in that same bin. The widths of the bins for this analysis were chosen to minimize the sizes of the bins, while at the same time maximizing bin purity, defined as the fraction of events reconstructed in the same bin in which they were generated. For example, Fig. 5.1 plots ϕ_{cm} for the 2.5 GeV 60% simulation. The shaded area of the same figure shows ϕ_{cm} for events which did not migrate from one bin to another. Based on the ratio of these two plots, a bin purity of 72% for the final acceptance function used in this analysis is demonstrated.

The last factor in determining the binning of the acceptance function is through an examination of the variation of the acceptance over the range of a particular variable. For example, the acceptance is fairly smooth over the θ^p_{rf} and ϕ^p_{rf} variables, as will be shown later in this chapter. Therefore, fewer bins are necessary to accurately model the acceptance for these two variables. On the other hand, the acceptance across the ϕ_{cm} variable changes drastically at some points. For this reason, it is preferable to increase the number of bins used to model the acceptance against this variable. These considerations, and the ones mentioned in the two previous chapters, played an essential role in the final decision for the number of bins, detailed in Table 5.1, used for each variable in this analysis.

5.2.1 Implementation

To create an acceptance function for this reaction, events are generated using a model, described in Sec. 5.2.1.1, for the $\Lambda(1116)$ electroproduction. These events are binned in an ASCII table according to the dimensions in Table 5.1. The same events are then used as the input for a Monte Carlo simulation of the CLAS detector,

Table 5.1. Acceptance variable ranges and bins quantities.

Variable	Minimum Value	Maximum Value	Number of Bins
Q^2 for $E_{beam} > 4$ GeV	0.9 GeV^2	3.5 GeV^2	10
Q^2 for $E_{beam} = 2.5$ GeV	0.52 GeV^2	1.35 GeV^2	3
W for $E_{beam} > 4$ GeV	1.61 GeV	2.65 GeV	5
W for $E_{beam} = 2.5$ GeV	1.61 GeV	2.15 GeV	2
Φ_{cm}	0	360	10
$\cos\Theta_{cm}$	-1.0	1.0	8
ϕ^p_{rf}	0	360	5
$\cos\theta^p_{rf}$	-1.0	1.0	5

described in Sec. 5.2.1.2. Detector effects not implemented in this simulation are implemented by a post processor, as will be detailed in Sec. 5.2.1.3. The data are then cooked using *a1c*, the same executable used to reconstruct the real data. The event filtering and bank filtering mentioned in Sec. 4.5 are performed on the data set. Finally, the simulated data is analyzed using the same code, *lam_ana*, used to analyze the real data, and these events are binned in another ASCII table. The two ASCII tables are then combined, as shown in Fig. 5.2, to calculate an acceptance lookup table. In the analysis, the real data are scaled on an event by event basis using this lookup table.

The computing for this project is carried out on a cluster of 21 dual processor 350 MHz and 500 MHz pentium machines running RedHat Linux 5.1. Batch scripts performing all of the operations mentioned in the previous paragraph are submitted to this farm using the Distributed Queuing System (DQS) developed at Florida State University [41]. Each job processed by the DQS script has a limit of 50, 000 generated events. Each job takes, on average, one day to process fully, with approximately 16 hours of that time used during *gsim* processing. Running at the maximum capacity of the farm, this should lead to 2.1 M events being processed a day. Due to periodic maintenance periods and occasional unavailability of farm nodes, the actual production level is closer to 1.5 million events a day. Still, a total

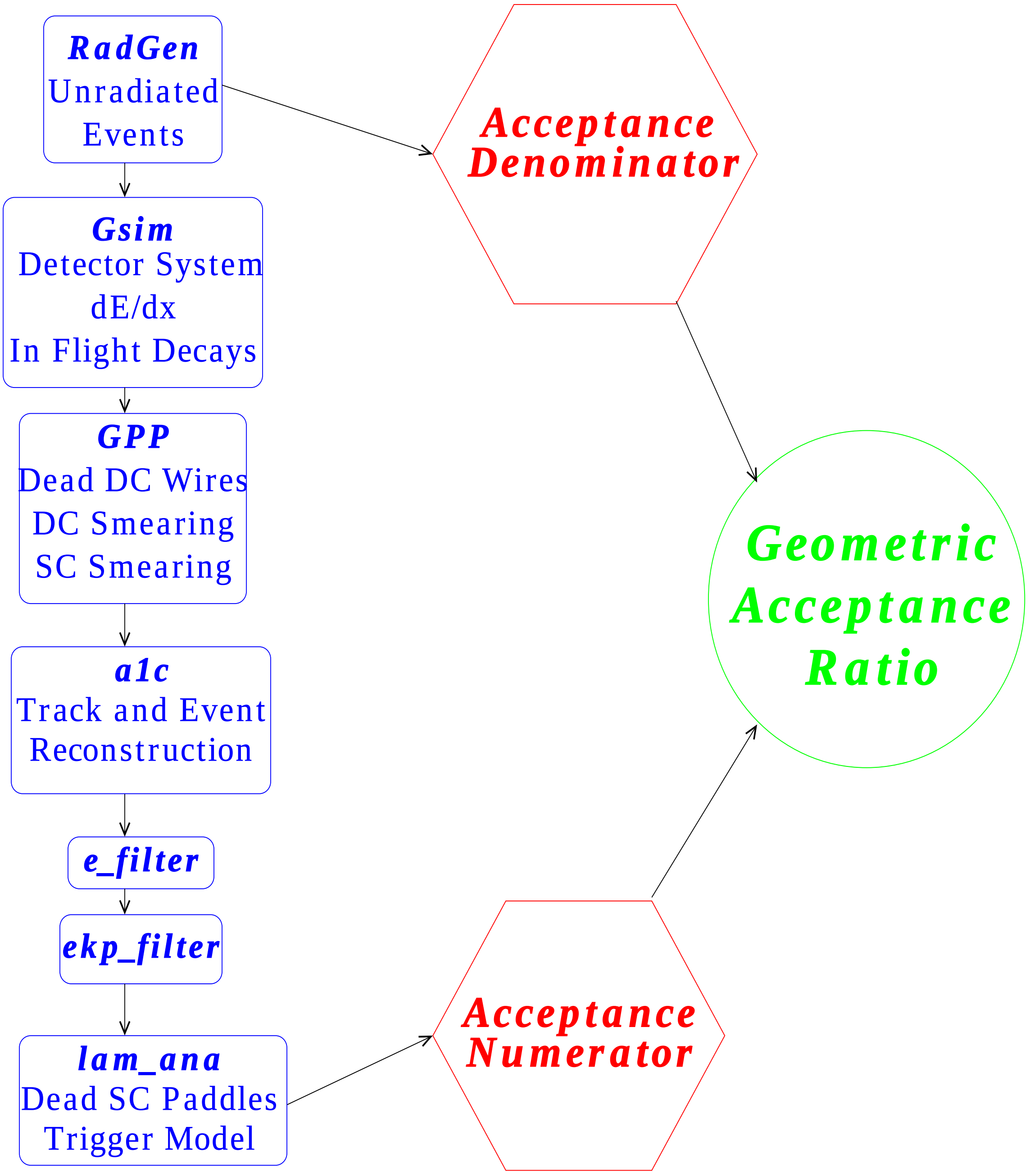

Figure 5.2. Flowchart describing the process by which a geometric acceptance lookup table is derived.

of 128 million events, representing four months of farm usage, were generated for the acceptance used in this thesis.

5.2.1.1 Event Generator

The event generator, *RadGen*, is based on the isobaric models of R. Williams, C.-R. Ji, and S. Cotanch [5] [42] and was converted into the C programing language by P. Geye [43]. The code was then modified by T. Mart who updated the values of the hadronic form factors employed by the model [44].

In the formalism specified in this code, the differential electroproduction cross section is expressed as

$$d\sigma = \frac{(2\pi)^{-5} M_p M_\Lambda M_e^2}{2[(e_1 \cdot p)^2 - M_e^2 M_p^2]^{\frac{1}{2}}} < |t_{fi}^2| > \delta(e_1 + p - e_2 - k - l) \frac{d\mathbf{e}_2 d\mathbf{k} d\mathbf{l}}{E_{e'} E_k E_\Lambda}, \tag{5.6}$$

where $< |t_{fi}|^2 >$ is the spin averaged, squared transition matrix. Integrating over the hyperon momentum gives

$$\sigma^3 \equiv \frac{d^3\sigma}{d\Omega_{e'} dE_{e'} d\Omega_k} = \frac{(2\pi)^{-5} M_p M_\Lambda M_e^2 |\mathbf{k}|^2 E_{e'}}{2[(e_1 \cdot p)^2 - M_e^2 M_p^2]^{\frac{1}{2}} E_k E_\Lambda R} < |t_{fi}|^2 > \tag{5.7}$$

where

$$R = \frac{\mathbf{k}}{|\mathbf{k}|} \cdot \left(\frac{\mathbf{k}}{E_k} - \frac{\mathbf{l}}{E_\Lambda} \right). \tag{5.8}$$

The transition matrix can be written out as

$$< |t_{fi}|^2 > = \left(\frac{\pi\alpha}{8 M_\Lambda M_p M_e^2} \right) \left(\frac{1}{q^2} \right) \sum_{i,j=1}^{6} B_i B_j^* [\overline{T}_1^{ij} + \overline{T}_2^{ij}] \tag{5.9}$$

where α is the electromagnetic fine structure constant,

$$\overline{T}_1^{ij} = \mathbf{Tr}[(\not{l} + M_\Lambda) \mathcal{N}_\mu^i (\not{p} + M_p) \mathcal{N}_\nu^{j\dagger} g^{\mu\nu}], \tag{5.10}$$

and

$$\overline{T}_2^{ij} = \left(\frac{4}{q^2}\right) \mathbf{Tr}[(\not{l} + M_\Lambda)(\mathcal{N}^i \cdot e_1)(\not{p} + Mp)(\mathcal{N}^{j\dagger} \cdot e_1)]. \tag{5.11}$$

The $B_{i,j}$ included in Eq. 5.9 are the summed amplitudes from the included Feynman diagrams, which can be found in Table 1.1, such that

$$\begin{aligned} B_j(q^2,s,t,u) &= B_j^{Born}(q^2,s,t,u) + \sum_{N^*} B_j^{N^*}(q^2,s,t,u) + \sum_{Y^*} B_j^{Y^*}(q^2,s,t,u) \\ &+ \sum_{K^*} B_j^{K^*}(q^2,s,t,u) \end{aligned} \tag{5.12}$$

where the last set of terms is included as a duality correction.

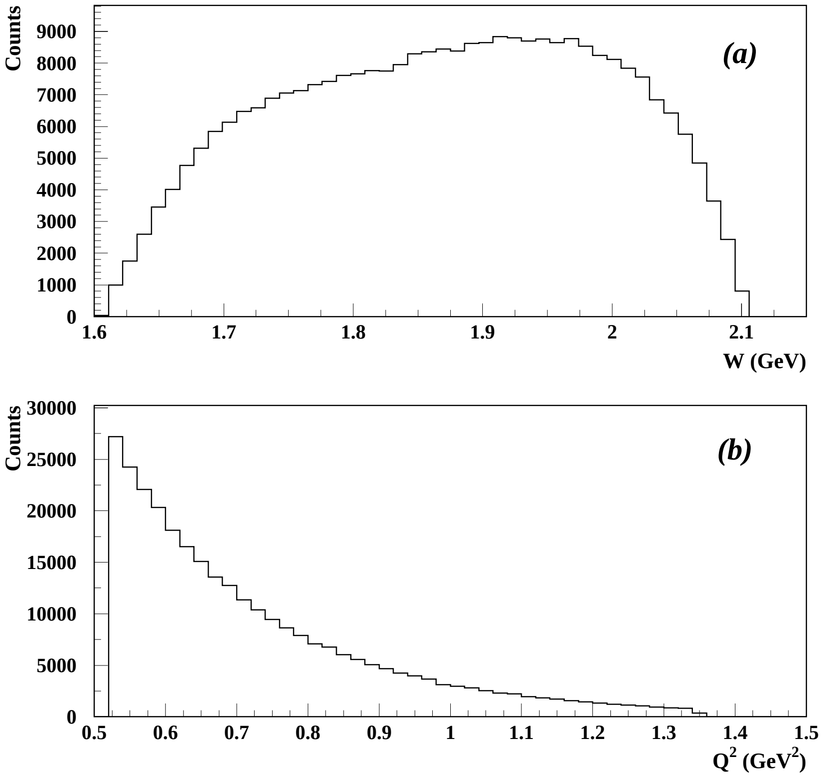

Figure 5.3. Electron kinematic variables (a) Q^2 and (b) W distributions generated using *RadGen* for $E_{Beam} = 2.5$ GeV.

Without radiative effects, for $E_{Beam} = 2.5$ GeV data, *RadGen*, using the above formalism, produces the distributions for the kinematics of the electron shown in

Fig. 5.3. Although the generated W distribution is not peaked at low values as expected, the Q^2 distribution shows the expected exponential decay. The angular distributions for the four other acceptance table variables, shown in Fig. 5.4, also reproduce the expected distributions including the forward peaking in $\cos\theta_{cm}^{K+}$.

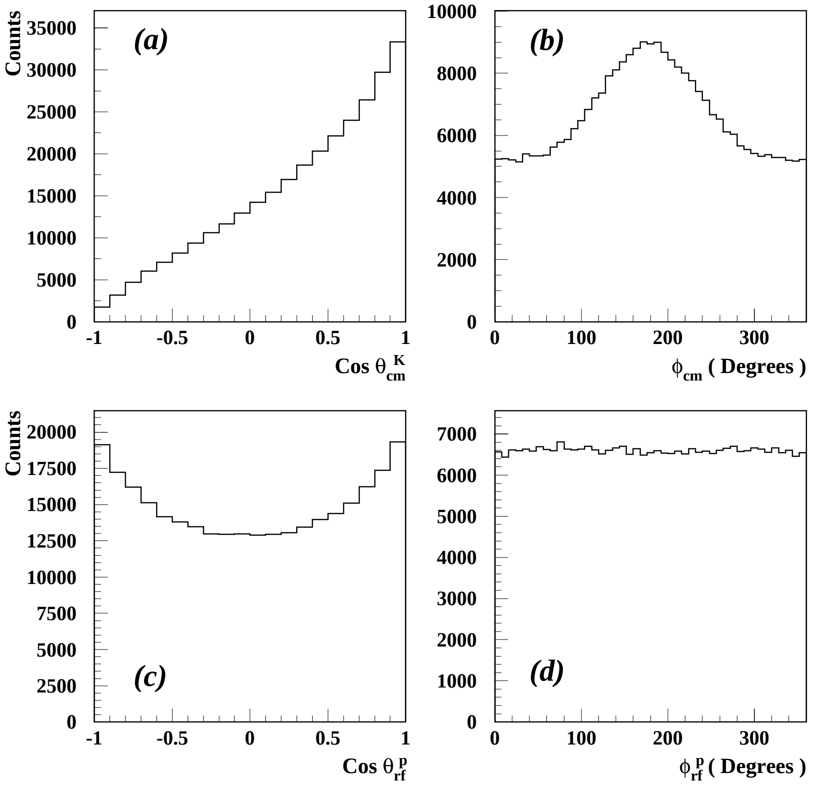

Figure 5.4. Angular distributions (a) $\cos\theta_{cm}^{K+}$, (b) ϕ_{cm}, (c) $\cos\theta_{rf}^{p}$, and (d) ϕ_{rf}^{p} generated using *RadGen* for E_{Beam} = 2.5 GeV data.

For this analysis, the generated events were only limited by the ranges of Q^2 and W and the physical limits these constraints created. In the analysis of some reactions, generated events were limited to fiducial regions of CLAS. A previous study of Λ(1520) electroproduction at CLAS [46], though, has shown that particles thrown in the direction of the CLAS torus can still be reconstructed within a CLAS fiducial region. Many of these events also passed all of the event identification cuts, including missing mass cuts. As a result events generated to simulate the acceptance for this analysis were not limited to fiducial regions of CLAS. Instead, events were allowed to populate the full 4π laboratory angular range.

5.2.1.2 GSIM

Geant is a software toolkit created at CERN to simulate nuclear physics experiments. In Geant, the user models an experimental setup through the use of geometrical volumes filled with materials of various densities. Geant also handles the transport of particles through the various regions while taking into account boundary effects as well as the interactions of the particles with matter and magnetic fields. The particle trajectories as well as the response of the detector elements are then recorded.

The Geant based simulation of the CLAS spectrometer, known as GSIM, through which the generated events are passed, contains a digitization of the material associated with the torus and mini-torus, as well as the CLAS support structures. The materials for the target cell specific to the E1C run period are also included. More importantly though, GSIM models the DC, EC, SC, and CC components of CLAS. The positions of each detector in the model match the specific location and orientation of the detector during the E1C run period conditions. The geometrical volumes of both the DC and CC systems contain the appropriate gas mixtures associated with each detector. However, the material associated with the individual DC wires is not explicitly implemented in this simulation. The intricate modeling of the full CLAS system, though, lets most dE/dx effects, particle showering, and multiple scattering to be automatically folded into GSIM. Figure 5.5 shows, for example, the detail involved in GSIM for an electron shower in the EC.

In addition to particles created through showers and multiple scattering, GSIM handles the in-flight decays of particles according to the mean lifetimes of the particles and decay channels specified in Ref. [22]. In this way, the in-flight decay of the K^+ and the $\Lambda(1116)$ are automatically folded into the acceptance. However, since the $p\pi^-$

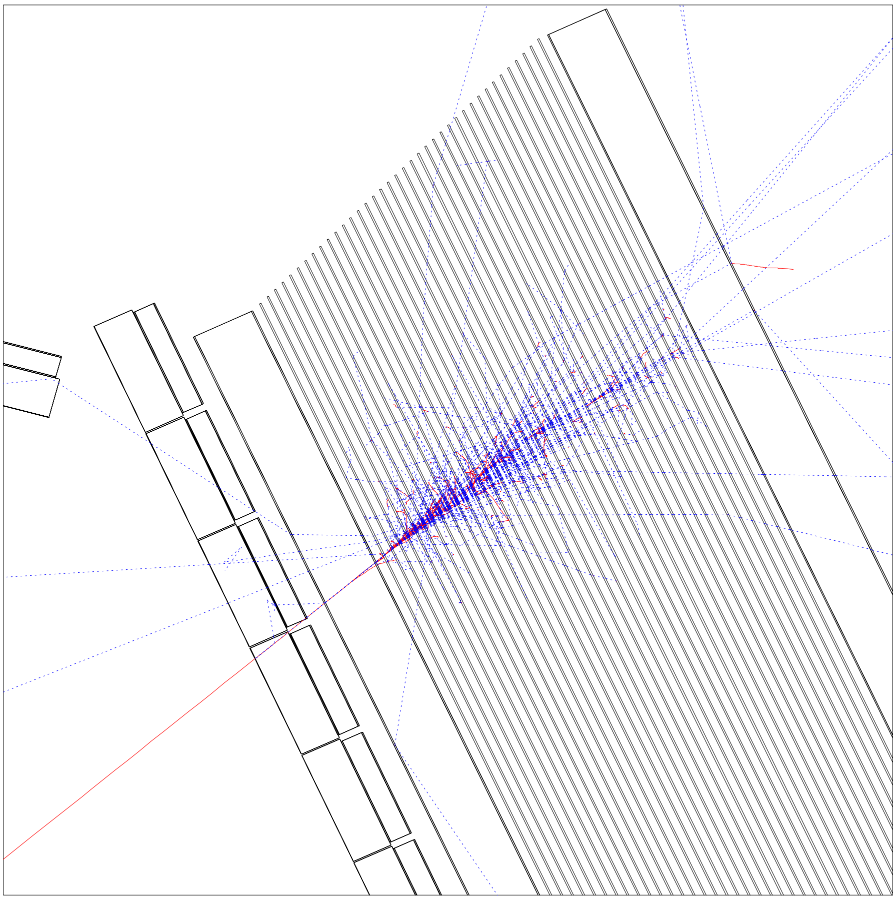

Figure 5.5. A GEANT simulation of the EC response to a 2.4 GeV electron entering the calorimeter from the bottom left of the figure. The dotted lines denote photons emerging from the shower. The individual TOF bars, backing structures, and EC lead sheets are shown [31].

decay mode of the $\Lambda(1116)$ has the largest branching ratio and largest acceptance for detection in CLAS, the GSIM libraries were modified to force the $\Lambda(1116)$ to decay through only this channel to reduce the CPU time necessary to generate the acceptance table.

5.2.1.3 GSIM Post Processor

Although the material associated with each wire in the DC is not explicitly implemented in GSIM, the geometry map file associated with those wires allows

GSIM to map a particular track to a corresponding set of DC wires. Between run periods, and even during run periods, though, the health of the DC fluctuates as some wires malfunction and others are repaired. As mentioned in Sec. 4.4.2.2, during E1C cooking, the post processing program, *pdu* was run on each of the data files to determine which DC wires were malfunctioning. At the completion of E1C cooking, the number of dead wires was plotted versus run number for each DC region. A run was then chosen from each beam energy and torus combination indicative of the DC health for that particular run condition. The status of each DC wire during this run was added to the Mapmanager file *DC_STATUS.map*. The GSIM Post Processor (*GPP*), utilizing the *DC_STATUS.map*, was then used to remove dead wires particular to that data set from the GSIM file before cooking. In this way, gaps in the DC were accurately incorporated in to the simulated acceptance of CLAS.

When GSIM calculates which DC wires to associate with a track, it records the exact position of the track. In reality, though, hardware and detector effects introduce resolution contributions which smear the position of the track. *GPP* has the capability to mimic these effects by smearing the recorded GSIM track positions on a region by region basis according to a Gaussian distribution. Using a sixth order polynomial [45], in addition to a user specified scaling value, *GPP* determines the width of that Gaussian distribution. The user specified scaling factor is determined through an examination of the $\Lambda(1116)$ missing mass resolution from one CLAS sector when various smearing factors are used. The factors used in this analysis are 1.5 for Region 1, 2.0 for Region 2, and 2.5 for Region 3.

A comparison of the simulated and actual $\Lambda(1116)$ resolutions are shown in Fig. 5.6 for the 4.2 GeV 60% data set. Figure 5.6(a) shows the electron-K^+ missing mass for GSIM events which also contain a reconstructed proton and a missing π^-. Figure 5.6(b) plots the same spectrum for actual data. Several factors contribute to the smaller resolution in the GSIM data. First, the real data peak has a contribution from background due to the residual $\Sigma(1193)$ peak. This background is not present

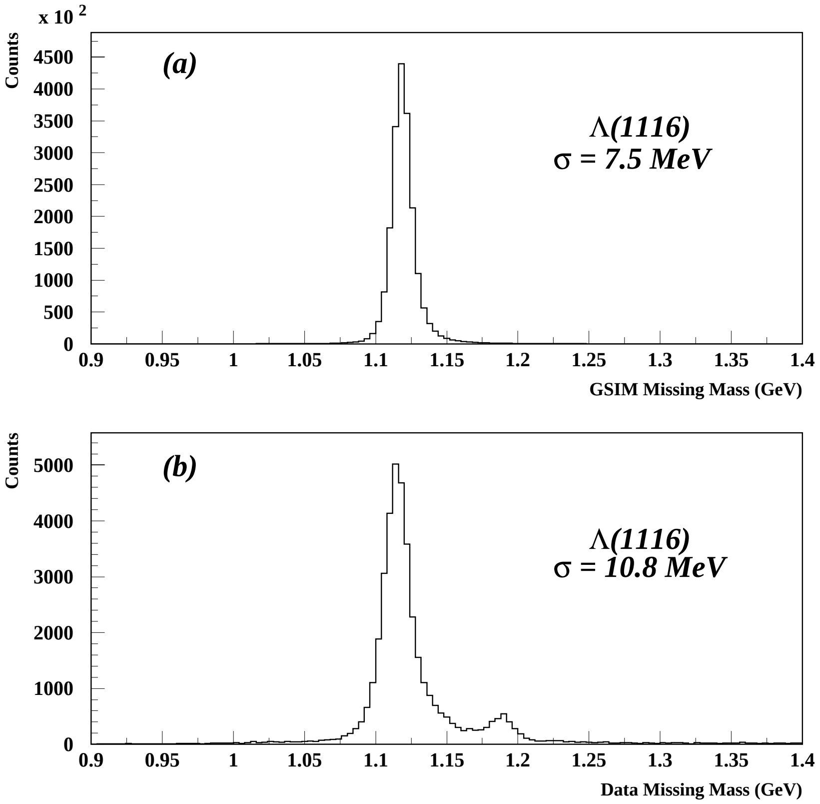

Figure 5.6. (a) Plots the electron-K^+ missing mass for GSIM events which also contain a reconstructed proton and a missing π^-. (b) The same spectrum for real data events. The differences between the resolutions are discussed in the text.

in the GSIM data since the $\Sigma(1193)$ was not simulated. The GSIM data also does not include radiative effects. Lastly, there might be slight detector misalignments from sector to sector which causes the $\Lambda(1116)$ centroid to shift slightly between sectors. Such an effect widens the overall $\Lambda(1116)$ width. However, artificially smearing the GSIM DC to compensate for these effects is not a proper method for dealing with these issues.

Similar to the DC, the GSIM SC banks record the exact TDC value for each recorded hit. The left and right TDC value for each SC, therefore, is smeared by *GPP* to mimic the actual resolution effects. Figure 5.7(a) plots the SC mass for reconstructed GSIM hadron tracks, while Fig. 5.7(b) plots the same spectrum for actual hadron tracks from the 2.5 GeV 40% data set. Once again the GSIM resolution is slightly better than the resolution found in the real data. For both the proton and K^+ peaks, this difference is mainly due to the sector misalignment. The resolution for the K^+ peak in the real data is also affected by a large π^+ background. This background does not exist in the GSIM plot since no events were generated containing energetic π^+ tracks. This fact also explains the lack of a peak in Fig. 5.7(a) at 0.140 GeV present in Fig. 5.7(b).

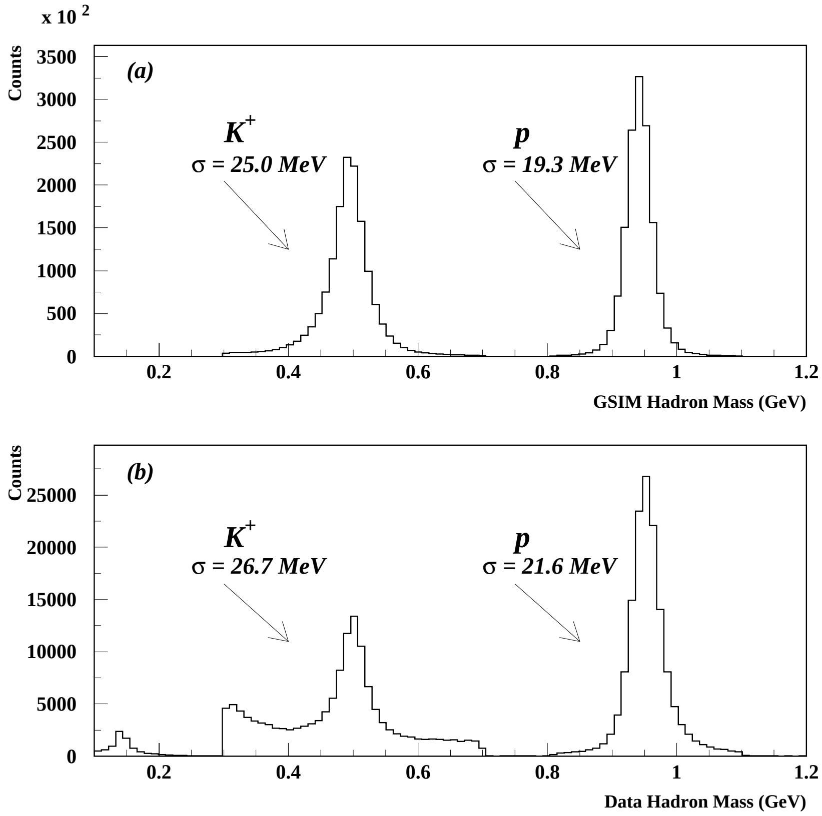

Figure 5.7. (a) Hadron masses reconstructed from the SC for GSIM data. (b) The same spectrum for real data events. The differences between the resolutions are discussed in the texts.

5.2.1.4 Reconstruction Inefficiencies

Not all analysis inefficiencies are related to the actual detector components. Another source of inefficiency is found in the software used to reconstruct the data. For example, large inefficiencies were found in the analyses of the reconstruction of both $\Lambda(1520)$ and $\phi(1020)$ events [46]- [48]. In these analyses, reconstruction inefficiencies occurred in events in which two tracks traversed the same sector of CLAS and eventually crossed within the boundaries of CLAS. Even similarly charged tracks sometimes exhibite this behavior. The estimated systematic error associated with these close track inefficiencies is $\sim 2\%$ [49].

In order to model this crossing track inefficiency as well as other hidden inefficiencies in the reconstruction software, the simulated data is reconstructed using the same *a1c* program used to reconstruct the real data. The detector geometry and magnetic field map used to reconstruct the simulated data are the same ones that are used to reconstruct the real data. The calibration values, though, used to reconstruct the simulated data are the simply the inverse of the values used to digitize the data.

After being processed by *a1c*, the size of the simulated data set is reduced by *e_filter*, *ekp_filter*, and *bank_filter*, the same programs used to reduce the real data. The final data set is also analyzed using the same program, *lam_ana*, which performs the final analysis on the real data.

5.2.1.5 Trigger Model

Due to the complex nature of CLAS, special attention must also be paid to the effects the trigger has on the acceptance for a particular reaction. Although GSIM contains a digitization of the EC and CC hardware, it does not accurately model the detailed performance of either detector. *GPP* does contain a trigger simulator which allows the user to select events in which a particle triggers an intrasector EC and CC coincidence. The threshold cut employed by *GPP*, though, is sharp, and does not accurately reflect the detector resolution at threshold. As a result, the trigger is taken into account in the *lam_ana* program as the overall acceptance is being calculated.

First, as discussed in Sec. 3.3.1, for a given EC hardware threshold, there should be a corresponding sharp cutoff in the recorded electron energies. Amplitude fluctuations in the EC response though are not sharp, leading to a distortion of the electron energy spectrum near threshold. This distortion leads to acceptance issues which are very difficult to model. As a result the same cut, applied to the real data, as found in Eq. 3.4, is also applied to the GSIM data. This cut raises the lower edge of the $\Lambda(1116)$ kinematic region well above the problematic region.

The inefficiencies of the CC are handled in a different manner. During E1C, special runs were taken in which the trigger included only the EC. From these runs a map of the efficiency of the CC was made from an examination of the mean number of photoelectrons recorded in the CC for elastically scattered electrons [51]. Figure 5.8 shows, as an example, the efficiency of the CC versus Q^2 for electrons in the 4.0 GeV 60% data. In the *lam_ana* program, the position and angle of the electron track is calculated relative to the CC plane. Based on this information, a value is retrieved from the CC efficiency map for the detector response. If this efficiency is less than a random number between 0-1, the event is recorded as failing reconstruction.

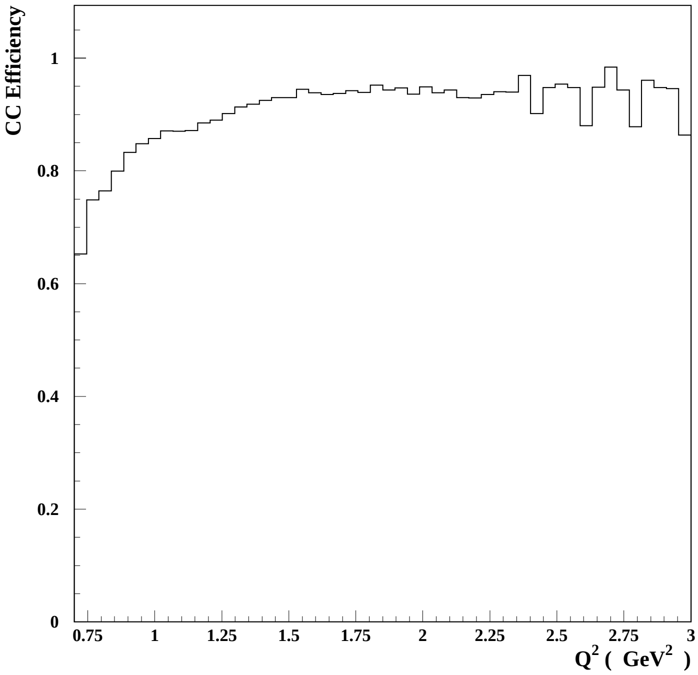

Figure 5.8. Efficiency of the CC versus Q^2 for all electrons for the 4.0 GeV 60% data. The large fluctuations for $Q^2 > 2.35\ GeV^2$ are due to low statistics.

5.2.2 Results of CLAS Acceptance Calculation

Figures 5.9-5.11 show the acceptance for the different data sets included in this analysis based on the procedure described in Sec. 5.2.1. In each of these plots the acceptance is averaged over the degrees of freedom not shown. For example, in Fig. 5.9(a) the acceptance is averaged over Q^2, ϕ_{cm} ,$\cos\theta_{cm}^{K+}$, ϕ_{rf}^{p}, and $\cos\theta_{rf}^{p}$.

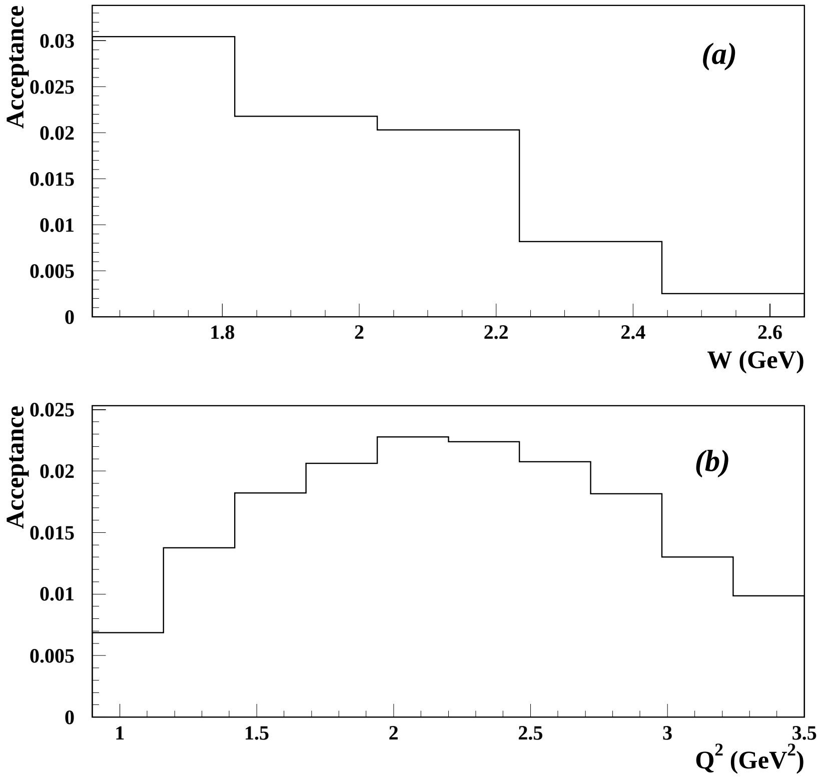

Figure 5.9. Acceptance for the 4.2 GeV 60% data set for the variables (a) W and (b) Q^2.

Figure 5.9 shows, for the 4.2 GeV 60% data, decreasing acceptance with increasing W and Q^2 as the electron approaches the boundaries of its kinematics. In Fig. 5.9(b) the smaller acceptance values at low Q^2, though, correspond to events being lost as the electron continues to follow the electron beam pipe where there is no CLAS detector element. Drawing similar conclusions from Figs. 5.10 and 5.11 is harder

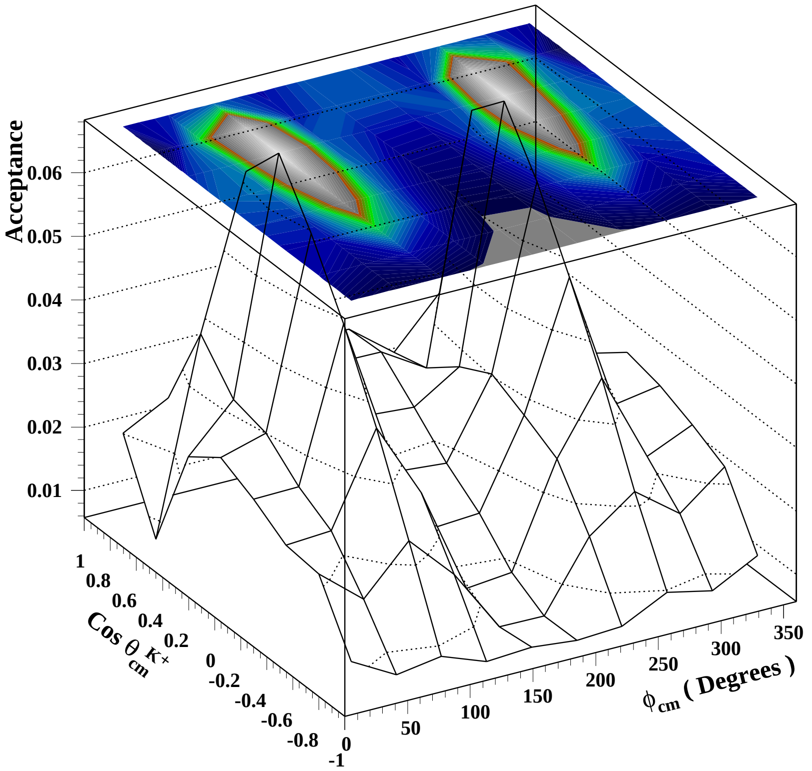

Figure 5.10. Acceptance characteristics for the center of mass angles for the 2.5 GeV 60% data set.

to accomplish due to the transformations back to the laboratory frame of reference and the correlations between the four final state particles. For polarization results , though, it is important to notice that the acceptance over the rest frame angles in Fig. 5.11 is relatively flat compared to the other binning variables.

For the data set used to calculate the polarization results, Fig. 5.12(a) shows the mean acceptance is $\sim$ 4.5%. Figure 5.12(b) shows that the mean number of thrown events in accessed bins of the acceptance function denominator is $\sim$ 800 events, resulting in an average statistical error in the acceptance function of $\sim$ 16%. To prevent anomalous events from dominating acceptance corrected yields, $\mathcal{A}$ is required to be greater than 0.008 and the number of events in the denominator of an accessed

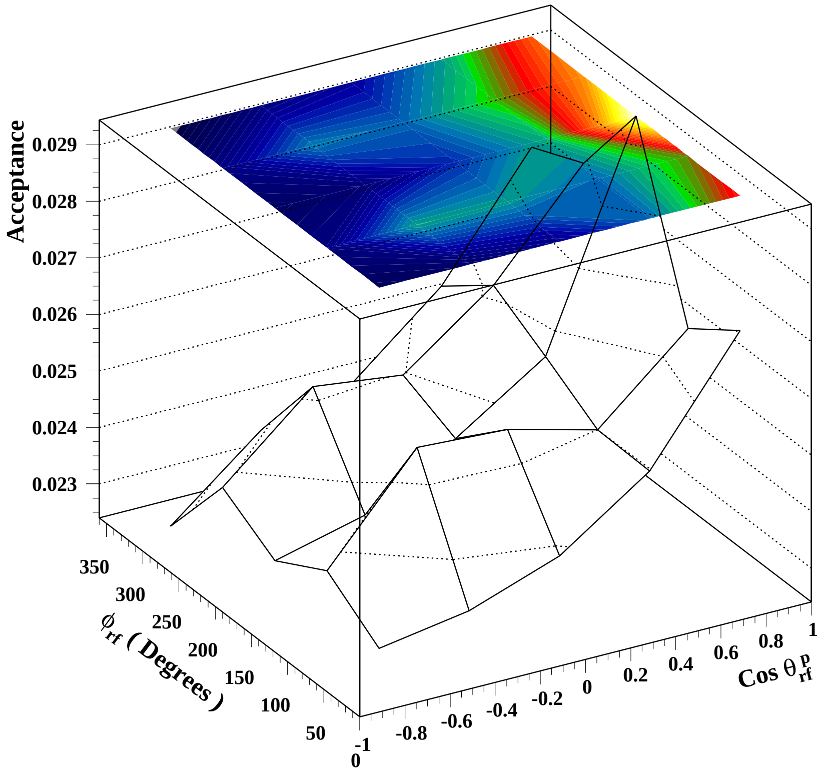

Figure 5.11. Acceptance characteristics for the $\Lambda(1116)$ rest frame angles for the 2.5 GeV 40% data set.

bin is required to be greater than 250. The combination of these two requirements produces a systematic error $\sim 5\%$.

5.3 Radiative Corrections

One disadvantage of electron scattering is the fact that photons, both real and virtual, are easily produced in electron scattering experiments. These photons can be created as internal radiation when the charged particles involved in the reaction are accelerated by the field of the nucleus involved in the primary hard scattering. The charged particles can also undergo external radiation by which they are accelerated by other nuclei in the surrounding materials.

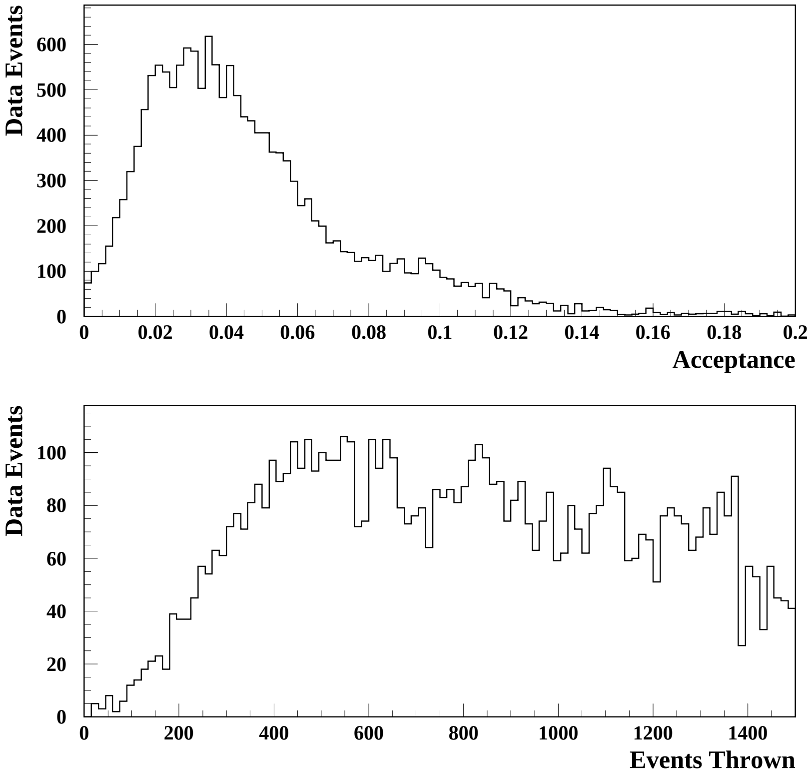

Figure 5.12. Frequency distributions of the (a) correction factor, $\mathcal{A}$, applied to the data presented in this thesis and (b) the number of events thrown into bins of the acceptance function denominator accessed by data presented in this thesis.

The emission of real photons, through these two processes, causes the detected momentum of the particle and the actual momentum at the scattering vertex to differ. This discrepancy causes a distortion in the extracted spectra. Amplitudes involving the emission of virtual photons, though, affect only the magnitude of the measured cross section. However, the data must still be corrected to account for these processes shown in Fig. 5.13.

In this analysis, the diagrams in Fig. 5.13 were included as part of *RadGen* using the formalism introduced by Ref. [50], which was converted to C code by R. Thompson [36]. This formalism makes two fairly safe assumptions. First, it is assumed that the photons are radiated in the direction of the particle from which

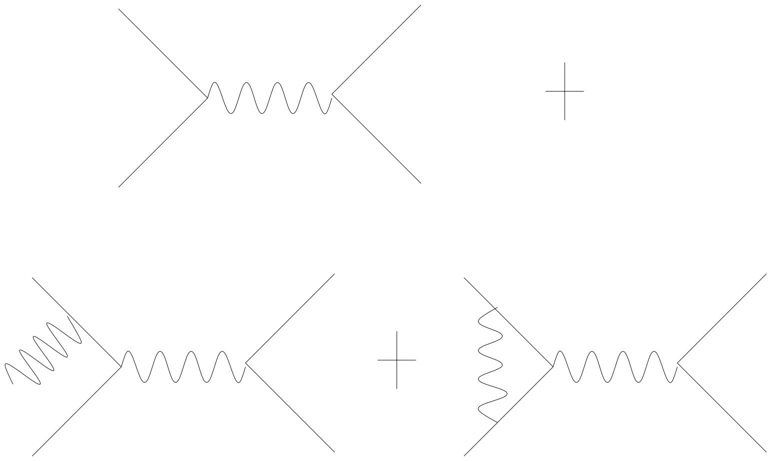

Figure 5.13. The first diagram is an example of the standard diagram contributing to the $\Lambda(1116)$ electroproduction model. The second diagram shows an example of a first-order external radiation process contributing to the radiative correction calculation, while the third diagram shows an example of a first-order internal radiation process.

they emitted. This is known as the peaking approximation. Secondly, in the soft photon approximation, the energy of the emitted photon, ω is assumed to be much less than the momenta of the initial and final state of the particle from which they radiated.

Due to the already small geometric acceptance discussed in Sec.5.2, radiative effects were not folded into the geometric acceptance. Instead, events undergoing radiation and events not undergoing radiation are generated using *RadGen.* The resolution of the electron-K^+ missing mass peak for both sets of events are then smeared according to a Gaussian distribution to match the resolution of GSIM as shown in Fig. 5.14. These events are binned according to variable dimensions specified in Table 5.2. The ratio between the two sets of events are then taken on a bin by bin basis according to

$$\mathcal{R} = \frac{N_{Radiated}}{N_{Unradiated}} \times \frac{\mathcal{L}_{Unradiated}}{\mathcal{L}_{Radiated}}. \tag{5.13}$$

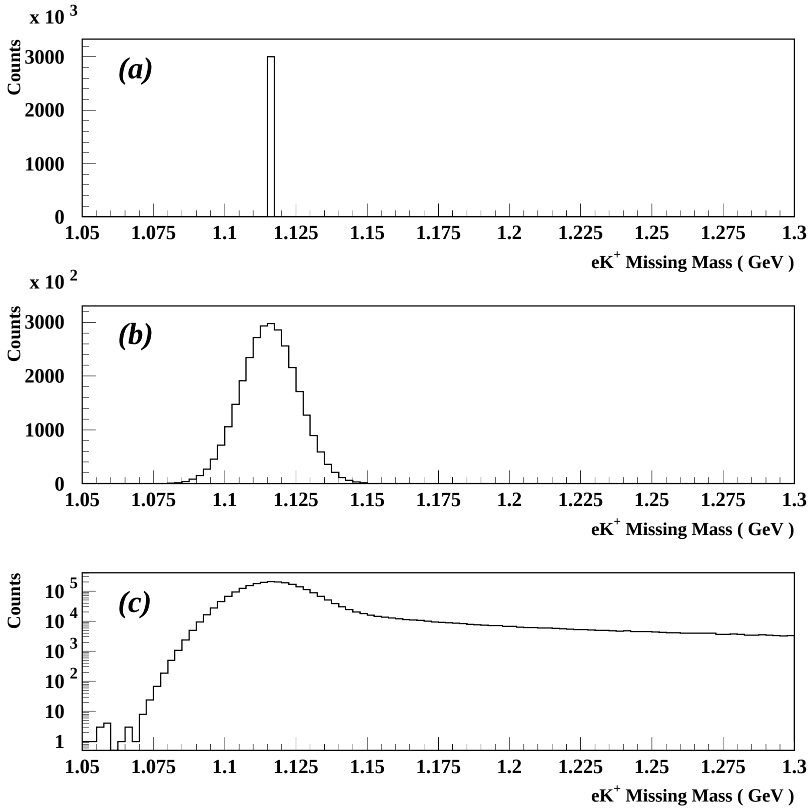

Figure 5.14. Electron-K^+ missing mass from the radiative correction program for the 4.0 GeV 60% data set. (a) Plots the unradiated missing mass, (b) plots the smeared unradiated missing mass, and (c) plots the smeared radiated missing mass on a log scale.

$N_{Radiated}$ and $N_{Unradiated}$ are the number of radiated and unradiated events in a particular bin and $\mathcal{L}_{Radiated}$ and $\mathcal{L}_{Unradiated}$ are the number of events thrown into each bin by *RadGen*. It is incorrect to assume that $\mathcal{L}_{Radiated}$ and $\mathcal{L}_{Unradiated}$ are equal for a particular bin, as is discussed in Ref. [36]. In the reaction examined in this thesis, such an assumption incorrectly produces a dramatic correlation between Q^2 and $\cos\theta_{cm}^{K^+}$. Figure 5.15 illustrates the radiative corrections determined through the proper technique for the 4.0 GeV data.

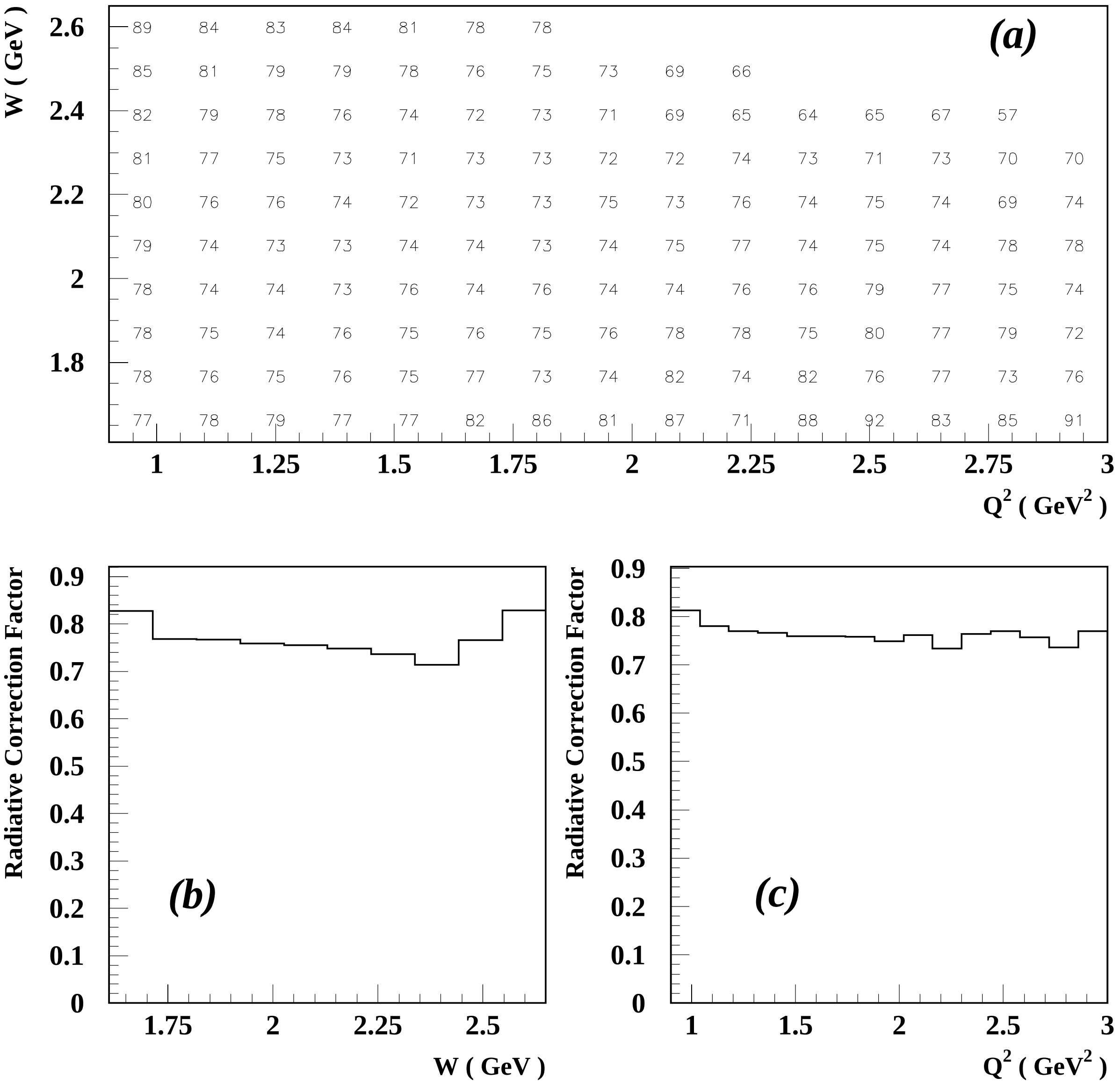

Figure 5.15. Radiative correction factors for the 4.0 GeV 60% data set. (a) shows the Q^2 versus W correction factor as a percentage. (b) and (c) show the correction factor projected as a function of W and Q^2, respectively.

Table 5.2. Radiative correction variable ranges and bins quantities.

Variable	Minimum Value	Maximum Value	Number of Bins
Q^2 for $E_{beam} > 4$ GeV	0.9 GeV^2	3.0 GeV^2	15
Q^2 for $E_{beam} = 2.5$ GeV	0.52 GeV^2	1.35 GeV^2	10
W for $E_{beam} > 4$ GeV	1.61 GeV	2.65 GeV	10
W for $E_{beam} = 2.5$ GeV	1.61 GeV	2.15 GeV	10
$\cos\Theta_{cm}$	-1.0	1.0	10

5.4 Empty Target Corrections

For a liquid hydrogen target housed in a target cell, it is impossible to avoid recording events which originate from the target wall instead of the hydrogen gas. Additional events could also originate from impurities within the liquid hydrogen. Although missing mass cuts eliminate a majority of these events, due to the Fermi motion of the proton in the nucleus, some events of this type do succeed in passing all event identification cuts. For this reason, a simple vertex cut is insufficient in eliminating these background events. An empty target correction factor therefore must be applied to the data to account for this effect.

During the E1A and E1B run periods an ice buildup on the walls of the target cell made the calculation of a correction factor even more difficult. Figure 5.16 though shows the number of deuterons normalized to the Faraday Cup versus the run number for the 4.2 GeV 60% data. The data points where the number of deuterons $\approx 200\mu C^{-1}$ correspond to runs taken with an empty target. The remaining production runs, though, show a relatively constant number of deuterons, indicating the lack of an ice buildup. The remaining data sets included in this analysis follow a similar trend.

Since the empty target correction factor remains constant throughout a run period, the method used to calculate this factor is fairly straightforward. First, the production runs and empty target runs are analyzed separately using the *lam_ana* code. $\mathcal{T}$ is then determined through the equation

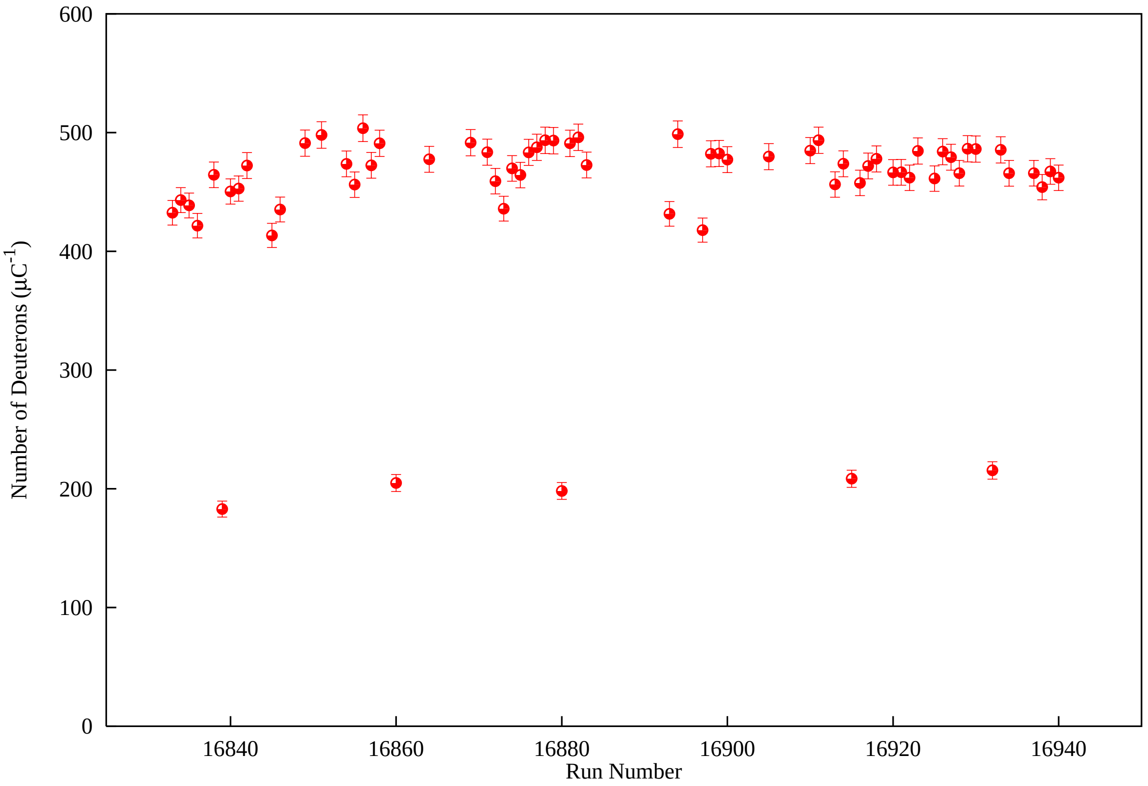

Figure 5.16. Number of deuterons normalized to the Faraday cup for runs taken during the 4.2 GeV 60% portion of E1C.

$$\mathcal{T} = 1 - \frac{N_{Empty}\mathcal{L}_{Production}}{N_{Production}\mathcal{L}_{Empty}} \tag{5.14}$$

where N_{Empty} and $N_{Production}$ are the number of $\Lambda(1116)$ events recorded by *lam_ana* for the empty target and production target runs, respectively. $\mathcal{L}_{Production}$ and $\mathcal{L}_{Empty}$ refer to the livetime gated Faraday Cup luminosities of the respective target configurations. The resulting $\mathcal{T}$ factors for this analysis can be found in Table 5.3.

5.5 Other Corrections and Systematic Errors

5.5.1 Beam Energy Correction

Previous analysis [52][53] of CLAS data suggests a slight miscalibration of the beam energy provided to Hall B. There are several straightforward methods to

Table 5.3. Empty target corrections

Run Period	Correction Factor
2.5 GeV 40%	0.971
2.5 GeV 60%	0.975
4.0 GeV 60%	0.977
4.2 GeV 60%	0.973

determine the amount by which the beam energy must be adjusted. The first method is to use the kinematics of either the scattered electron or proton from elastic events. If only the scattered electron track is used, the beam energy is given by

$$E_{Beam} = \frac{p_e}{(1 - \frac{p_e}{M_p}(1 - \cos\theta_e))}, \tag{5.15}$$

where p_e is the momentum of the scattered electron, M_p is the mass of the proton, and θ_e is the laboratory polar angle between the beam direction and the scattered electron. If the proton tracks are used instead, the beam energy can be derived from the mass of the proton, M_p, the energy of the proton, E_p, and the laboratory polar angle between the beam and the scattered proton, θ_p as follows:

$$E_{Beam} = \frac{E_p M_p - M_p^2}{M_p - E_p + p_p \cos\theta_p}. \tag{5.16}$$

For the 4.2 GeV 60% data, Eq. 5.15 produces the distribution shown in the top plot of Fig. 5.17 while Eq. 5.16 produces the bottom distribution[53]. The mean of the Gaussian fit to each distribution demonstrates that a beam energy correction factor of 1.008 is needed.

Another method to determine the beam energy scaling factor is to adjust the beam energy until a well defined value is reproduced. This method was employed in the analysis of $\Lambda(1520)$ events for the 4.2 GeV 60% data set[53]. The top distribution of Fig. 5.18, taken from [53], plots the mean value of the electron-K^+ missing mass peak for $\Lambda(1520)$ events versus the beam energy scaling factor. The bottom part of the figure shows the mean value of the electron-K^+-proton missing mass peak, which

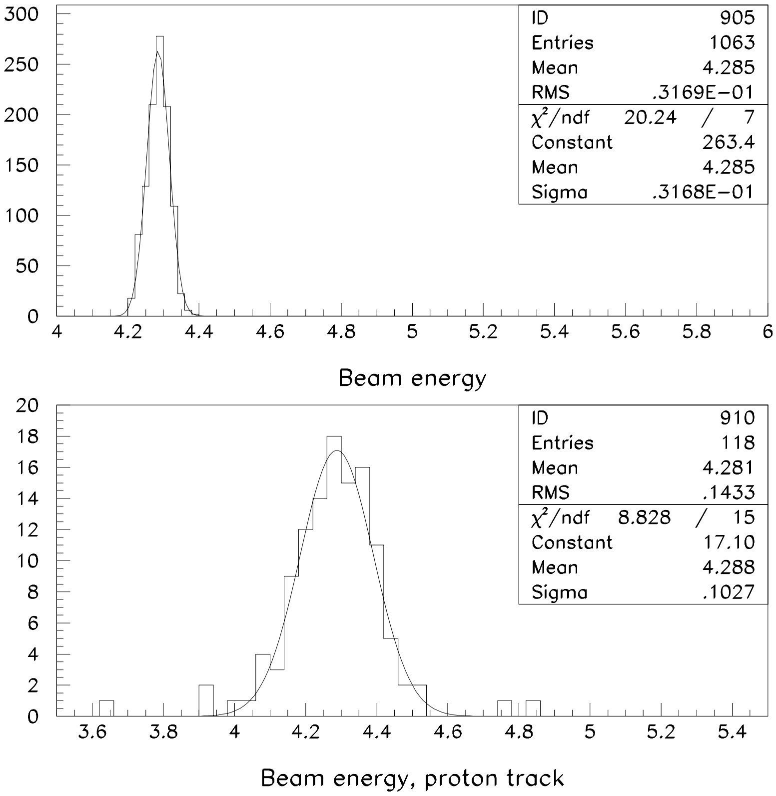

Figure 5.17. The top plot shows a calculation for the incident beam energy using the electron track and Eq. 5.15 for elastic events from the 4.247 GeV 60% data. The calculated beam energy using only the proton track, and Eq. 5.16, is shown in the bottom distribution. Figure from [53].

should be the mass of a K^-, versus the beam energy scaling factor, also for $\Lambda(1520)$ events. The dashed lines in both plots indicate the nominal mass of the missing particle from Ref. [22]. The slight difference between the ideal beam scaling factor in these two plots is not troublesome since there is a 1 GeV uncertainty in the mass of the $\Lambda(1520)$[22]. Additionally, in the analysis, the $\Lambda(1520)$ missing mass peak has a radiative tail and sits on a sizeable background absent from the K^- missing mass peak. Both plots, though, still indicate the nominal beam energy is too low, which is consistent with the results from the first technique.

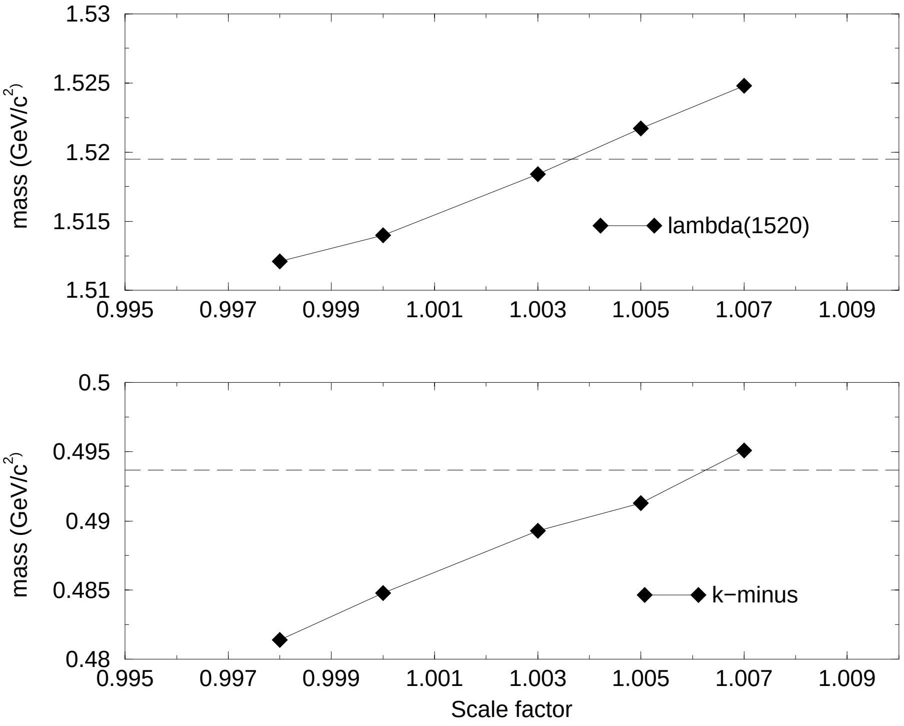

Figure 5.18. The top plot shows the mean value of the reconstructed mass peak of the $\Lambda(1520)$ versus the beam energy scaling factor for the 4.247 GeV 60% data. The bottom plot shows the mean value of the reconstructed K^- from the eK^+p missing mass peak for $\Lambda(1520)$ events versus the beam energy scaling factor. The dashed lines indicate the nominal masses of the missing particles from [22]. Figure from [53].

The beam energy scaling factor for this analysis was determined for each data set using the second method just described. The results of this analysis can be found in Table 5.4 and employ the electron-K^+ missing mass for $\Lambda(1116)$ events. The electron-K^+-proton missing mass squared is not used due to its proximity to zero mass and lack of a proper Gaussian shape. The systematic error in the acceptance corrections introduced by this correction factor is less than 1%.

Table 5.4. Beam energy correction factors

Beam Energy (GeV)	Torus Current (A)	Correction Factor
2.567	1500	1.005
2.567	2250	1.005
4.056	2250	1.006
4.247	2250	1.007

5.5.2 Energy Loss Corrections

As particles pass through CLAS, they lose energy through multiple scattering and showering processes. As mentioned in Sec. 5.2.1.2, GSIM takes these effects into consideration, automatically folding them into the geometric acceptance. Some analyses, however, correct the momentum of particles in the data to improve reconstructed values such as missing mass resolutions. With the exception of protons with momentum less than 0.45 GeV, Figs. 5.19 and 5.20 demonstrate the energy losses are of the order of 1% or less for the kinematics involved in this analysis. Therefore, protons with momentum less than 0.45 GeV are dropped from the analysis and no dE/dx corrections are applied to the remainder if the data. This introduces a systematic error of less than $\sim 1\%$.

5.5.3 Beam Charge Asymmetry

As shown in Eq. 1.33, if the electron beam is unpolarized, the only nonzero projection operator for the $\Lambda(1116)$ polarization lies along the direction normal to the hyperon production plane. If the beam is polarized, however, the polarization projection operator can be nonzero along the other two axes.

As mentioned in Chapter 2, the electron beam used in the study was polarized. In this analysis, the results are summed over both beam helicity states. If the beam charge asymmetry is zero, this summation should result in the equivalent of an unpolarized beam. The beam charge asymmetry for the E1C experiment, however, was not zero. The asymmetry was measured for the 2.5 GeV and 4.2 GeV data sets

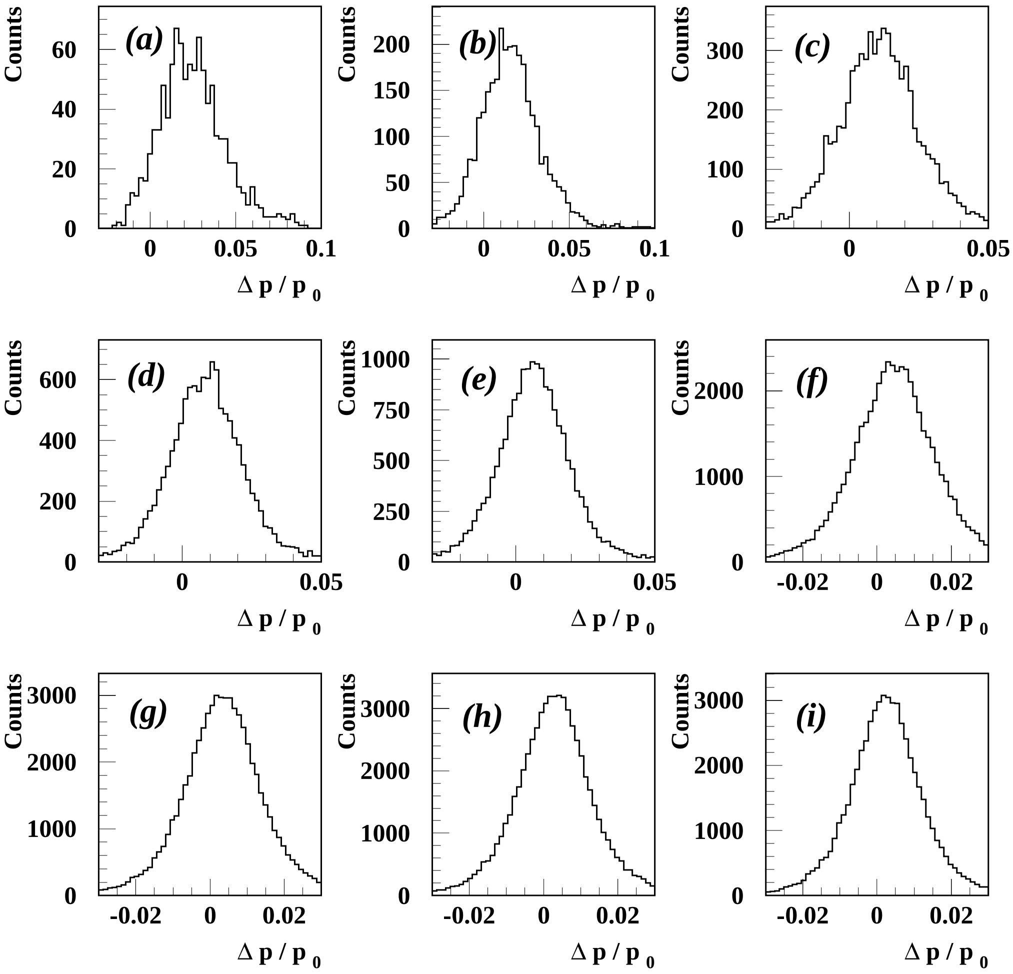

Figure 5.19. GSIM simulation of dE/dx for proton tracks in the 2.5 GeV 40% data set. Δp is the difference between the original proton momentum, p_0, and the reconstructed momentum. (a) Proton tracks with $p_0 < 0.4$ GeV, (b) 0.4 GeV $< p_0 <$ 0.45 GeV, (c) 0.4 GeV $< p_0 <$ 0.45 GeV, (d) 0.45 GeV $< p_0 <$ 0.5 GeV, (e) 0.5 GeV $< p_0 <$ 0.55 GeV, (f) 0.55 GeV $< p_0 <$ 0.6 GeV, (g) 0.6 GeV $< p_0 <$ 0.7 GeV, (h) 0.7 GeV $< p_0 <$ 0.8 GeV, (i) 0.8 GeV $< p_0 <$ 0.9 GeV.

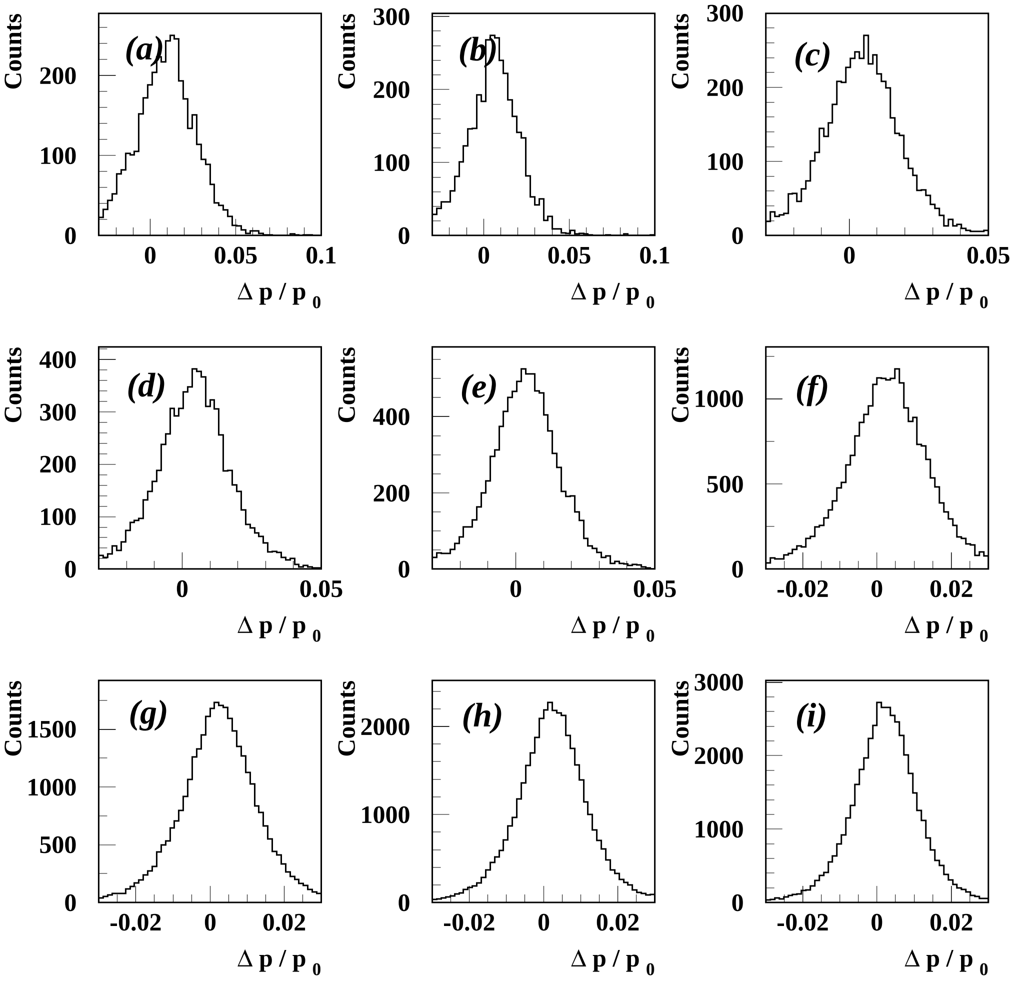

Figure 5.20. GSIM simulation of dE/dx for kaon tracks in the 2.5 GeV 40% data set. Δp is the difference between the original kaon momentum, p_0, and the reconstructed momentum. (a) Kaon tracks with $p_0 < 0.4$ GeV, (b) 0.4 GeV $< p_0 < 0.45$ GeV, (c) 0.4 GeV $< p_0 < 0.45$ GeV, (d) 0.45 GeV $< p_0 < 0.5$ GeV, (e) 0.5 GeV $< p_0 < 0.55$ GeV, (f) 0.55 GeV $< p_0 < 0.6$ GeV, (g) 0.6 GeV $< p_0 < 0.7$ GeV, (h) 0.7 GeV $< p_0 < 0.8$ GeV, (i) 0.8 GeV $< p_0 < 0.9$ GeV.

using elastic e-p scattering [54]. For the majority of runs in these two data sets, the beam asymmetry was quoted to be less than than 1%.

The beam asymmetry was not studied for the 4.0 GeV E1C data set since there was significant beam contamination from beam delivered to Hall C[54]. Therefore, there is no direct measure in CLAS of the beam helicity for each electron beam bucket in this data set. The polarization results look essentially the same though, with and without the inclusion of the $E_{Beam} = 4.0$ GeV data. Therefore, this data set is included in the analysis with the assumption that the beam asymmetry is less than 1%.

5.5.4 Luminosity

The total integrated luminosity for a reaction is given as

$$\mathcal{L} = N_{Beam} N_{Target}, \tag{5.17}$$

where N_{Beam} is the number of electrons incident on the target throughout the experiment and N_{Target} is the areal density of protons in the target. N_{Beam} can be determined through the equation

$$N_{Beam} = \frac{Q_{Total}}{e} = \frac{FC_{Total}}{e} \cdot \frac{0.1nC}{1\ FC\ click} \tag{5.18}$$

where Q_{Total} is the total integrated charge, e is the charge of the electron, and FC_{Total} is the total number of clicks recorded by the clock-gated Farady cup. N_{Target} can be determined through

$$N_{Target} = \frac{\rho t A}{\omega} \tag{5.19}$$

where ρ is the target density, t is the target length, A is Avagadro's number, and ω is the molar weight of the target material. Using these equations and the target information from Sec. 2.4.6 yields the integrated luminosities presented in Table

Table 5.5. Total integrated luminosities

Beam Energy (GeV)	Torus Current (A)	Integrated Luminosity ($\times$ 10^{39} cm^{-2})
4.056	2250	1.24
4.247	1500	1.45

Table 5.6. Summary of systematic Errors

Source of Error	Uncertainty	Correction Factor
Beam Charge Asymmetry	$< 1\%$	-
Close Track Reconstruction	$\sim 2\%$	-
Beam Energy Correction	$< 1\%$	see Table 5.4
Mass Cuts	$\sim 2\%$	-
Empty Target Corrections	$\sim 1\%$	see Table 5.3
Acceptance Cutoffs	$\sim 5\%$	~ 1.10
Radiative Corrections	$\sim 2\%$	~ 1.20
dE/dx Correction	$< 1\%$	-
Branching ratios	$< 1\%$	-
Luminosities	$\sim 3\%$	-

5.5. Only two data sets are presented since only these were used for cross section measurements. A study of the elastic cross section, though, suggests an upper limit of $\sim 3\%$ systematic error involved in these values[55].

5.5.5 Summary of Systematic Errors

Table 5.6 summarizes the systematic errors involved in this analysis, most of which are discussed in this chapter. The first three errors are the most important since they contribute to errors in the polarization results. The last seven errors mainly contribute as an overall scaling factor to the polarization results. The total systematic error is much smaller than the statistical errors in this analysis.

CHAPTER 6

RESULTS AND CONCLUSIONS

6.1 General Results

As mentioned in Chapter 1, this thesis dramatically improves our knowledge of the recoil polarization of electroproduced $\Lambda(1116)$ compared to previous measurements. Additionally, this thesis is the culmination of many new and essential techniques developed to analyze the data. For example, with the help of Dr. Manak, in the course of this work new strategies and tools, described in Chapter 4, were initiated and developed to process and monitor the large amounts of data acquired by CLAS. This thesis can also be used as the first blueprint, developed with the assistance of Dr. Barrow, for the acceptance calculations that must be performed on the CLAS data and the utilization of a batch CPU farm to accomplish this task.

By implementing all of these techniques and tools mentioned in the preceding chapters, CLAS is able to measure kinematically complete $\Lambda(1116)$ events over a large kinematic range. For the first time, polarization data were taken over the full center of mass angular range, $0.5 < Q^2 < 3.0$ GeV^2, and W from threshold to 2.3 GeV. The acceptance corrected Q^2 and W yields are presented in Fig. 6.1. The sharp cutoff in Fig. 6.1(a) is a result of the kinematic limits of the acceptance lookup table for the 2.5 GeV data. The kinematic range of the acceptance lookup tables for $E_{Beam} > 3.0$ GeV, on the other hand, is wider than the present range of the data. The acceptance corrected center of mass angles, presented in Fig. 6.2, show the full angular range available with CLAS.

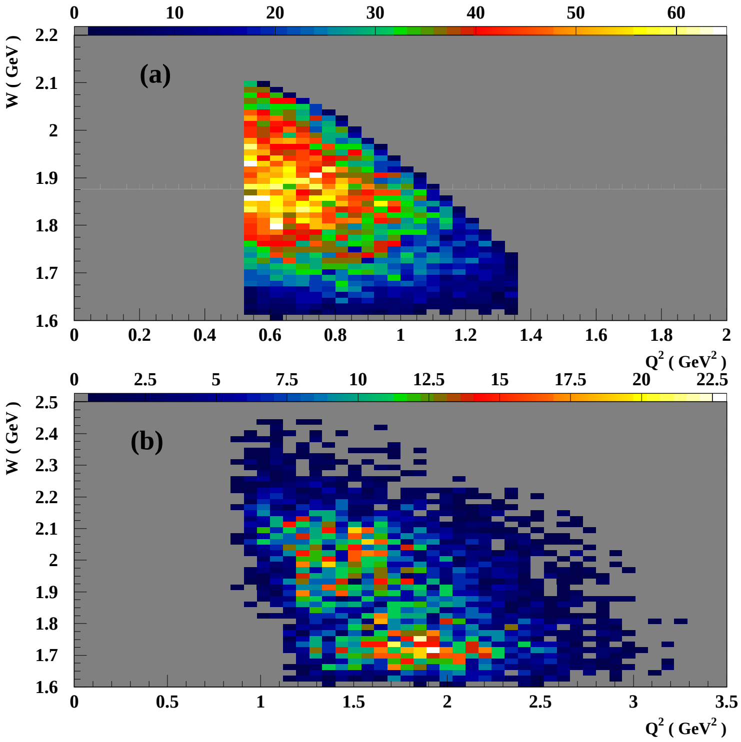

Figure 6.1. Acceptance corrected Q^2 versus W for kinematically complete $\Lambda(1116)$ events for (a) E_{Beam} = 2.5 GeV and (b) $E_{Beam} > 3.0$ GeV.

As mentioned in Chapter 1, prior to this thesis there has been only one data point reported for electroproduced $\Lambda(1116)$ recoil polarization. This data point was recorded in Hall C with 40 kinematically complete events at $Q^2 = 1.50$ GeV^2 and $\theta^{cm}_{K\gamma} = 14^\circ$ with a quoted polarization between -0.21 and 0.89[21]. Therefore, there are no previous measurements that can be compared with the current data. As a result, before presenting the polarization results, two other measurements for which there are many previous studies will be reported. The polarization results will then be presented in a subsequent section.

6.1.1 Lifetime

A study was made of events containing an electron, K^+, proton, and π^- that satisfy all the particle and event identification cuts specified in Chapter 3. For

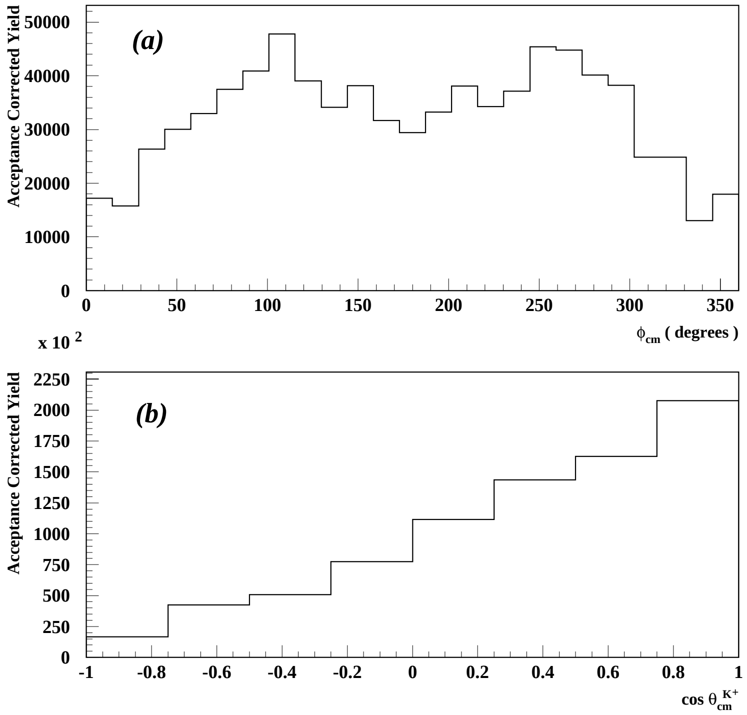

Figure 6.2. Acceptance corrected center of mass angles (a) ϕ_{cm} and (b) $\cos\theta_{cm}^{K+}$ for kinematically complete $\Lambda(1116)$ events.

these events, a common vertex was determined for the electron and the K^+ tracks. Similarly, a vertex was identified for the proton and π^- tracks. The difference between these two vertices, as shown in Fig. 6.3, defines the distance in the laboratory frame traveled by the $\Lambda(1116)$ before its decay. Since the $\Lambda(1116)$ is traveling at relativistic speeds, this distance is converted to the proper time using

$$\beta = \frac{|p|}{E} \tag{6.1}$$

and

$$\gamma = \frac{E}{M}. \tag{6.2}$$

Fit to an exponential dependence, the data for $E_{Beam} = 2.5$ GeV shown in Fig. 6.4 indicate a mean flight path, $c\tau$, for the $\Lambda(1116)$ of $8.10^{+0.61}_{-0.53}$ cm. Within error this

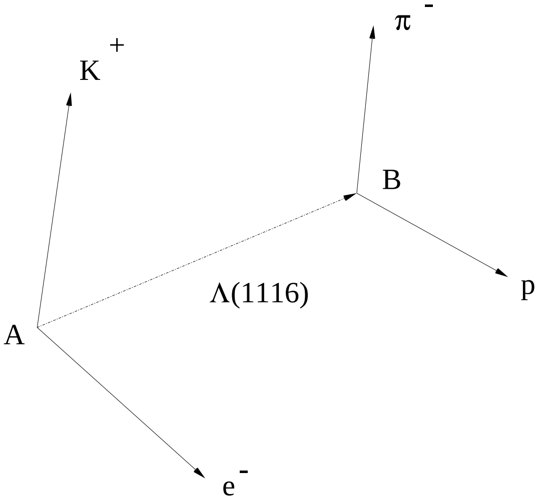

Figure 6.3. Vertex A represents the position at which the $\Lambda(1116)$ and K^+ are created as the electron scatters off the target proton. Vertex B represents the point at which the $\Lambda(1116)$ decays into a proton and π^-. The difference between these two vertices allows us to measure the lifetime of the $\Lambda(1116)$.

number is in good agreement with the established value of $c\tau = 7.89$ cm for the $\Lambda(1116)$[22].

6.1.2 Cross Section

The Q^2 dependence of the $\Lambda(1116)$ cross section from previous measurements is summarized in Fig. 6.5[60]. These experiments detected the scattered electron and K^+ using two arm spectrometers over a wide range of kinematics. The data presented in Fig. 6.5 were therefore scaled in W, ϵ, and θ_{cm} so that <W> = 2.15 GeV and θ_{cm} = 0°. The data in this figure were fit with the function A/(Q^2 + B)^2 resulting in A=3979.3 and B=2.67.

Using CLAS events containing an electron, K^+, and proton, at $E_{Beam} > 3.0$ GeV, Fig. 6.6 shows the Q^2 dependence of the $\Lambda(1116)$ cross section for $2.0 < W < 2.2$GeV and $\cos\theta_{cm}^{K+} > 0.4$. The data is corrected for acceptance, radiative effects, and empty target corrections. The data is scaled to accommodate the branching ratio of the $\Lambda(1116)$, the acceptance cutoff, and binning. The CLAS data, though, is not scaled

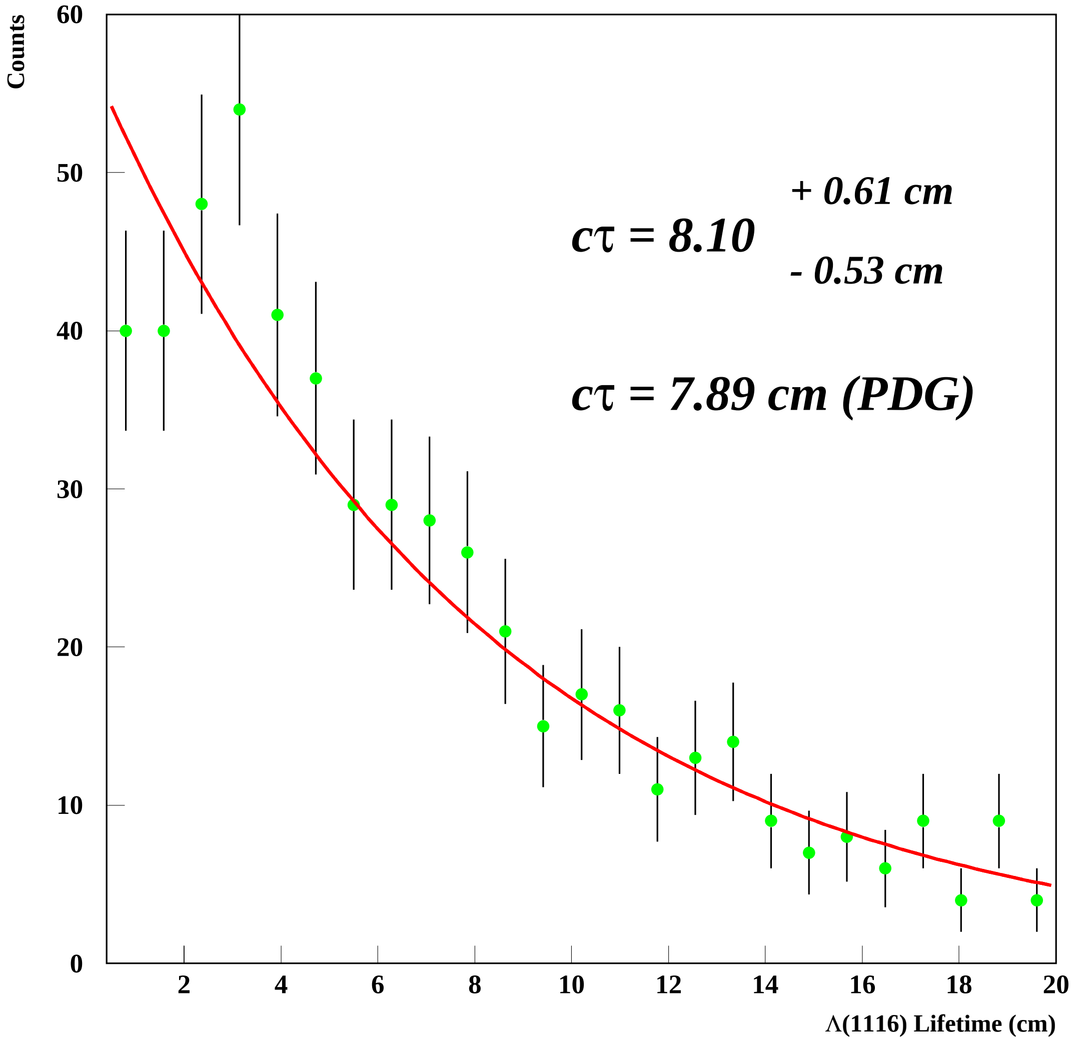

Figure 6.4. Measurement of the in flight decay of the Λ(1116).

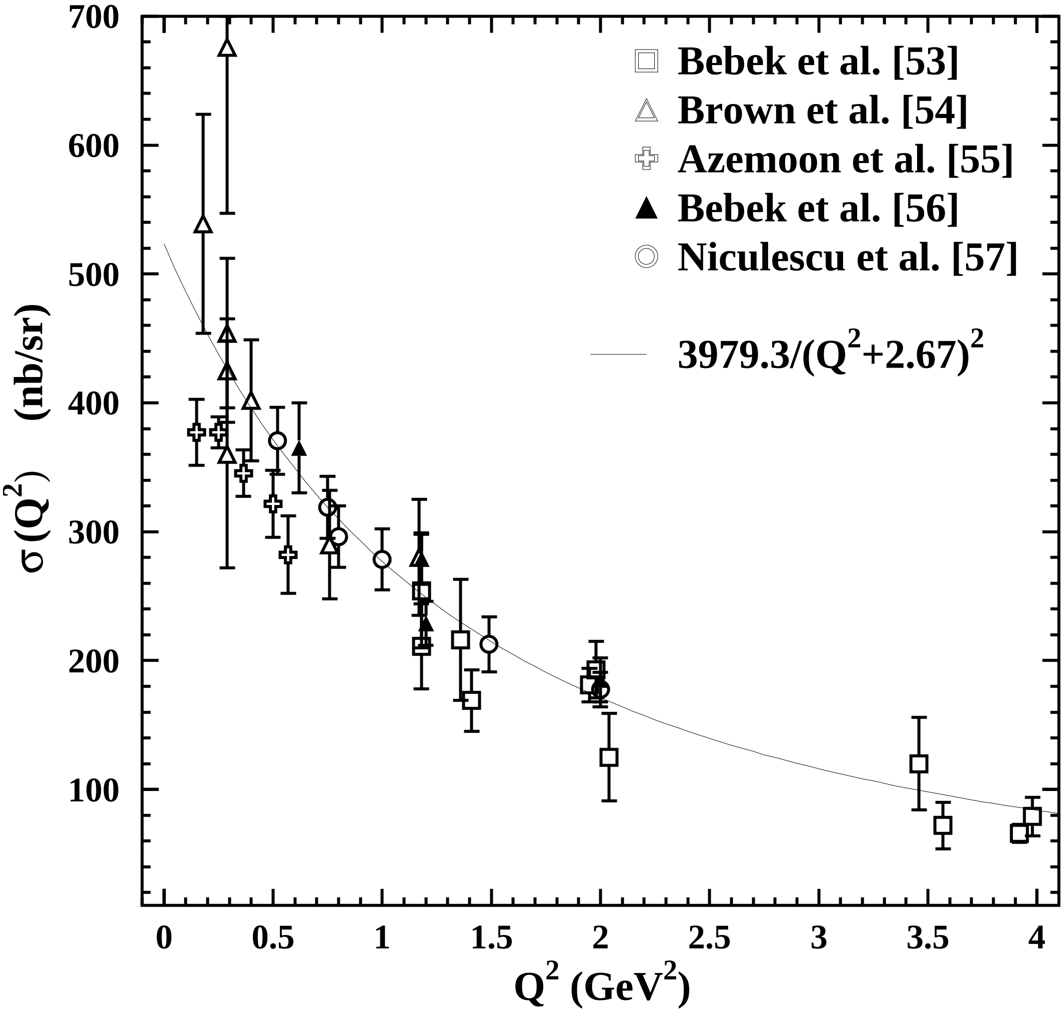

Figure 6.5. Q^2 dependence of the Λ(1116) cross section for previous measurements[60]. The data was scaled for different W, ϵ, and $\cos\theta_{cm}$ measurements. Further discussion of the scaling can be found in Ref. [60]. The data thus represent measurements taken at <W> = 2.15 GeV and θ_{cm} = 0°. The line represents a fit to the data using the the function A/$(Q^2$ + B$)^2$.

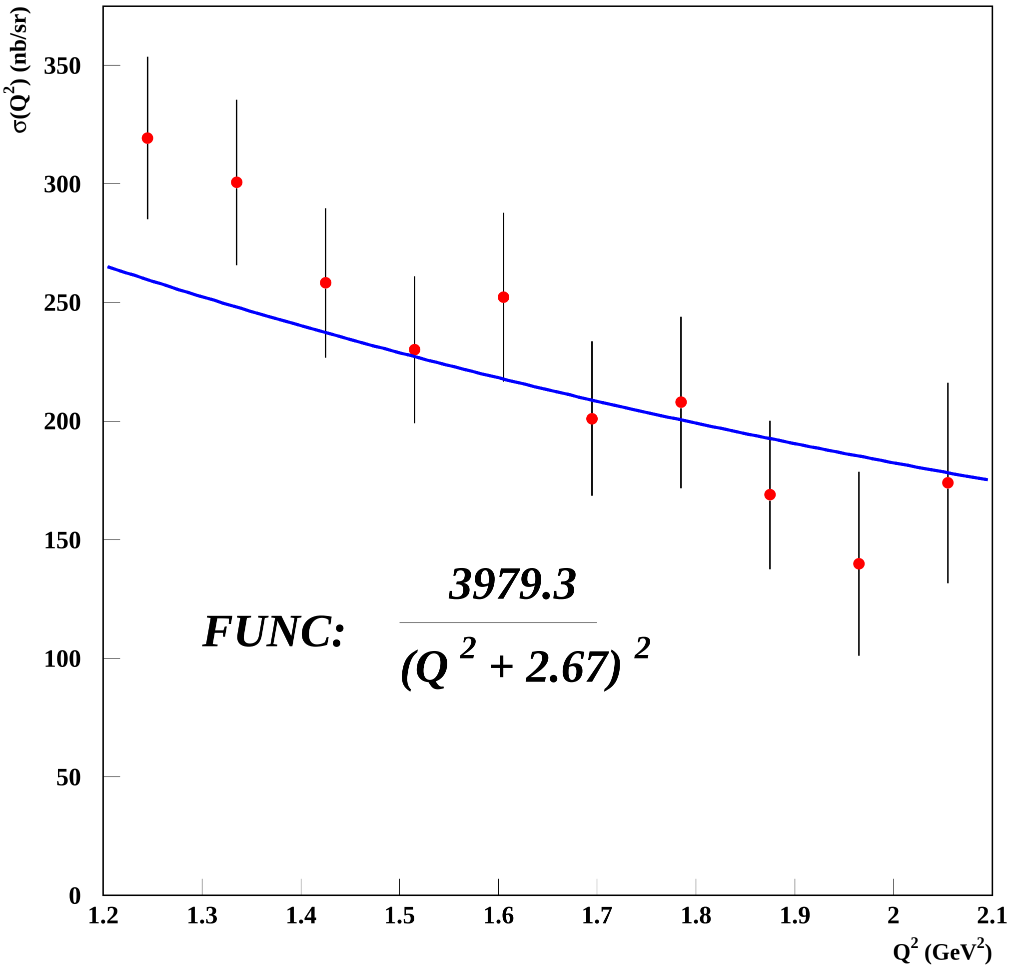

Figure 6.6. The Q^2 dependence of the $\Lambda(1116)$ cross section for $E_{Beam} > 3.0$ GeV data and electron, K^+, proton events. The data were constrained so $2.0 <$ W < 2.2 GeV and $\cos\theta_{cm}^{K+} > 0.4$. The error bars represent statistical errors only. The line through the data plots the function 3979.9 / $(Q^2 + 2.67)^2$ used in [12].

for W, ϵ, or θ_{cm} in the same manner as the data in Fig. 6.5. The cuts placed on the CLAS data to constrain the kinematic region to a region comparable to the measurements in Ref. [60] limit the Q^2 range.

Plotted in Fig. 6.6, is the function derived in [60]. This function shows that the CLAS data does not follow the exact Q^2 dependence derived in Ref. [60]. This could be due to the fact that Ref. [60] fit the cross sectional dependence over a much larger Q^2 range. Another possible source of the discrepancy between the two Q^2 dependencies is that the previous data were scaled in W, $\cos\theta$ and ϵ. The CLAS data as mentioned before was not scaled for these variables. The more important fact to notice from Fig. 6.6, though, is that the average value of the CLAS cross section is in very good agreement with the previous measurements.

Based on this cross section result and the lifetime measurement, CLAS is able to reproduce with good accuracy previous data using the methods established in the previous chapter. It is now possible to move on to the polarization results.

6.2 Recoil Polarization

The polarization experiments mentioned in Chapter 1, Refs. [15]-[19] and Ref. [21], positioned one counting telescope above the hyperon production plane and one counting telescope below the hyperon production plane. The polarization was then determined from

$$P \propto \frac{N_+ - N_-}{N_+ + N_-}, \tag{6.3}$$

where N_+ is the number of decay protons measured in the upper telescope and N_- is the number of decay protons measured in the lower telescope. CLAS, however, has a nearly 4π coverage in the laboratory frame of reference. Therefore, the simple static counting method used in previous studies is not employed. Instead, the rest frame of the $\Lambda(1116)$ is derived for each event according to Fig. 6.7. In order to transform to this frame, the energy and momentum of the particles are boosted and rotated to the center of mass coordinate system where $\hat{z}$ points along the direction of the virtual photon, $\hat{y}$ is perpendicular to the hyperon production plane, and $\hat{y} \times \hat{z} = \hat{x}$. The perpendicular to the hyperon production plane is defined as the cross product of the virtual photon direction and the K^+ direction. The particles are then boosted to the $\Lambda(1116)$ rest frame in which $\hat{l}$, the longitudinal axis, points along the direction of motion of the $\Lambda(1116)$, $\hat{n}$, the normal axis, points out of the hyperon production plane, and $\hat{n} \times \hat{l} = \hat{t}$, the transverse axis.

The direction of the outgoing proton from the $\Lambda(1116)$ decay in the $\Lambda(1116)$ rest frame is then projected onto each of these axes. The angular distributions along the polarized axis follow

$$\frac{dN}{d\Omega^p_{rf}} \propto 1 + \alpha P_\Lambda \cos\theta^p_{rf}, \tag{6.4}$$

where $\alpha = 0.642 \pm 0.013$ [22]. Here α is determined by PDG by averaging a number of experimental values. In general, though, α may be determined experimentally by looking at the angular distribution of protons from the decay of unpolarized $\Lambda(1116)$. Protons from the unpolarized set will produce a distribution of the form

$$\frac{dN}{d\Omega^p} \propto 1 + \alpha \cos\theta^p, \tag{6.5}$$

The proton angular distributions from the polarized $\Lambda(1116)$ sample used in this thesis are fit with a polynomial of order 1 whose slope is then normalized and adjusted by α. The errors in the derived polarizations take into account the statistical errors of the data as well as the error in α. A sample fit is shown in Fig. 6.8. The fits to the unpolarized axes do not take into account α or its error. The full set of fits used in this analysis may be found in Appendix C.

Using these fits, a statistical analysis of the W dependence of the recoil polarizations further supports the analysis techniques used in this analysis. In this statistical

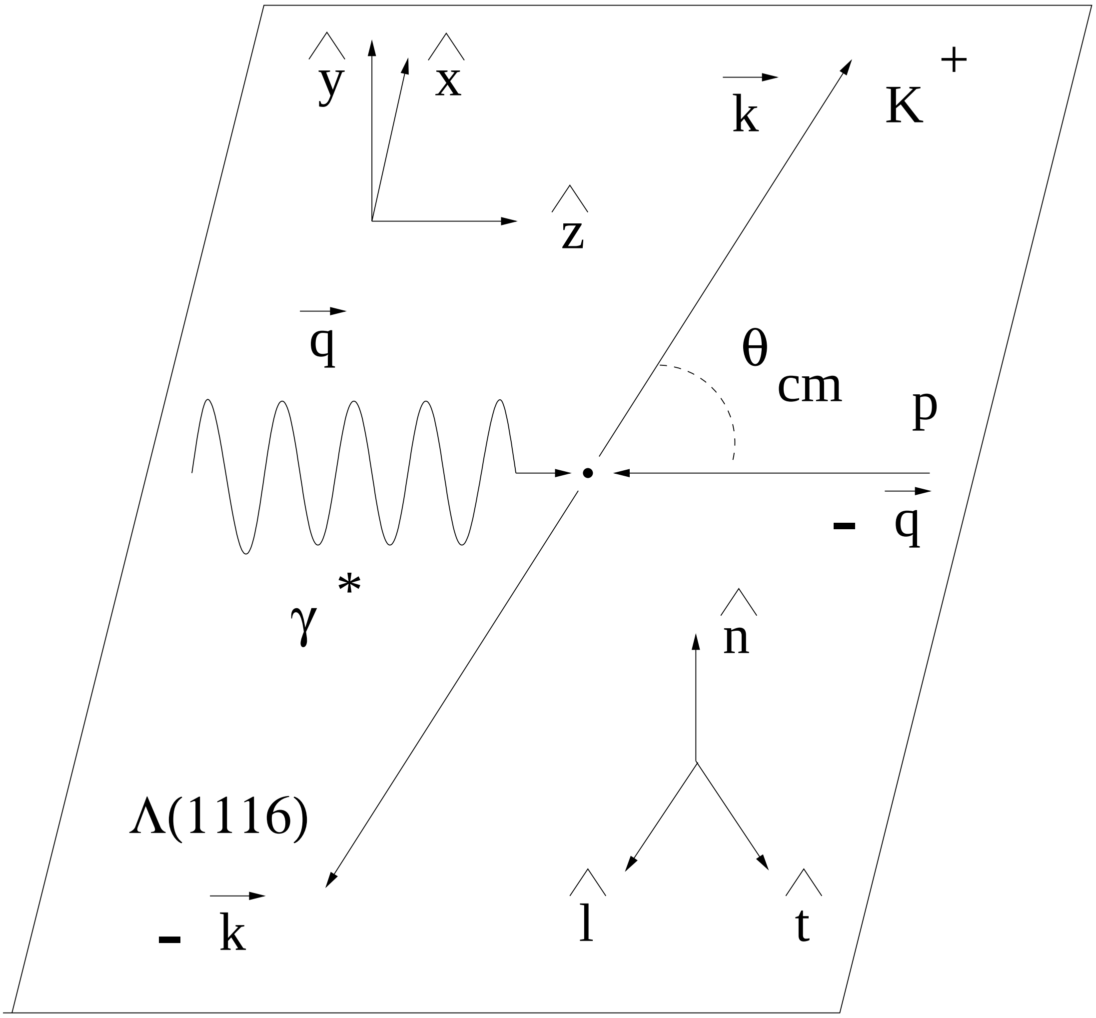

Figure 6.7. Schematic showing the directions of two different frames of reference used in this analysis. The directions $\hat{z}$, which points along the direction of the virtual photon, $\hat{y}$, which points out of the hyperon production plane, and $\hat{x}$ define directions used in the center of mass frame. The directions $\hat{l}$, $\hat{n}$, and $\hat{t}$ are the directions used in the $\Lambda(1116)$ rest frame. $\hat{l}$ points along the direction of the motion of the $\Lambda(1116)$. $\hat{n}$ points out of the hyperon production plane and $\hat{t}$ is defined by the cross product of $\hat{n}$ and $\hat{l}$.

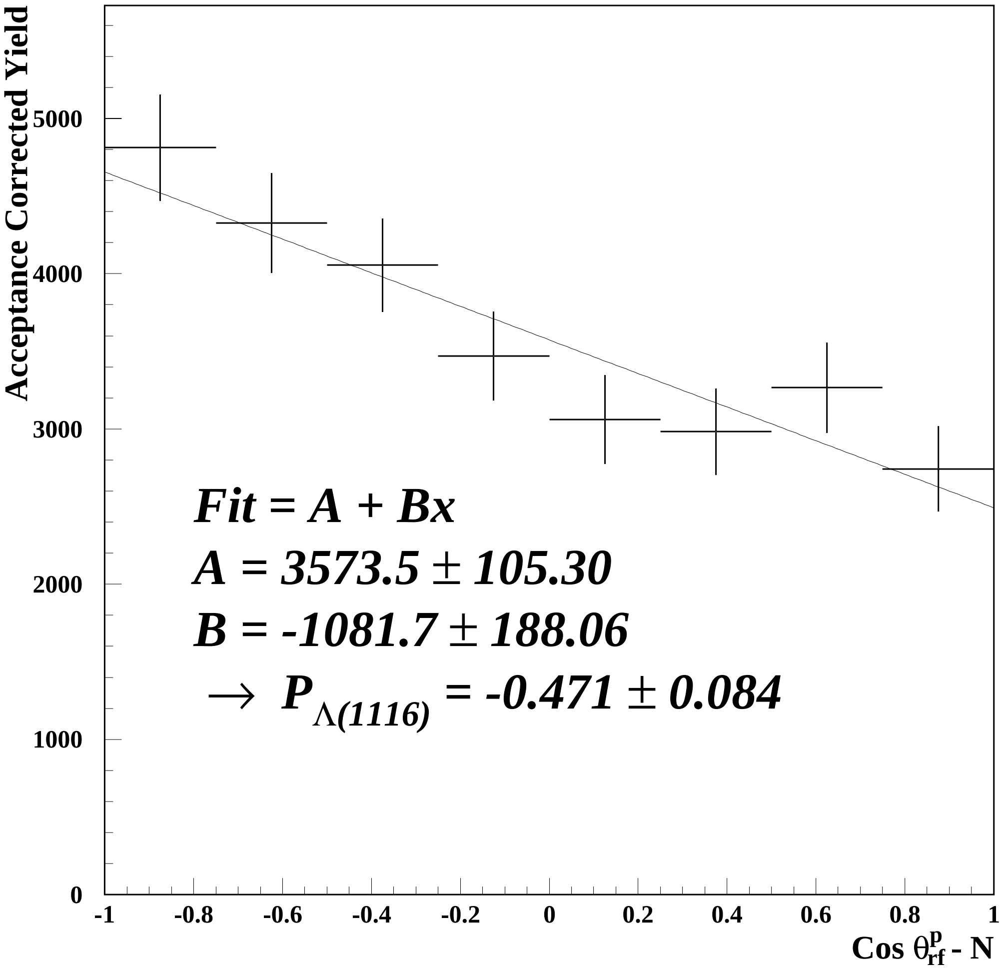

Figure 6.8. Sample fit of the angular distribution of the decay proton in rest frame of the $\Lambda(1116)$ along the normal axis. The fit parameters are normalized and adjusted by α in order to derive the polarization. Data are from $1.873 < \mathrm{W} < 2.152$ GeV and $0.2 < \cos\theta_{cm}^{K+} < 0.4$. Error bars on the data are statistical only.

Table 6.1. Reduced χ^2 values for the W dependent polarizations along the normal, transverse, and longitudinal axes. P1 χ^2 are the reduced χ^2 values for a linear fit. P0 χ^2 are the reduced χ^2 values for a constant fit.

W Range (GeV)	Normal Axis		Transverse Axis		Longitudinal Axis	
	P1 χ^2	P0 χ^2	P1 χ^2	P0 χ^2	P1 χ^2	P0 χ^2
1.61 - 1.716	6.46	8.694	2.338	2.005	2.368	4.582
1.716 - 1.766	2.186	6.817	1.442	1.425	1.388	1.192
1.766 - 1.816	1.188	9.143	1.341	1.160	0.965	1.064
1.816 - 1.866	1.767	9.143	1.561	1.341	2.278	1.963
1.866 - 1.916	1.910	7.293	3.596	3.105	1.938	1.670
1.916 - 1.966	1.057	7.038	1.219	1.069	0.909	0.836
1.966 - 2.016	1.426	5.333	1.299	1.149	1.396	1.767
2.016 - 2.066	1.011	4.168	2.572	2.223	1.247	1.069
2.066 - 2.116	2.298	2.829	1.900	1.631	1.655	2.159

analysis, the proton angular distributions in the $\Lambda(1116)$ rest frame are first fit with a linear function. The same distributions are then fit to a constant. The reduced χ^2 values from both of these fits are compared. According to a statistical $\mathcal{F}$ test[61], if the ratio of these two numbers is greater than 3.73, there is a 95% confidence that the extra fitting term is significant. In this analysis, a significant linear term suggests a nonzero polarization along a particular axis.

Table 6.1 reproduces the reduced χ^2 values for both the linear and constant fits along each $\Lambda(1116)$ axis. As mentioned in Chapter 1, the $\Lambda(1116)$ should only be polarized along the normal axis. For six of the nine W bins, the ratios of the reduced χ^2 values indicate that the linear term is significant along the normal axis. For the other two axes, none of the ratios suggests a significant linear fitting term. These results further validate the analysis techniques of Chapter 5.

The CLAS polarization data, shown in Figs. 6.9-6.11, were binned as a function of $\cos\theta_{cm}^{K+}$ and W to allow for comparison with the SAPHIR [20] photoproduction results shown in Fig. 1.6. A decomposition of the photoproduction cross section, led Tran *et al.* to fit the data in Fig. 1.6 with a combination of s- and p-waves. The CLAS data are therefore also fit with a combination of associated Legendre polynomials up

Table 6.2. Results of fit $A\cos\theta_{cm}^{K^+}\sin\theta_{cm}^{K^+} + B\sin\theta_{cm}^{K^+}$ for the $\Lambda(1116)$ recoil polarization for different W bins.

W Range (GeV)	A	B
1.617 - 1.716	-0.012 ± 0.111	-0.318 ± 0.056
1.716 - 1.873	0.174 ± 0.140	-0.569 ± 0.063
1.873 - 2.152	-0.183 ± 0.123	-0.485 ± 0.057

to order 1. At $\cos\theta_{cm}^{K^+} = 1$ and $\cos\theta_{cm}^{K^+} =$ -1, however, the virtual photon and the K^+ are parallel and anti-parallel, respectively. Therefore, the normal to the hyperon production, which is the cross product of these two directions, is equivalently zero and can not be defined. As a result, the Legendre polynomials must go to zero at these points, reducing the functional dependence to the form $A\cos\theta_{cm}^{K^+}\sin\theta_{cm}^{K^+} + B\sin\theta_{cm}^{K^+}$.

The results of the Legendre polynomial fits to the CLAS data are shown in Table 6.2. Although there are large differences between the relative importance of the fitted terms, not much reliability should be placed in these numbers. First, the variations in the Legendre fits mainly stem from data at back angles which suffer from a lack of statistics and a correspondingly large $\cos\theta_{cm}^{K^+}$ averaging interval. Secondly, with the data finely binned in both W and $\cos\theta_{cm}^{K^+}$, most of the individual polarization fits do not pass the statistical $\mathcal{F}$ test.

From Figs. 6.9-6.11, though, two main observations can be made. First, the data does not show the forward-backward asymmetry in $\cos\theta_{cm}^{K^+}$ seen in the photoproduction data. This could indicate that the longitudinal polarization of the virtual photon, absent in photoproduction plays a significant role in the electroproduction of the polarized $\Lambda(1116)$. Secondly, at forward angles, the data shows only a slight variation in the magnitude of the polarization for the different W bins. A similar trend is observed for the SAPHIR data[20]. As mentioned in Sec. 1.2, W is defined as the mass of the intermediate particle in an s-channel description of the production process. Therefore, a bump or dip in the W dependence of the recoil polarization could indicate contributions of different strengths from particular resonances. The

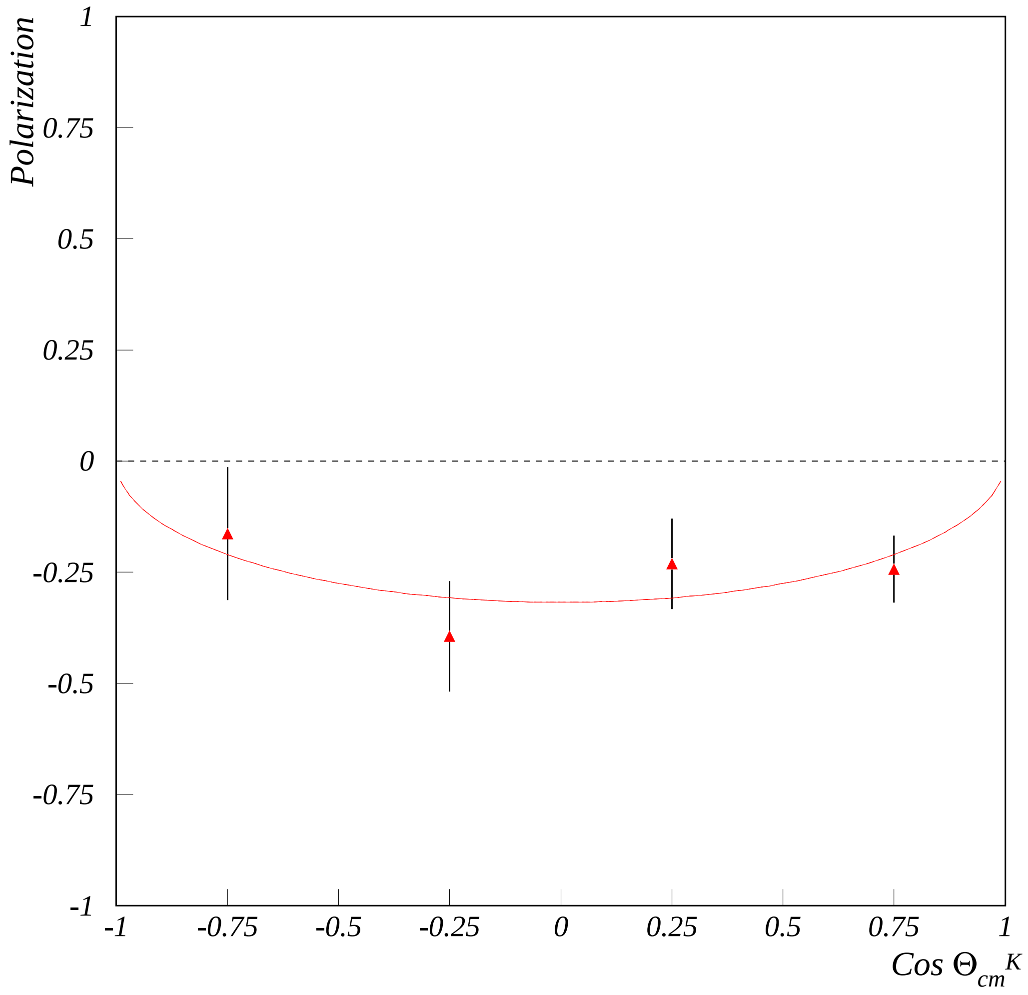

Figure 6.9. Recoil polarization along the axis normal to the hyperon production plane. Data is constrained to be between 1.67 < W < 1.76 GeV. Line represents an associated Legendre polynomial fit up to l=1.

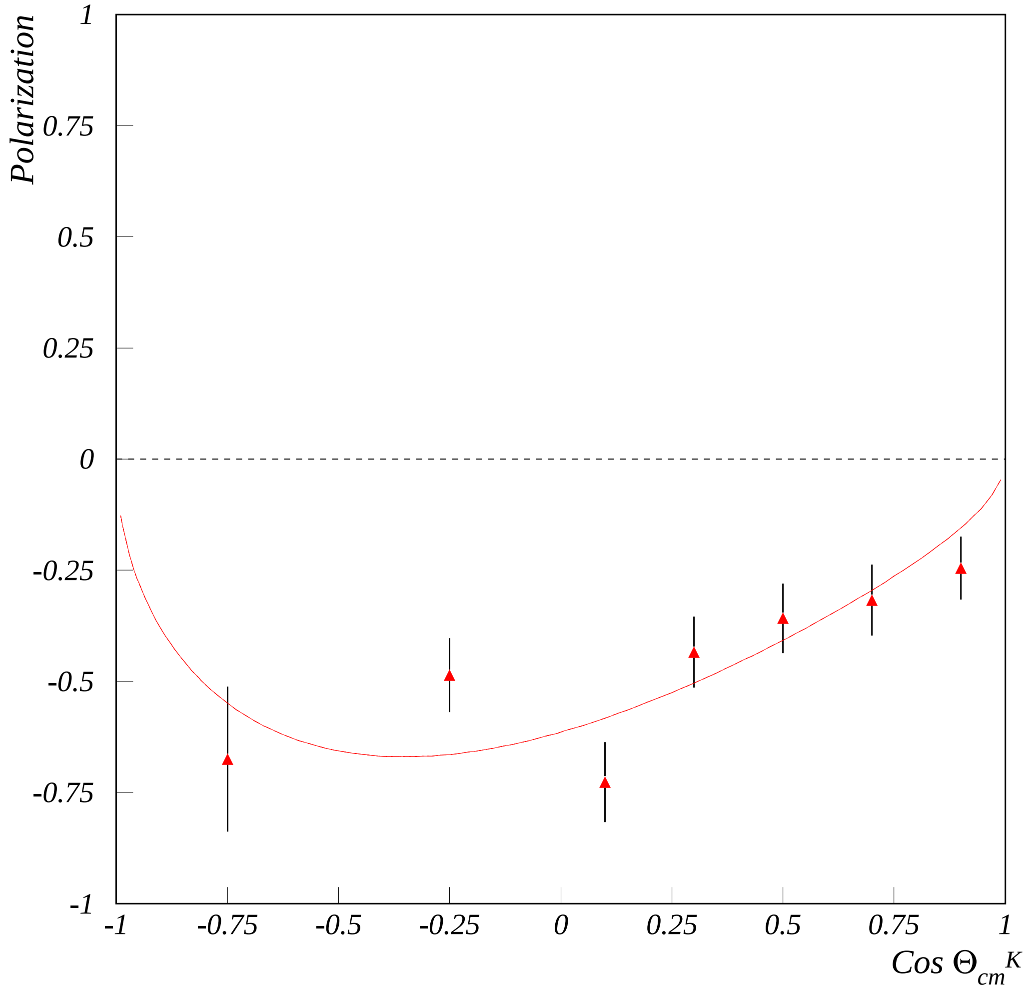

Figure 6.10. Recoil polarization along the axis normal to the hyperon production plane. Data is constrained to be between $1.716 < W < 1.783$ GeV. Line represents an associated Legendre polynomial fit up to l=1.

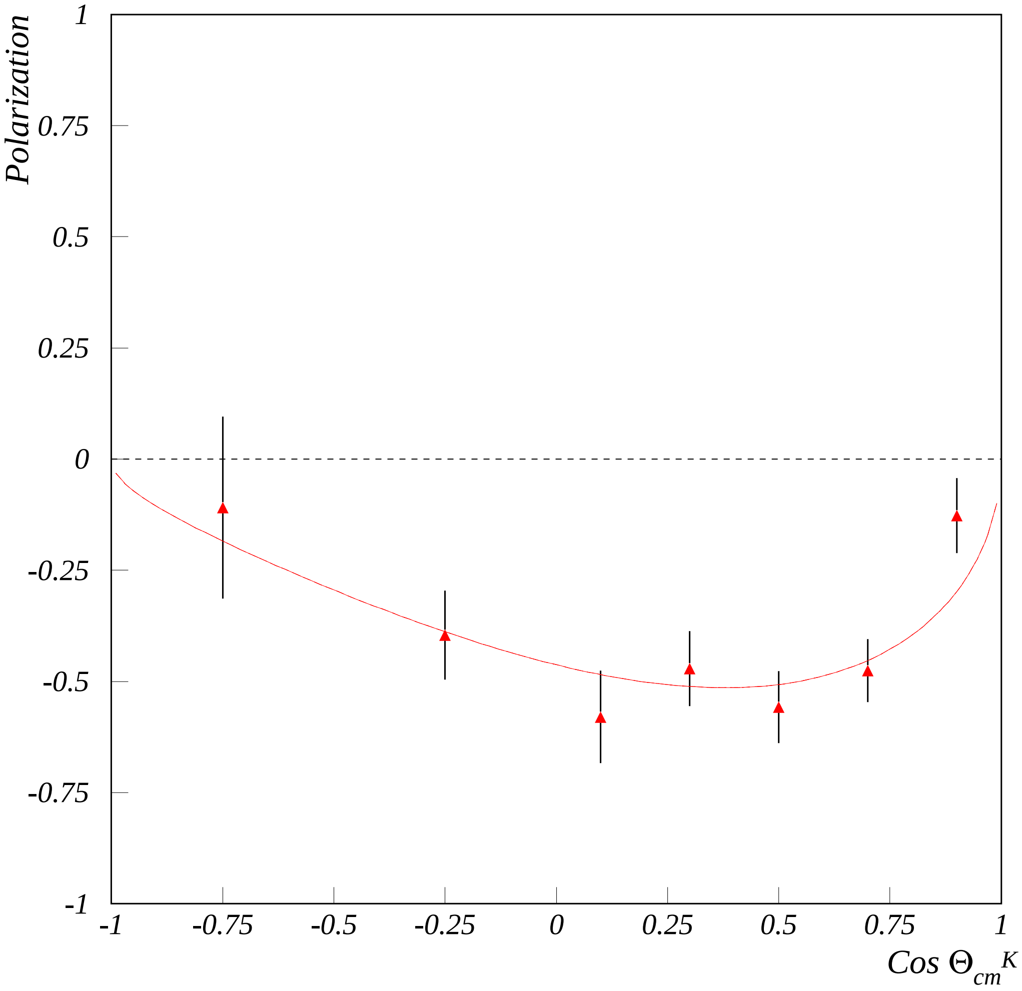

Figure 6.11. Recoil polarization along the axis normal to the hyperon production plane. Data is constrained to be between $1.873 < W < 2.152$ GeV. Line represents an associated Legendre polynomial fit up to l=1.

absence of W dependence, though, would indicate a lack of significant contributions from isobar excitations in contrast to the cross section data presented in [20].

To further examine the significance of resonances in the polarization, Fig. 6.12 plots the W dependence of the $\Lambda(1116)$ recoil polarization. To improve the statistics in the individual polarization fits, the data are summed over $\cos\theta_{cm}^{K+}$. Like Figs. 6.9-6.11, this figure shows a rather stable W dependence of the polarization. There is, however, a dip in the polarization for $1.866 < \mathrm{W} < 1.916$. This dip occurs at the vicinity of a $D_{13}(1895)$ resonance which is predicted by S. Capstick and W. Roberts [62] to have a significant $K\Lambda$ coupling. In Ref. [63], Bennhold *et al.* predicts that this resonance plays an important role in $\Lambda(1116)$ photoproduction. Ref. [63], though, claims that the recoil polarization is not sensitive to the existence of this resonance. As a further disclaimer, it must be noted that this dip still falls within the statistical error of the other polarization values. Therefore, more data and a full partial wave analysis is needed to validate the significance of this dip. As another check of the validity of the data, though, Figs. 6.13-6.14 show the W dependence of the proton angular dependence on the transverse and longitudinal axes. As expected, these projections are consistent with zero for all but two points in Fig. 6.14. The points at $1.61 < \mathrm{W} < 1.716$ GeV and $2.066 < \mathrm{W} < 2.116$ GeV in Fig. 6.14, though, are the result of poor fits and do not pass an $\mathcal{F}$ test significance criterion as shown in Table 6.1.

6.3 Conclusions

The CLAS event reconstruction reproduces well established values such as the Q^2 dependence of the $\Lambda(1116)$ cross section and the lifetime of the $\Lambda(1116)$. The CLAS data correctly yields zero $\Lambda(1116)$ polarization in the hyperon production plane. CLAS is also able to measure for the first time over a large kinematic range the rather large recoil polarization of the $\Lambda(1116)$. Without detailed theoretical calculations,

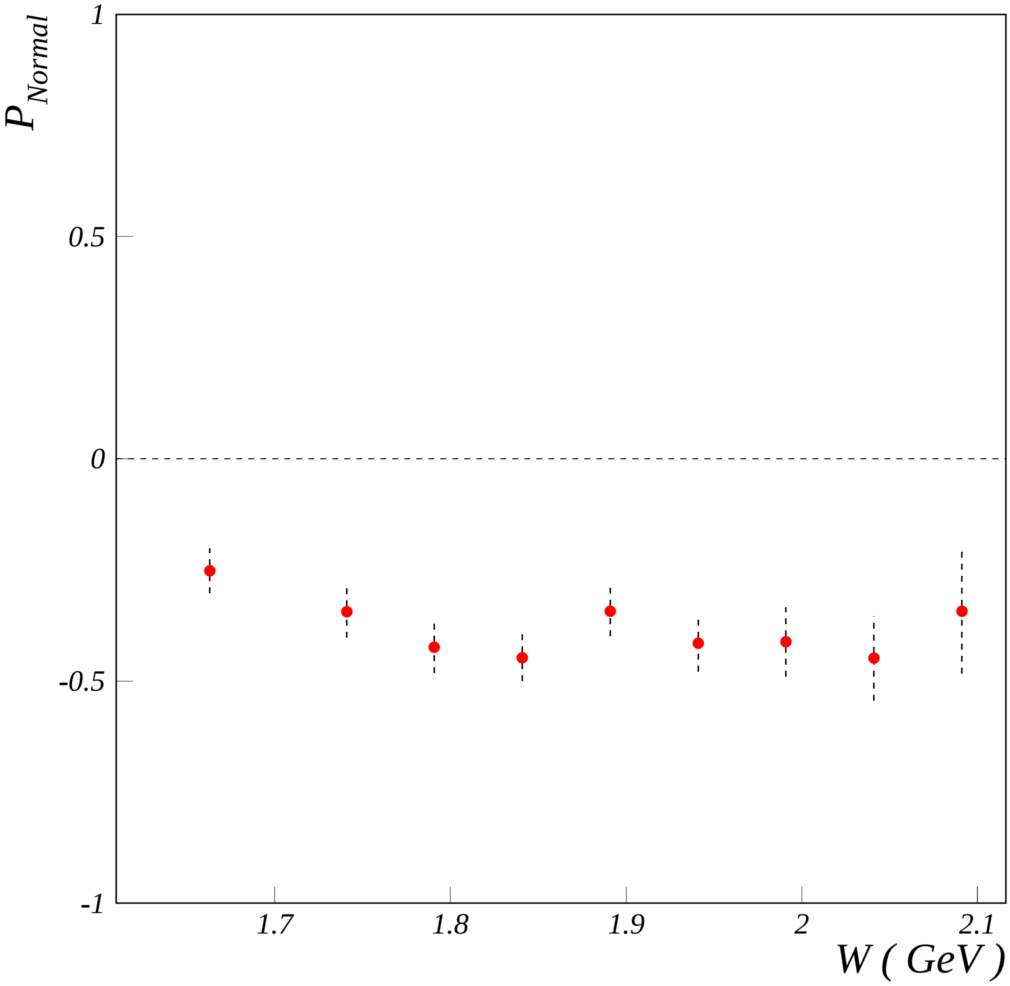

Figure 6.12. W dependence of the recoil polarization along the axis normal to the hyperon production plane.

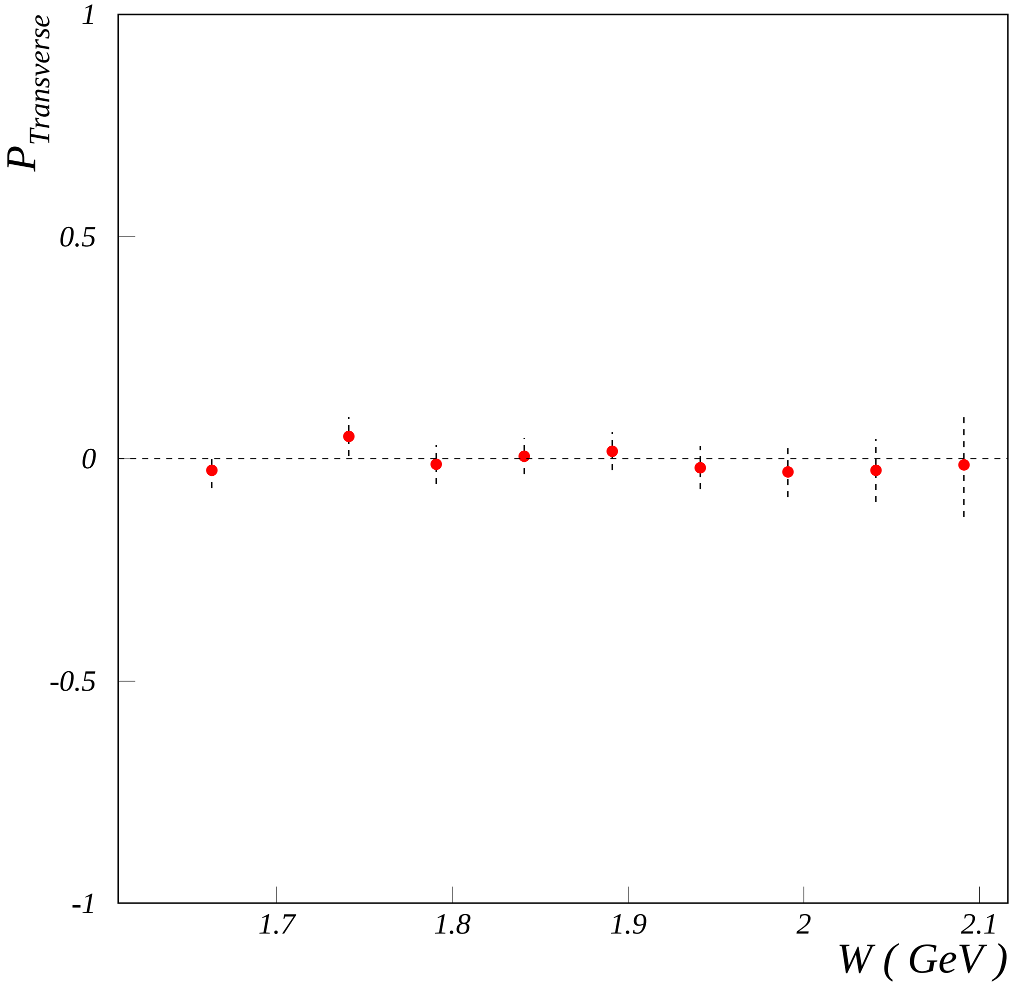

Figure 6.13. W dependence of the recoil polarization along the axis transverse to the hyperon production plane.

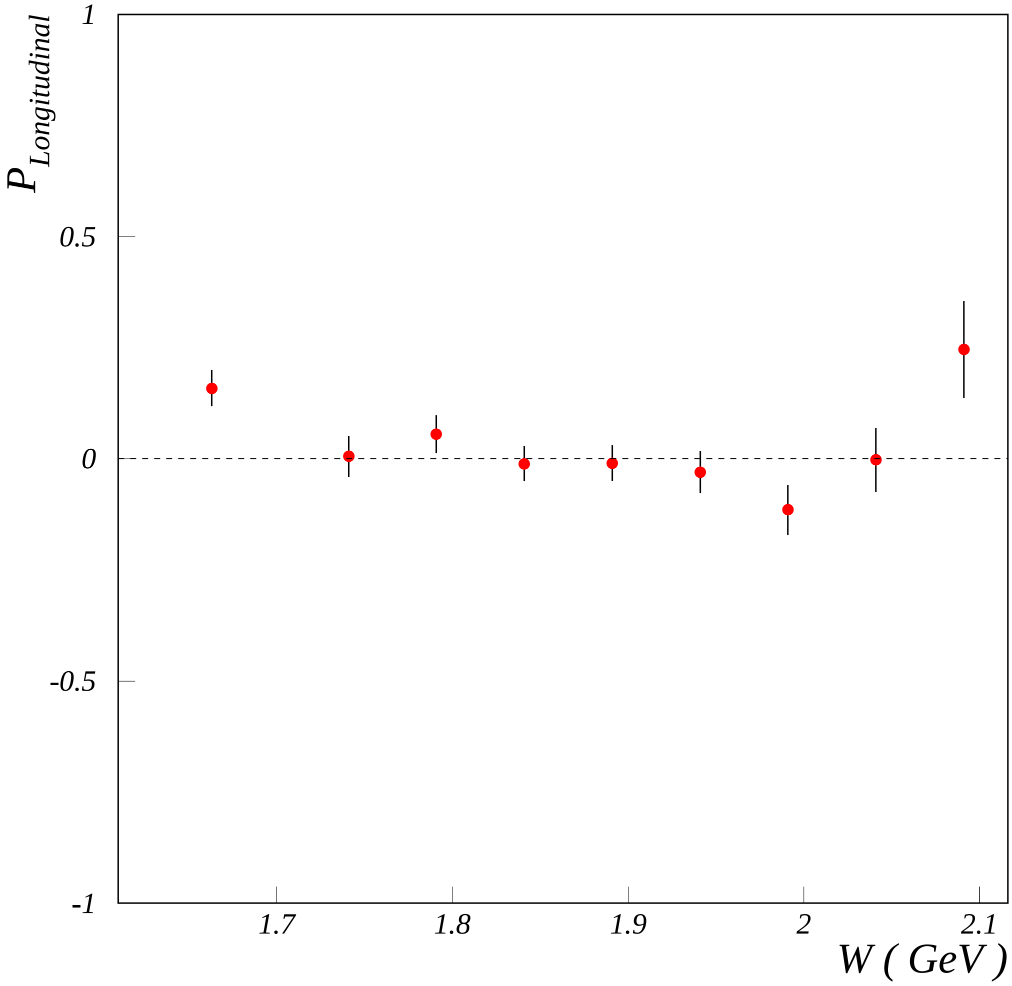

Figure 6.14. W dependence of the recoil polarization along the axis longitudinal to the hyperon production plane.

and for a limited data set, though, it is difficult to draw conclusive implications from the polarization data. Currently, none of the previously mentioned models are able to calculate consistent $\Lambda(1116)$ recoil polarizations.

The recoil polarization demonstrates a fairly smooth behavior as a function of W. This could indicate the lack of significant contributions from a few narrow s-channel diagrams. The interference from a number of broad s-channel resonances, though, could produce the same behavior. More data and a full partial wave analysis is therefore necessary to understand this behavior. Still, these CLAS results showing the negative sign and significant magnitude of the recoil $\Lambda(1116)$ polarization will go a long way towards constraining the existing phenomenological models and generating theoretical interest and the creation of new models.

6.4 Future Analysis

A large quantity of data useful to this analysis has already been taken. Approximately 30% more data was taken during the E1C run period and has already been cooked. During the E1D run period approximately 4 times more data was taken. This data set is in the calibration and cooking stages of analysis. The E1-6 experiment has just started taking data at an incident beam energy of 5.7 GeV. All of these data sets would greatly improve the statistics in the polarization analysis. With new beam energies and torus settings, though, there is a need for additional simulations. As shown in Sec. 5.2.1, this requires a large amount of CPU time.

As mentioned in Sec. 1.5, each new polarization degree of freedom in $\Lambda(1116)$ electroproduction accesses new response functions. The new data mentioned in the previous paragraph may allow for the analysis of the recoil polarization on the response function level. Additionally, data is already being analyzed for a double polarization experiment using the polarization of the incident beam as well as the $\Lambda(1116)$ recoil polarization. Data has also been taken and cooked for a triple polarization experiment in which the target was also polarized. The analysis of this data, though, has yet to be undertaken.

In all of these data sets, there exists a large quantity of cleanly identifiable $\Sigma(1193)$ events. The branching ratio of the $\Sigma(1193)$ is 100% to $\Lambda(1116)\gamma$ [22] with the polarization of the Σ related to that of the Λ by P_{Σ^0} = -3P_Λ. Analysis of these events would give further insight into the strange quark degree of freedom. Once again though, the analysis of this data requires a separate set of acceptance functions.

APPENDIX A

TABLES OF EXPERIMENTAL RESULTS

Table A.1. Q^2 dependent cross section data points.

Q^2 (GeV)	$\sigma(Q^2)$ (nb/sr)
1.245 ± 0.045	319 ± 34
1.335 ± 0.045	300 ± 35
1.425 ± 0.045	258 ± 31
1.515 ± 0.045	230 ± 31
1.605 ± 0.045	252 ± 36
1.695 ± 0.045	201 ± 33
1.785 ± 0.045	207 ± 36
1.875 ± 0.045	168 ± 31
1.965 ± 0.045	139 ± 39
2.055 ± 0.045	173 ± 42

Table A.2. $\cos\theta_{cm}^{K^+}$ dependence of recoil polarization for Fig. 6.9

$\cos\theta_{cm}^{K^+}$ Range	P_N	P_T	P_L	Counts
-1.0 - -0.5	-0.163 ± 0.150	0.068 ± 0.123	0.262 ± 0.122	307
-0.5 - 0.0	-0.394 ± 0.124	-0.207 ± 0.098	0.148 ± 0.107	461
0.0 - 0.5	-0.231 ± 0.102	-0.086 ± 0.086	0.218 ± 0.083	637
0.5 - 1.0	-0.243 ± 0.075	0.040 ± 0.057	0.125 ± 0.058	1250

Table A.3. $\cos\theta_{cm}^{K+}$ dependence of recoil polarization for Fig. 6.10

$\cos\theta_{cm}^{K+}$ Range	P_N	P_T	P_L	Counts
-1.0 - -0.5	-0.675 ± 0.163	0.297 ± 0.143	-0.026 ± 0.151	254
-0.5 - 0.0	-0.486 ± 0.083	0.146 ± 0.062	0.018 ± 0.075	1108
0.0 - 0.2	-0.726 ± 0.090	-0.008 ± 0.072	0.114 ± 0.089	871
0.2 - 0.4	-0.434 ± 0.080	-0.098 ± 0.058	0.077 ± 0.074	1174
0.4 - 0.6	-0.358 ± 0.078	-0.106 ± 0.058	-0.038 ± 0.071	1263
0.6 - 0.8	-0.317 ± 0.080	0.062 ± 0.064	0.003 ± 0.074	1140
0.8 - 1.0	-0.245 ± 0.071	0.017 ± 0.052	0.043 ± 0.066	1491

Table A.4. $\cos\theta_{cm}^{K+}$ dependence of recoil polarization for Fig. 6.11

$\cos\theta_{cm}^{K+}$ Range	P_N	P_T	P_L	Counts
-1.0 - -0.5	-0.109 ± 0.205	-0.064 ± 0.146	0.002 ± 0.206	203
-0.5 - 0.0	-0.396 ± 0.100	-0.027 ± 0.076	-0.167 ± 0.085	804
0.0 - 0.2	-0.580 ± 0.104	0.091 ± 0.074	0.136 ± 0.101	780
0.2 - 0.4	-0.471 ± 0.084	-0.099 ± 0.062	-0.040 ± 0.078	1160
0.4 - 0.6	-0.558 ± 0.081	0.050 ± 0.059	-0.121 ± 0.072	1319
0.6 - 0.8	-0.476 ± 0.071	-0.095 ± 0.057	-0.198 ± 0.056	1425
0.8 - 1.0	-0.127 ± 0.084	0.077 ± 0.070	-0.033 ± 0.080	999

Table A.5. Polarizations Versus W

W Range (GeV)	P_N	P_T	P_L	Counts
1.61 - 1.716	-0.252 ± 0.051	-0.026 ± 0.040	0.159 ± 0.041	2655
1.716 - 1.766	-0.344 ± 0.059	0.051 ± 0.044	0.006 ± 0.046	2093
1.766 - 1.816	-0.424 ± 0.058	-0.012 ± 0.044	0.055 ± 0.043	2258
1.816 - 1.866	-0.448 ± 0.053	0.006 ± 0.041	-0.011 ± 0.040	2596
1.866 - 1.916	-0.343 ± 0.056	0.017 ± 0.043	-0.010 ± 0.040	2395
1.916 - 1.966	-0.415 ± 0.064	-0.020 ± 0.049	-0.030 ± 0.048	1848
1.966 - 2.016	-0.412 ± 0.078	-0.029 ± 0.058	-0.115 ± 0.057	1347
2.016 - 2.066	-0.449 ± 0.095	-0.026 ± 0.071	-0.002 ± 0.072	917
2.066 - 2.116	-0.343 ± 0.141	-0.014 ± 0.117	0.246 ± 0.109	392

APPENDIX B

INDIVIDUAL POLARIZATION FITS

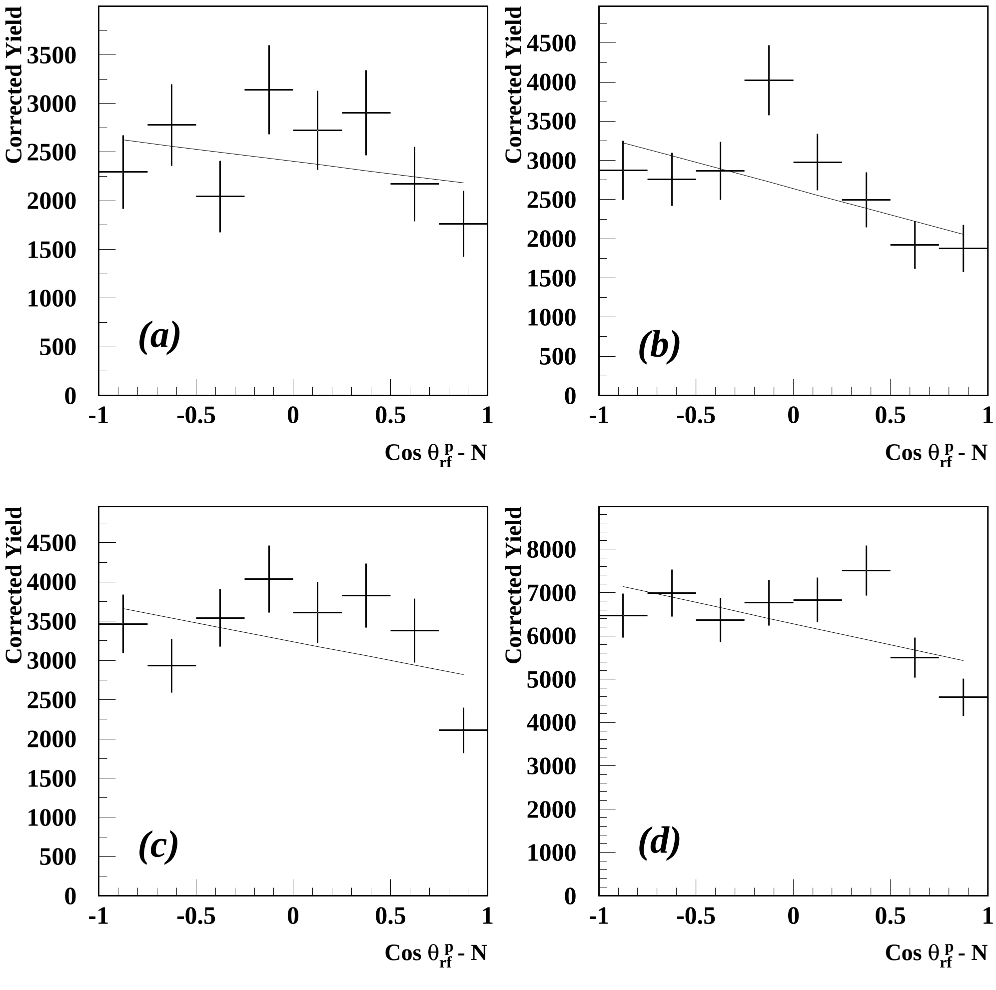

Figure B.1. $\Lambda(1116)$ decay proton angular distributions along the $\Lambda(1116)$ rest frame normal axis for $1.61 < W < 1.716$ GeV and (a) $-1.0 < \cos\theta_{cm}^{K+} < -0.5$, (b) $-0.5 < \cos\theta_{cm}^{K+} < 0.0$, (c) $0.0 < \cos\theta_{cm}^{K+} < 0.5$, and (d) $0.5 < \cos\theta_{cm}^{K+} < 1.0$.

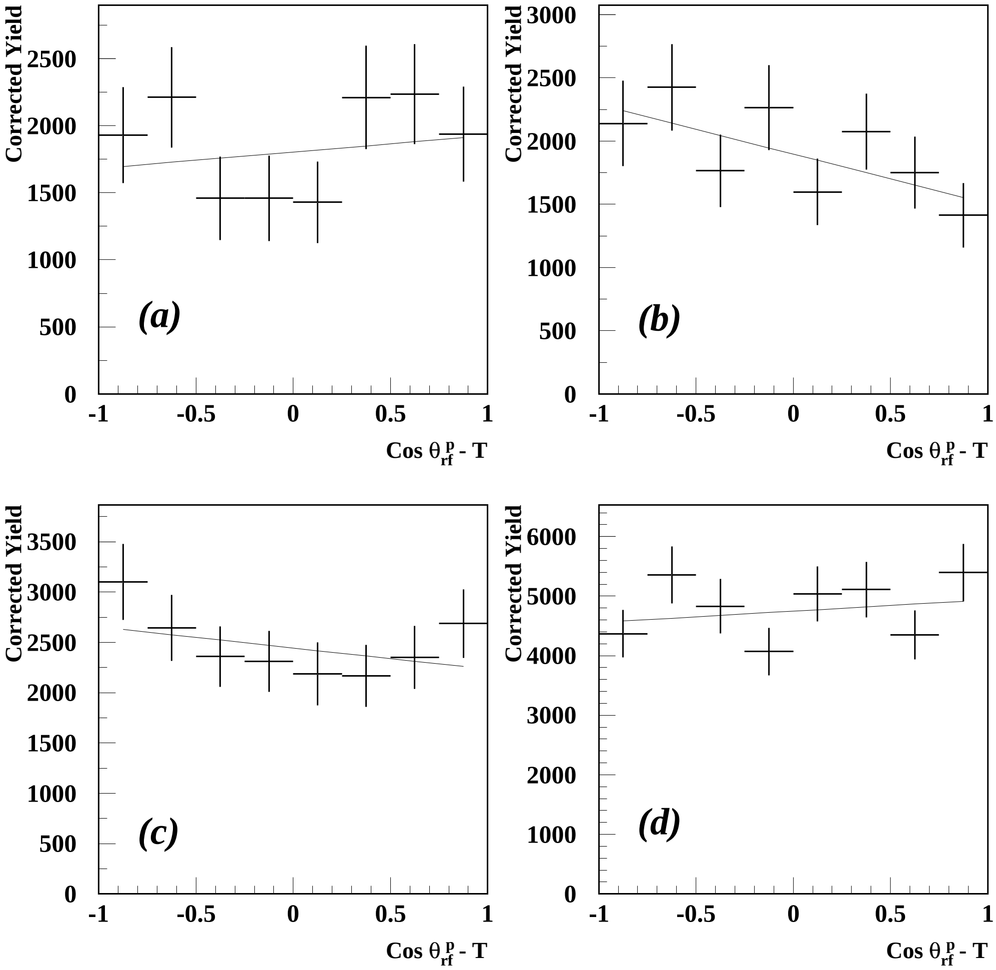

Figure B.2. Λ(1116) decay proton angular distributions along the Λ(1116) rest frame transverse axis for 1.61 < W < 1.716 GeV and (a) -1.0 < $\cos\theta_{cm}^{K+}$ < -0.5, (b) -0.5 < $\cos\theta_{cm}^{K+}$ < 0.0, (c) 0.0 < $\cos\theta_{cm}^{K+}$ < 0.5, and (d) 0.5 < $\cos\theta_{cm}^{K+}$ < 1.0.

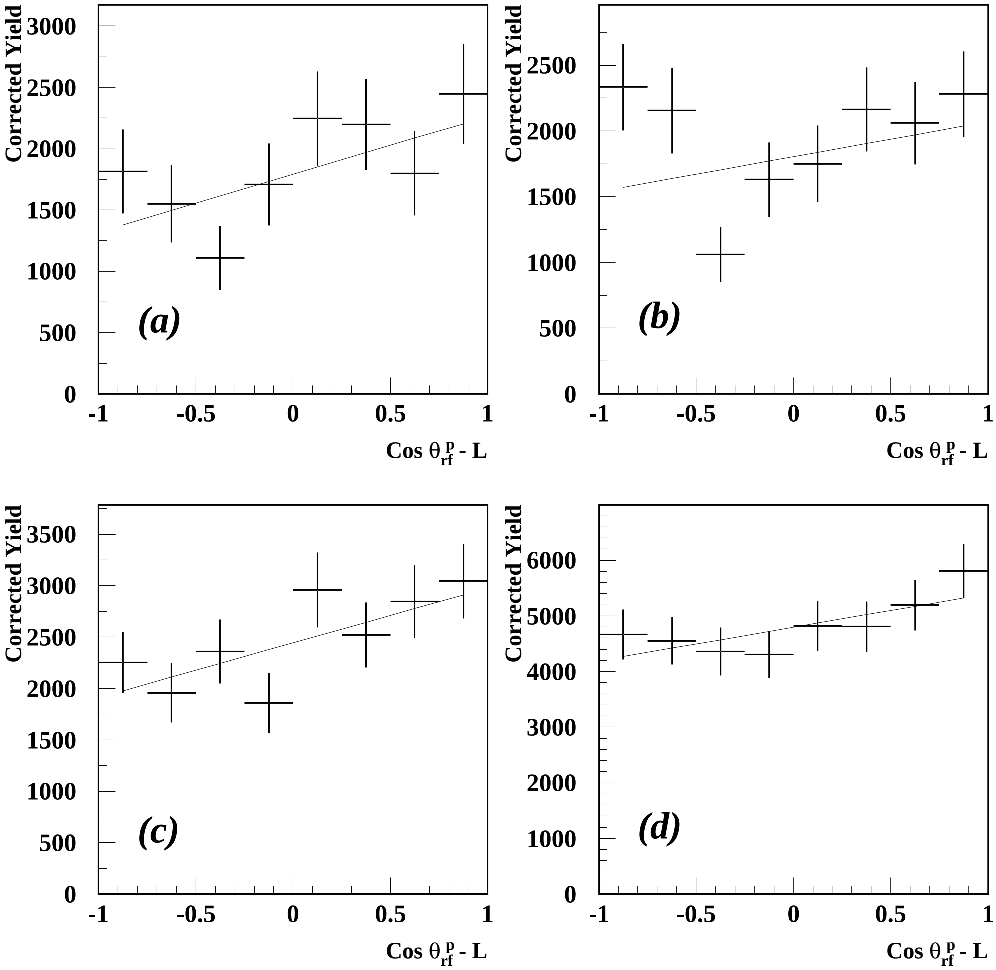

Figure B.3. Λ(1116) decay proton angular distributions along the Λ(1116) rest frame longitudinal axis for 1.61 < W < 1.716 GeV and (a) -1.0 < $\cos\theta_{cm}^{K^+}$ < -0.5, (b) -0.5 < $\cos\theta_{cm}^{K^+}$ < 0.0, (c) 0.0 < $\cos\theta_{cm}^{K^+}$ < 0.5, and (d) 0.5 < $\cos\theta_{cm}^{K^+}$ < 1.0.

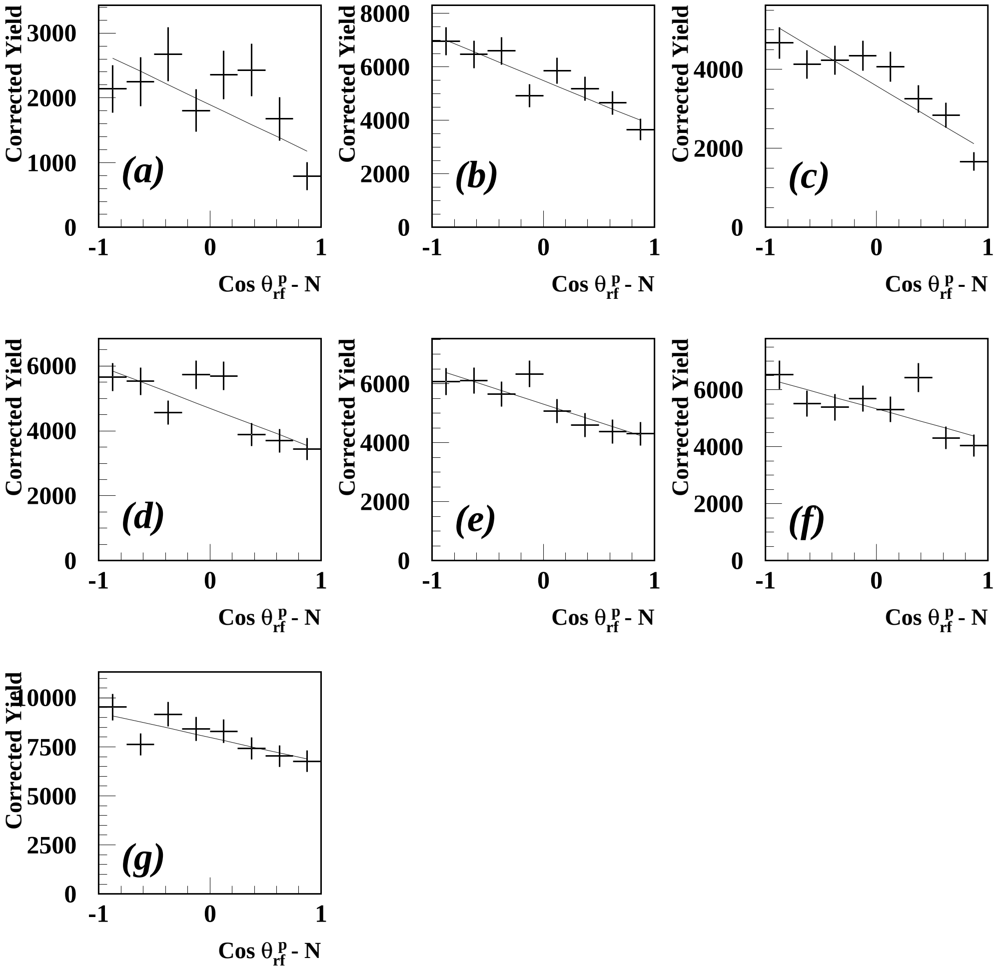

Figure B.4. $\Lambda(1116)$ decay proton angular distributions along the $\Lambda(1116)$ rest frame normal axis for 1.716 < W < 1.873 GeV and (a) -1.0 < $\cos\theta_{cm}^{K^+}$ < -0.5, (b) -0.5 < $\cos\theta_{cm}^{K^+}$ < 0.0, (c) 0.0 < $\cos\theta_{cm}^{K^+}$ < 0.2,(d) 0.2 < $\cos\theta_{cm}^{K^+}$ < 0.4, (e) 0.4 < $\cos\theta_{cm}^{K^+}$ < 0.6, (f) 0.6 < $\cos\theta_{cm}^{K^+}$ < 0.8, and (g) 0.8 < $\cos\theta_{cm}^{K^+}$ < 1.0.

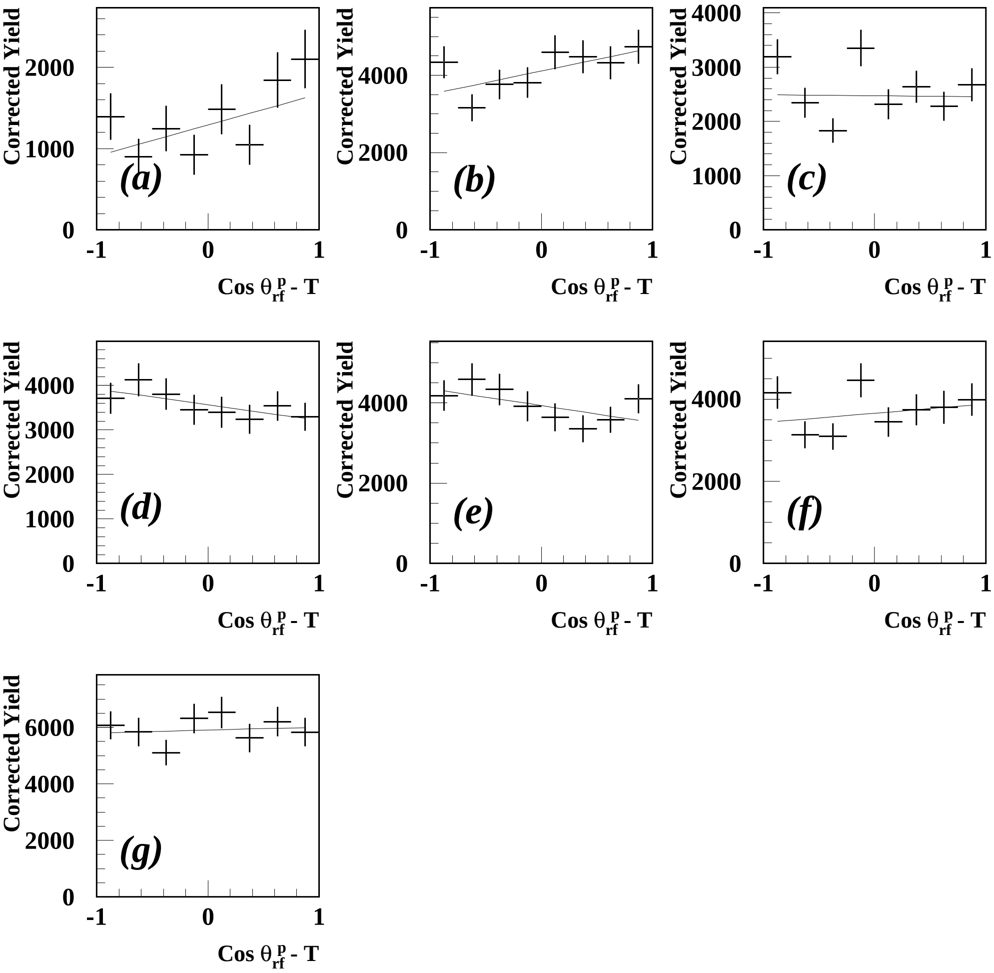

Figure B.5. $\Lambda(1116)$ decay proton angular distributions along the $\Lambda(1116)$ rest frame transverse axis for 1.716 < W < 1.873 GeV and (a) -1.0 < $\cos\theta_{cm}^{K^+}$ < -0.5, (b) -0.5 < $\cos\theta_{cm}^{K^+}$ < 0.0, (c) 0.0 < $\cos\theta_{cm}^{K^+}$ < 0.2,(d) 0.2 < $\cos\theta_{cm}^{K^+}$ < 0.4, (e) 0.4 < $\cos\theta_{cm}^{K^+}$ < 0.6, (f) 0.6 < $\cos\theta_{cm}^{K^+}$ < 0.8, and (g) 0.8 < $\cos\theta_{cm}^{K^+}$ < 1.0.

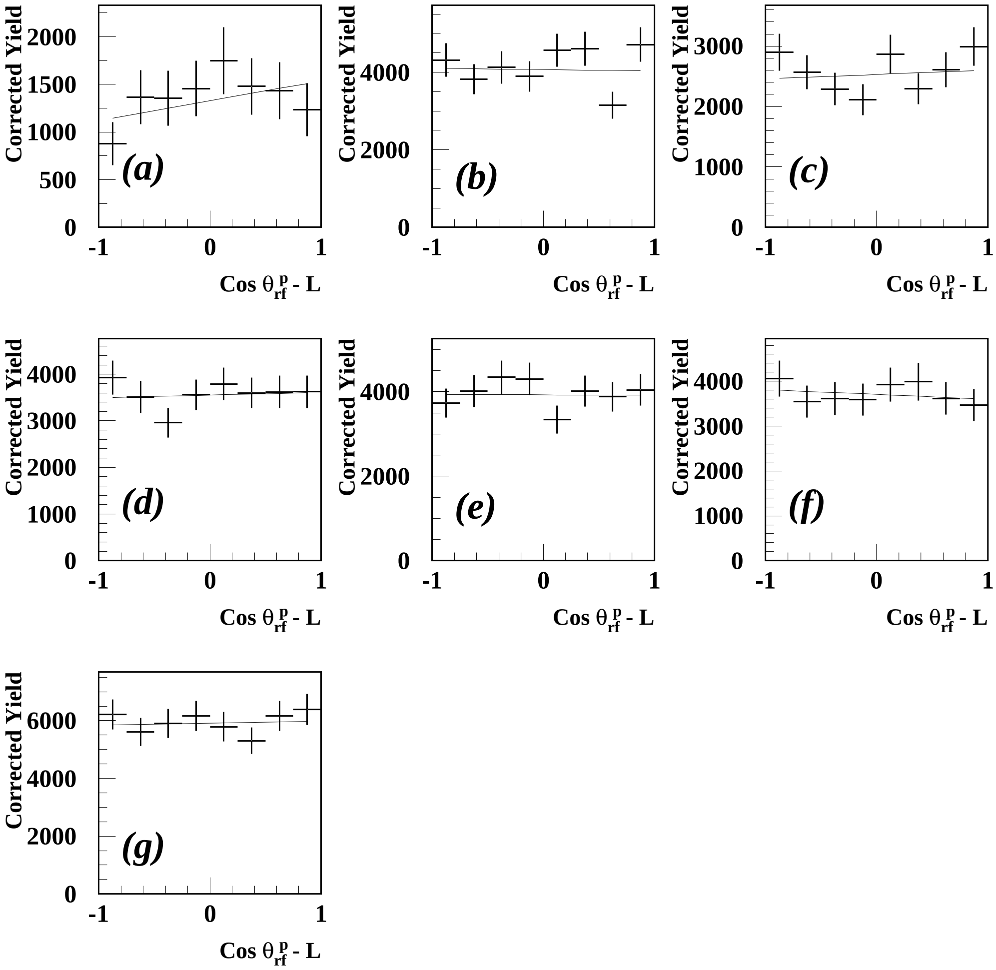

Figure B.6. $\Lambda(1116)$ decay proton angular distributions along the $\Lambda(1116)$ rest frame longitudinal axis for 1.716 < W < 1.873 GeV and (a) -1.0 < $\cos\theta_{cm}^{K^+}$ < -0.5, (b) -0.5 < $\cos\theta_{cm}^{K^+}$ < 0.0, (c) 0.0 < $\cos\theta_{cm}^{K^+}$ < 0.2,(d) 0.2 < $\cos\theta_{cm}^{K^+}$ < 0.4, (e) 0.4 < $\cos\theta_{cm}^{K^+}$ < 0.6, (f) 0.6 < $\cos\theta_{cm}^{K^+}$ < 0.8, and (g) 0.8 < $\cos\theta_{cm}^{K^+}$ < 1.0.

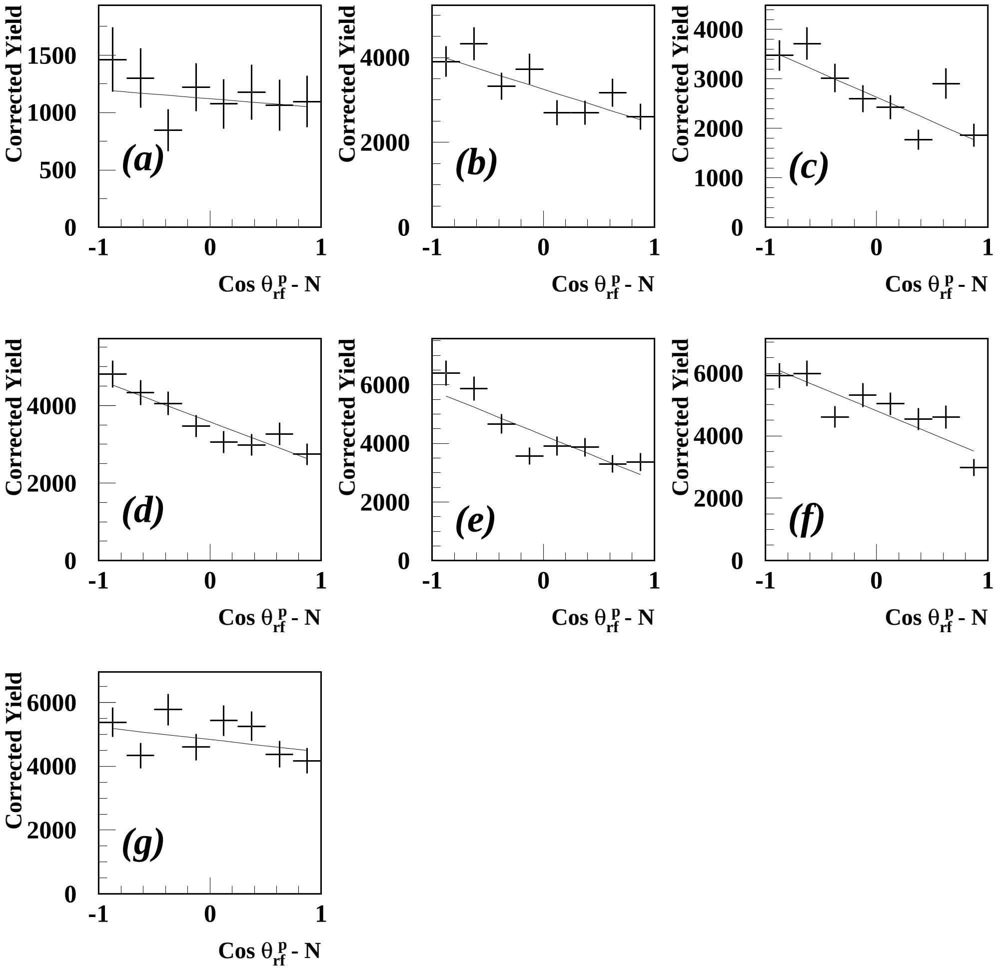

Figure B.7. $\Lambda(1116)$ decay proton angular distributions along the $\Lambda(1116)$ rest frame normal axis for $1.873 <$ W < 2.152 GeV and (a) $-1.0 < \cos\theta_{cm}^{K^+} < -0.5$, (b) $-0.5 < \cos\theta_{cm}^{K^+} < 0.0$, (c) $0.0 < \cos\theta_{cm}^{K^+} < 0.2$,(d) $0.2 < \cos\theta_{cm}^{K^+} < 0.4$, (e) $0.4 < \cos\theta_{cm}^{K^+} < 0.6$, (f) $0.6 < \cos\theta_{cm}^{K^+} < 0.8$, and (g) $0.8 < \cos\theta_{cm}^{K^+} < 1.0$.

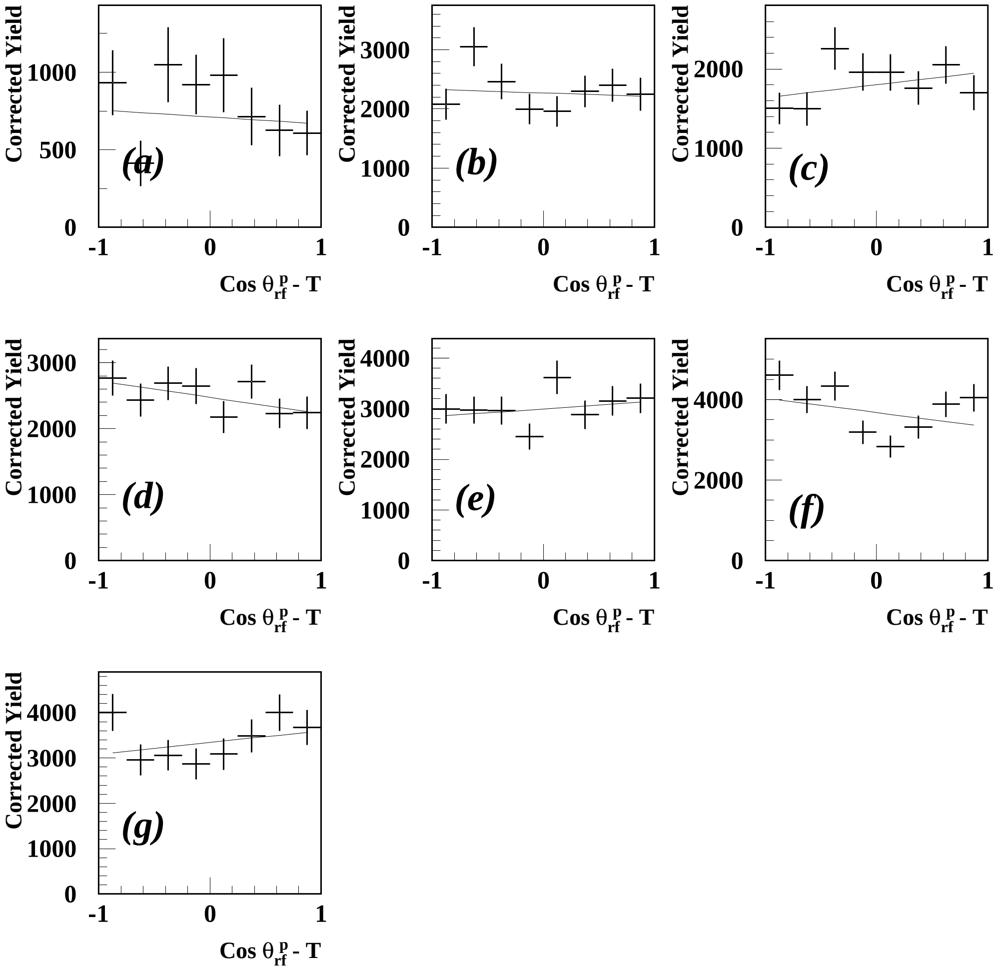

Figure B.8. Λ(1116) decay proton angular distributions along the Λ(1116) rest frame transverse axis for 1.873 < W < 2.152 GeV and (a) -1.0 < $\cos\theta_{cm}^{K^+}$ < -0.5, (b) -0.5 < $\cos\theta_{cm}^{K^+}$ < 0.0, (c) 0.0 < $\cos\theta_{cm}^{K^+}$ < 0.2,(d) 0.2 < $\cos\theta_{cm}^{K^+}$ < 0.4, (e) 0.4 < $\cos\theta_{cm}^{K^+}$ < 0.6, (f) 0.6 < $\cos\theta_{cm}^{K^+}$ < 0.8, and (g) 0.8 < $\cos\theta_{cm}^{K^+}$ < 1.0.

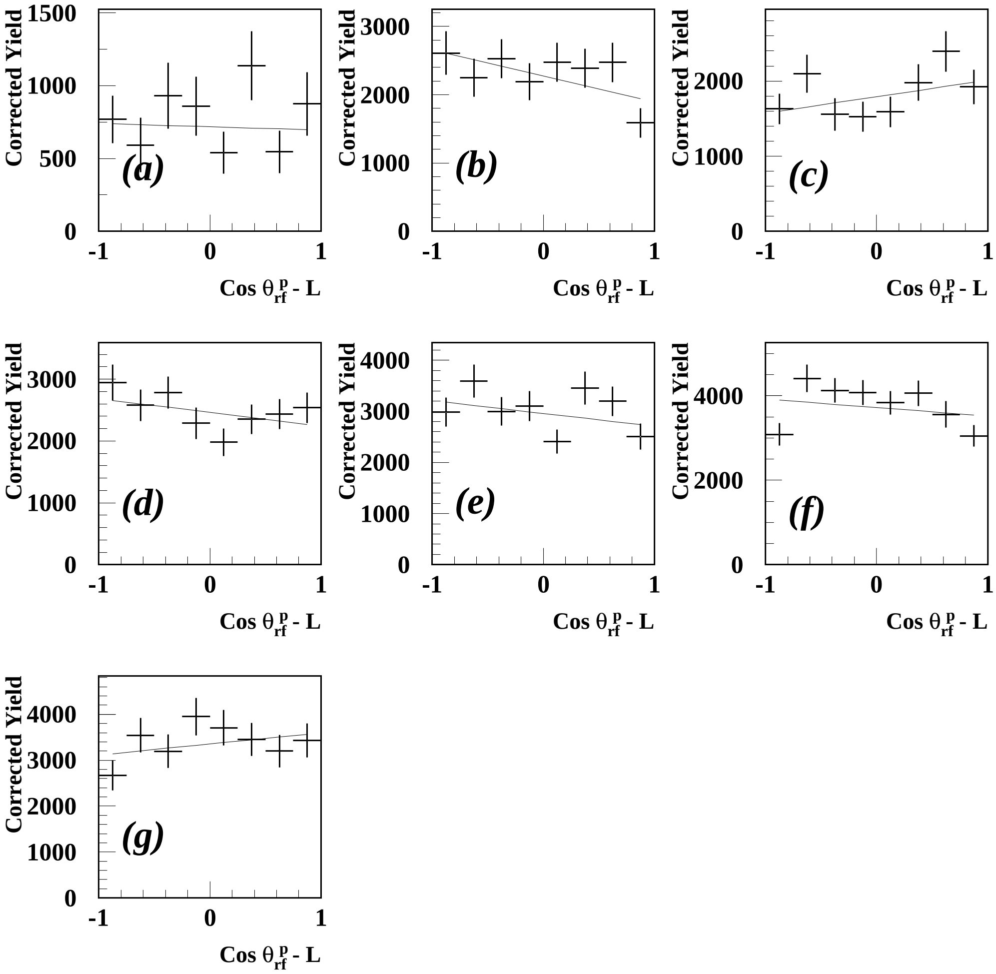

Figure B.9. $\Lambda(1116)$ decay proton angular distributions along the $\Lambda(1116)$ rest frame longitudinal axis for 1.873 < W < 2.152 GeV and (a) -1.0 < $\cos\theta_{cm}^{K^+}$ < -0.5, (b) -0.5 < $\cos\theta_{cm}^{K^+}$ < 0.0, (c) 0.0 < $\cos\theta_{cm}^{K^+}$ < 0.2,(d) 0.2 < $\cos\theta_{cm}^{K^+}$ < 0.4, (e) 0.4 < $\cos\theta_{cm}^{K^+}$ < 0.6, (f) 0.6 < $\cos\theta_{cm}^{K^+}$ < 0.8, and (g) 0.8 < $\cos\theta_{cm}^{K^+}$ < 1.0.

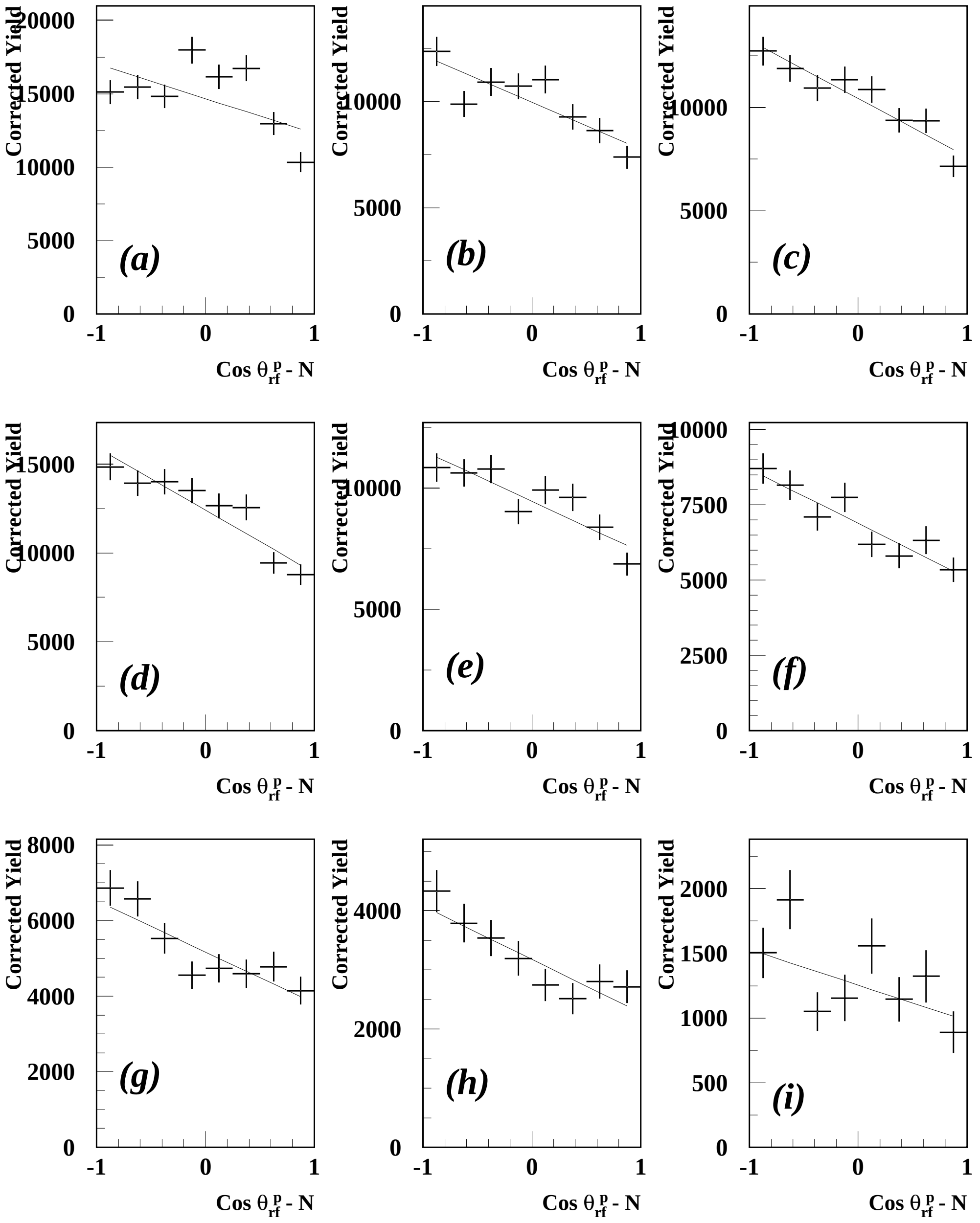

Figure B.10. $\Lambda(1116)$ decay proton angular distributions along the $\Lambda(1116)$ rest frame normal axis for (a) $1.61 < \text{W} < 1.716$ GeV, (b) $1.716 < \text{W} < 1.766$ GeV, (c) $1.766 < \text{W} < 1.816$ GeV, (d) $1.816 < \text{W} < 1.866$ GeV, (e) $1.866 < \text{W} < 1.916$ GeV, (f) $1.916 < \text{W} < 1.966$ GeV, (g) $1.966 < \text{W} < 2.016$ GeV, (h) $2.016 < \text{W} < 2.066$ GeV, and (i) $2.066 < \text{W} < 2.116$ GeV.

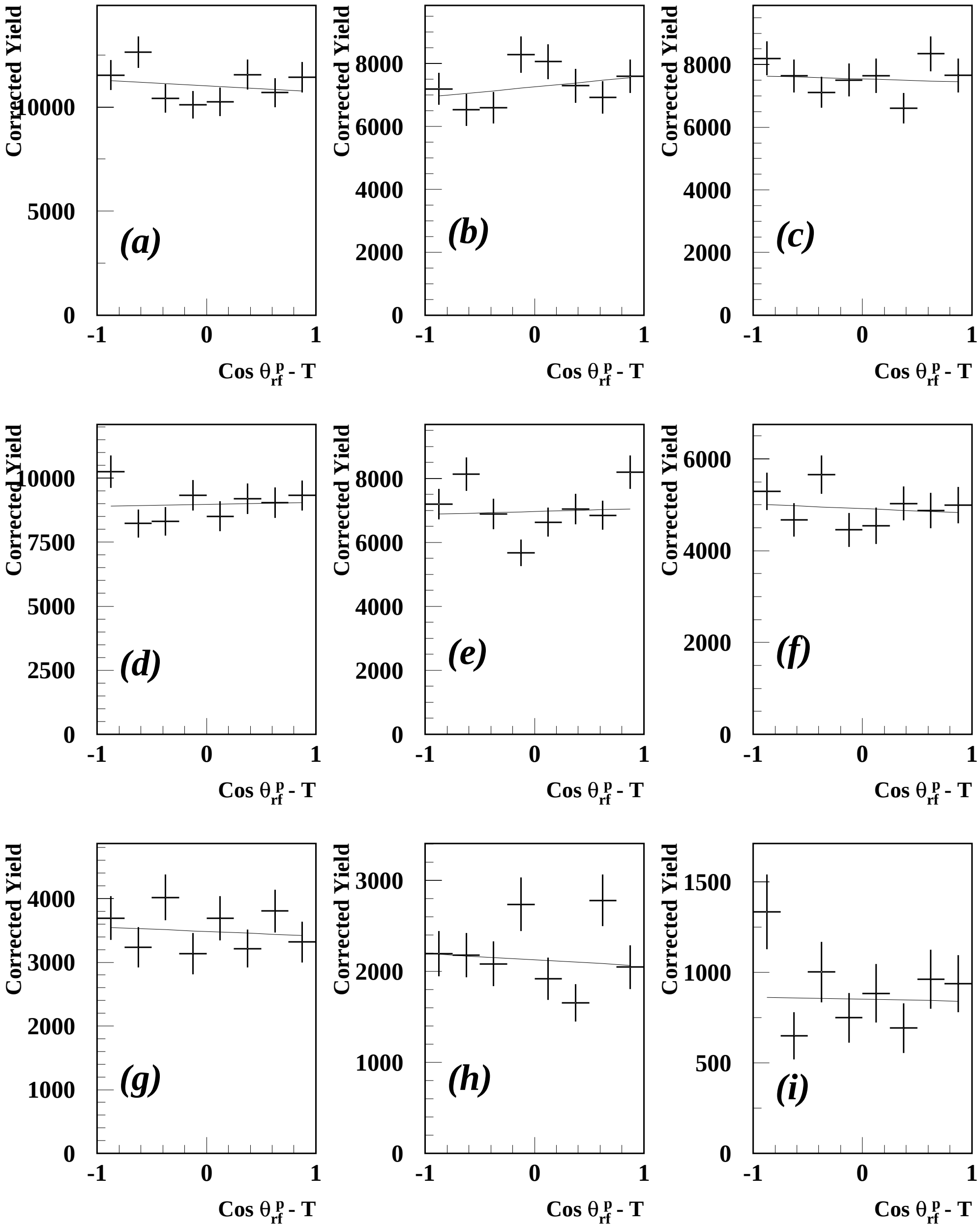

Figure B.11. Λ(1116) decay proton angular distributions along the Λ(1116) rest frame transverse axis for (a) 1.61 < W < 1.716 GeV, (b) 1.716 < W < 1.766 GeV, (c) 1.766 < W < 1.816 GeV, (d) 1.816 < W < 1.866 GeV, (e) 1.866 < W < 1.916 GeV, (f) 1.916 < W < 1.966 GeV, (g) 1.966 < W < 2.016 GeV, (h) 2.016 < W < 2.066 GeV, and (i) 2.066 < W < 2.116 GeV.

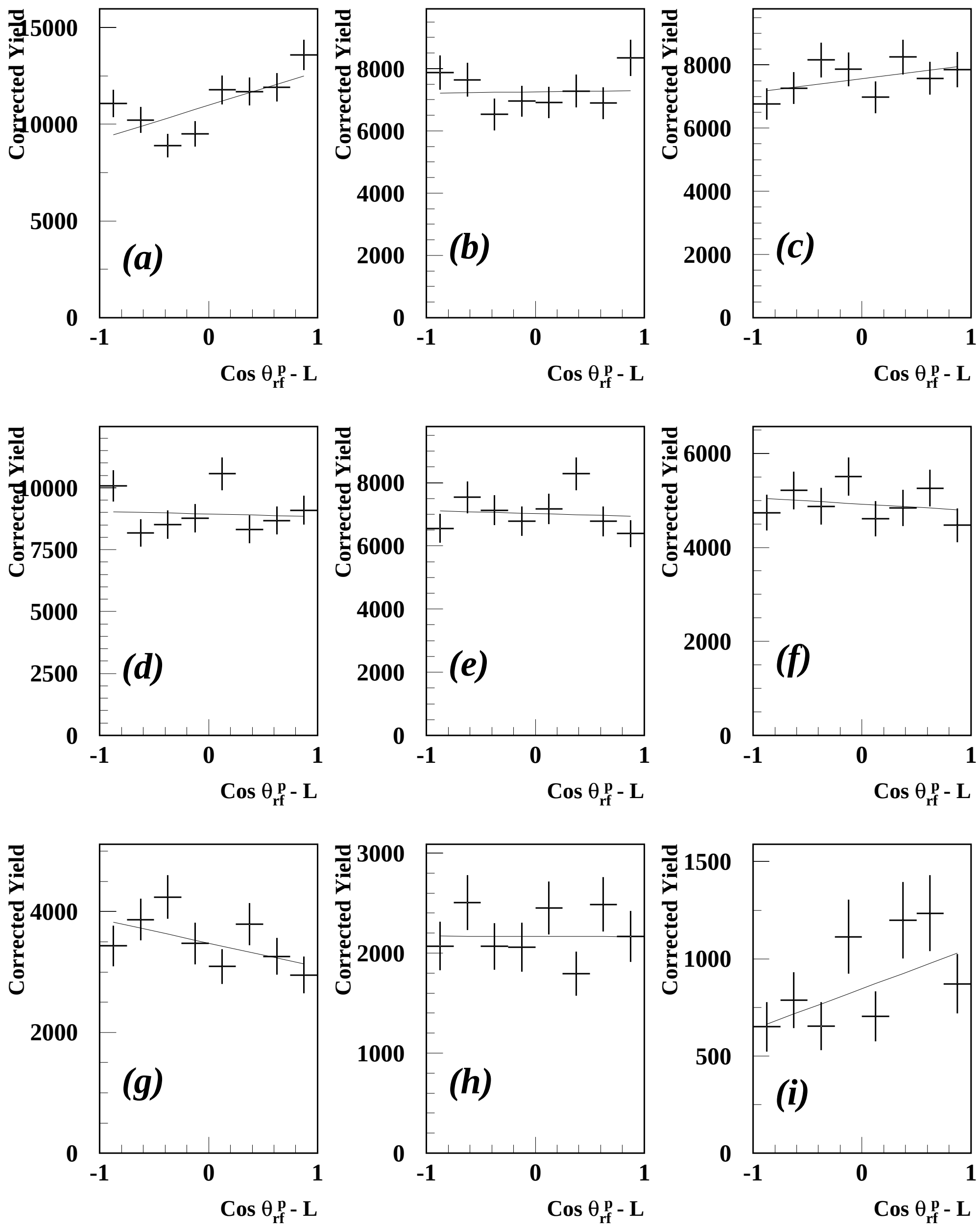

Figure B.12. $\Lambda(1116)$ decay proton angular distributions along the $\Lambda(1116)$ rest frame longitudinal axis for (a) 1.61 < W < 1.716 GeV, (b) 1.716 < W < 1.766 GeV, (c) 1.766 < W < 1.816 GeV, (d) 1.816 < W < 1.866 GeV, (e) 1.866 < W < 1.916 GeV, (f) 1.916 < W < 1.966 GeV, (g) 1.966 < W < 2.016 GeV, (h) 2.016 < W < 2.066 GeV, and (i) 2.066 < W < 2.116 GeV.

REFERENCES

[1] G.D. Rochesterand C.C. Butler, Nature **160** (1947) 855.

[2] R. N. Cahn and G. Goldhaber, *The Experimental Foundations of Particle Physics*, (Cambridge University Press 1989) 52-84.

[3] S. P. Barrow, *et al.* Phys. Rev. C **64** (2001) 044601-1 - 044601-10.

[4] J.C. David, C.Fayard, G. H. Lamot, and B. Saghai, Phys. Rev. C **53** (1996) 2613 - 2637.

[5] R. A. Williams, C. -R. Ji, and S.R. Cotanch, Phys. Rev. C **46** (1992) 1617 - 1635.

[6] D.S. Carman, K. Joo, L. Kramer, and B. Raue, "Polarization observables in the $^{1}\mathrm{H}(\overrightarrow{e}, \mathrm{e}'\mathrm{K}^{+})\overrightarrow{\Lambda^{0}}$ reaction.", JLAB Preprint PR99-006.

[7] D. H. Perkins, *Introduction to High Energy Physics*, (Addison-Wesley 1987) 220 - 222.

[8] C. -R. Ji and S. R. Cotanch, Phys. Rev. C **38** (1988) 2691.

[9] R. Dolen, D. Horn, C. Schmid, Phys. Rev. Lett. **19** (1967) 402; Phys. Rev. **166** (1968) 1768.

[10] R. A. Adelseck and B. Saghai, Phys. Rev. C **42** (1990) 108.

[11] M. Guidal, J.-M. Laget, and M. Vanderhaeghen, Nuc. Phys. A **627** (1997) 645 - 678.

[12] R. M. Mohring, Ph. D. thesis, University of Maryland, (1999) unpublished.

[13] M. Guidal, J.-M. Laget, and M. Vanderhaegen, Phys. Rev. C **61** (2000)

[14] T. Azemoon *et al.*, Nucl. Phys. B 95 (1975) 77 - 97; C. J. Bebek *et al.*, Phys. Rev. D **15** (1977) 594 - 601; C. J. Bebek *et al.*, *ibid.* **15** (1977) 3082 - 1089; P. Brauel *et al.*, Z. Physik C **3** (1979) 101 - 123; G. Niculescu *et al.*, Phys. Rev. Let. **81** (1998) 1805 - 1808.

[15] H. Thom *et al.*, Phys. Rev. Let. **11** (1963) 433-435.

[16] B. Borgia *et al.*, Nuovo Cimento **32** (1964) 218-223.

[17] M. Grilli, L. Mezzetti, M. Nigro, E. Schiavuta, Nuova Cimento **38** (1965) 1467-1488.

[18] D. E. Groom, J. H. Marshall, Phys. Rev **159** (1967) 1213-1219.

[19] T. Fujii *et al.*, Phys. Rev. D 2 (1970) 439-448.

[20] M. Q. Tran *et al.*, Phys. Lett. B **445** (1998) 20-26.

[21] L. Teodorescu *et al.*, Nucl. Phys. A 658 (1999) 362-371.

[22] C. Caso *et al.* (Particle Data Group), Review of Particle Physics, Eurpoean Physics Journal **C3** (1998) 1.

[23] G. Knöchlein, D. Dreschel, and L. Tiator, Z.Physik A **32** (1995) 327.

[24] A. Dooley Ph. D. thesis, Florida State University (2001) unpublished.

[25] W. E. Kleppinger and J.D. Walecka, Annals of Physics **146** (1983) 349-394.

[26] South Eastern Universities Research Association, *Conceptual Design Report: CEBAF Basic Experimental Equipment*, (1990) A - 1.

[27] Volker D. Burkert, "CEBAF and the Baryon Physics Program", Invited talk to Baryons '95 Conference in Santa Fe CEBAF-PR-96-001.

[28] M. D. Mestayer *et al.*, (CLAS Collaboration) Nucl. Instr. and Meth. A449 (2000) 81.

[29] E. S. Smith *et al.*, (CLAS Collaboration) Nucl. Instr. and Meth. A432 (1999) 265.

[30] G. Adams *et al.*, (CLAS Collaboration) "The CLAS Čerenkov Detector", submitted to Nucl. Instr. and Meth.

[31] M. Amarian *et al.*, (CLAS Collaboration) "The CLAS Forward Electromagnetic Calorimeter", submitted to Nucl. Instr. and Meth.

[32] Volker D. Burkert, private communication.

[33] Volker Blobel *et al.*, (CLAS Collaboration) "The BOS System fo CLAS detector", 1995.

[34] S. P. Barrow *et al.*, (CLAS Collaboration) "Data Acquisition System for Hall B of TJLAB", in progress.

[35] J.J. Manak, E.S. Smith, S. McAleer, S. Barrow, "e1, g1, and g6 Data Processing Procedures", JLAB Hall B CLAS-NOTE 1999-016,(unpublished).

[36] R Thompson, Ph. D. thesis, University of Pittsburgh, 1999, (unpublished).

[37] K. S. Egyian, "Determination of Electron Energy Cut Due to the CLAS EC Threshold", JLAB Hall B CLAS-NOTE 1999-011, (unpublished).

[38] E. Anciant, private communication, 1999.

[39] E. S. Smith *et al.*, "Calibration of the CLAS TOF System", JLAB Hall B CLAS-NOTE 1999-011, (unpublished).

[40] B. Mecking, *First results from the CEBAF CLAS spectrometer*, in Proc. Baryons '98 Conference, Bonn, 1998, Am. Phys. Soc.

[41] L. Dennis, private communication, 2000.

[42] R. Williams, C.-R. Ji, and S. Cotanch, Phys. Rev. Lett. **63** (1991) 1352.

[43] R. Feuerbac, private communication, 2000.

[44] T. Mart, private communication, 2000.

[45] K. Joo, private communication, 2001.

[46] S. Barrow, "$\Lambda(1520)$ electroproduction results", CLAS ANALYSIS NOTE 2000-002, (unpublished).

[47] S. P. Barrow, "Reconstruction inefficienies for pairs of positively charged hadrons with a small relative angle", CLAS ANALYSIS NOTE 1999-003, (unpublished).

[48] Konstantin Loukachine, Ph. D. Thesis, Virginia Polytechnic Institute and State University, 2000, unpublished.

[49] S. P. Barrow, "Backgrounds and systematic errors in teh study of $\Lambda(1520)$ electroproduction", CLAS ANALYSIS NOTE 2001-004, (unpublished).

[50] R. Ent, B. W. Fillippone, N.C.R. Makins, R.G. Milner, T.G. O'Neill, D.A. Wasson, Phys. Rev. C **64** (2001) 054610.

[51] A. Vlassov, private communication, 2000.

[52] L. C. Smith, private communication, 2000.

[53] S.P. Barrow, private communication, 2000.

[54] L. KRAMER, R. NASSERIPOUR, AND B. RAUE, "Analysis of e1c beam charge asymmetries", CLAS-NOTE 2001-12, (unpblished).

[55] R. THOMPSON, S. DYTMAN, K.Y. KIM, J. MEULLER, "A study of Eta Electroproduction using CLAS E1A data", CLAS ANALYSIS NOTE 2000-003, (unpublished).

[56] C. J. BEBEK *et al.*, Phys. Rev. D **15** (1977) 594.

[57] C. BROWN *et al.*, Phys. Rev. Lett. **28** (1972) 1086.

[58] T. AZEMOON *et al.*, Nuc. Phys. **95** (1975) 77.

[59] C. J. BEBEK *et al.*, Phys. Rev. Lett. **32** (1974) 21.

[60] G. NICULESCU *et al.*, Phys. Rev. Lett. **81** (1998) 1805.

[61] P.R.BEVINGTON, *Data Reduction and Error Analysis for the Physical Sciences*, (McGraw-Hill - 1969) 195 - 198.

[62] S. CAPSTICK AND W. ROBERTS, Phys. Rev. D **58** (1998) 074011.

[63] C. BENNHOLD, H. HABERZETTL, T. MART, nucl-th/9909022, conference proceedings ICTP International Conference on Perspectives in Hadronic Physics (1999).

BIOGRAPHICAL SKETCH

Simeon B. McAleer

Simeon B. McAleer was born in Rego Park, New York on 24 September 1973, and graduated from Regis High School in New York City in May 1991. He received the Ignation scholarship from the University of Scranton in Pennsylvania where he received a Bachelor of Science in physics and mathematics with a minor in Russian in May 1995. That fall he entered the doctoral program of the physics department at Florida State University. He received a Master of Science degree in August 1997 from Florida State University. During his time at Florida State University, he received two University Fellowhips as well as a fellowship from the Southeastern Universities Research Association. This dissertation was defended on December 13, 2001 at Florida State University.